Ph.D thesis

Design of a biocompatible probe for theranostic and multimodal imaging applications

Coordinator:
Prof. Giuseppe Mensitieri
Supervisors:
Prof. Paolo Antonio Netti
Eng. Enza Torino Ph.D.

Candidate
Donatella Vecchione

Contents

Thesis Abstract

Multimodal imaging probes can provide diagnostic information combining different imaging modalities. Nanoparticles (NPs) can contain two or more imaging tracers that allow several diagnostic techniques to be used simultaneously. In this thesis, a complex coacervation process to produce core-shell completely biocompatible polymeric nanoparticles (HyCoS) for multimodal imaging applications is described. Innovations on the traditional coacervation process are found in the control of the reaction temperature, allowing a speeding up of the reaction itself, and the production of a double-crosslinked system to improve the stability of the nanostructures in the presence of a clinical relevant contrast agent for MRI (Gd-DTPA). Through the control of the crosslinking behavior, an increase up to 6 times of the relaxometric properties of the Gd-DTPAis achieved. Furthermore, HyCoS can be loaded with a high amount of dye such as ATTO 633 or conjugated with a model dye such as FITC for *in vivo* optical imaging. The results show stable core-shell polymeric nanoparticles that can be used both for MRI and for optical applications allowing detection free from harmful radiation. Additionally, preliminary results about the possibility to trigger the release of a drug through a pH effect are reported. Furthermore, NPs combined with peptides, allow an efficient in vivo targeting useful to improve drug delivery and clinical outcome. We report the in vivo targeting of aggressive A20 murine B-cell

lymphoma by idiotype-specific peptide pA20-36 using fluorescence molecular tomographic (FMT) imaging in xenograft mouse models of lymphoma A20, through VivoTag probe, an amine-reactive near-infrared fluorochrome. In the end, core-shell polymeric nanovector with improved relaxometric properties for simultaneous PET/MRI acquisitions. and ^{18}F-FDG is used as tracer for PET. A protocol for sorption of ^{18}F-FDG into the nanoparticles is studied and designed to be integrated downstream the production of the tracer.

Introduction

Therapy and Multimodal Imaging

Nowadays, the possibility to combine a drug for a specific disease with one or more tracers for their use in simultaneous diagnostic techniques is the new frontier of the modern medicine[1]. Pharmaceutical companies have striven to produce diagnostic compounds with higher efficacies and improved safety profiles. Traditionally, drugs have low molecular active compounds which are often the result of engineering of a natural product[2]. They can be classified according to the active principle, the mechanism of action, their use and the type of administration[3] [4] [5] During a therapy it is crucial to monitor the therapeutic effect through the use of diagnostic technologies[6] furthermore, the possibility to integrate different imaging modalities contributes to an earlier and accurate diagnosis. The term "multimodal imaging" is referred to the integration of diagnostic technologies based on different physical principles for the acquisition of complementary information[7, 8]. Currently, the modalities available for imaging include optical imaging, magnetic resonance imaging (MRI), nuclear imaging, computer tomography (CT), and ultrasound (US)[9]. These technologies can acquire simultaneously or consequently the different information[10]. The asynchronous post-processing acquisition presents various problems, all based on the different position that the patients acquire during the different exams in the instruments. For this reason, the worldwide

companies are working to integrate different diagnostic techniques based on different physical principles in a single diagnostic instrument[11]. This allows to overcome the various limitations as the partial volume effects. In the last decade, instruments such as PET/MRI and Optic/PET machines have answered to this request allowing the simultaneous acquisition of structural, functional and metabolic information.

Diagnostic Techniques

Among the different diagnostic techniques, the most commonly used for the detection of tumor and neurodegenerative diseases is the MRI.

Magnetic Resonance Imaging (MRI) and Contrast Agents (CAs)

Magnetic Resonance Imaging [12] is one of the most important non invasive imaging modalities in clinical diagnostics and research, its characteristic is to use not ionizing rays. This technique has the ability to image tissues with high resolutions in three dimensions. More important however is the unique ability of MRI to obtain information both on anatomy and on a wide range of physiological parameters within a single examination, unsurpassed by other techniques[13][14]. MRI allows obtaining images by measuring the RF signals originating from the magnetic moments of lipid and mainly water protons in living tissues. The use of water as a probe molecule has many advantages. First of all, the proton has the highest

sensitivity among biologically relevant nuclei, and water is present in high concentrations in all tissues. The magnetic properties of water are sensitive to the local microstructure and composition of biological tissues. However, sometimes insufficient contrast is observed and so the use of contrast agents (CAs) is of great assistance in many applications of MRI or of other diagnostic techniques[15]. MRI contrast agents are used to improve the visibility of internal body structures in magnetic resonance imaging (MRI), they can be divided in paramagnetic, superparamagnetic, and ferromagnetic compounds[16]. A number of such substances have been developed and research continues in order to find more selective contrast media that will allow a better delineation of diseases, thus helping radiologists to make a more precise diagnosis [17]. MRI technique exploits the minute imbalance in the number of spin-up and spin-down protons when they placed in a strong magnetic field, which produces a tiny net magnetization in thermal equilibrium. The equilibrium can be disturbed by radiating the protons with an external resonant radio-frequency (RF) electromagnetic field leaving the system in an excited state. When the RF field is turned off the system relaxes back to thermal equilibrium with a process that is known as relaxation. There are two different relaxation processes spin-lattice or longitudinal relaxation (T_1) while the second is spin-spin or transverse relaxation (T_2). The transverse relaxation process may be accelerated by microscopic and macroscopic magnetic field

inhomogeneities in which case the latter relaxation process is referred to as T_2^*. Most of the contrast agents generate contrast by changing the T_1 and T_2. Relaxivity (r_1 and r_2) is a parameter that is inversely proportional to the relaxation times and it characterizes the properties of a MRI contrast agent. Relaxivities r_1 and r_2 are dependent on the magnetic field strength. Generally, r_1 decreases at higher field strength while r_2 stays constant or increases[15, 18]. The ratio between r_2 and r_1 determines whether a contrast agent is suitable for contrast enhanced T_1-weighted imaging or whether it can be used for contrast enhanced T_2- and T_2^*-weighted imaging. However, the MRI contrast agents can be classified into two groups: CAs which increase the transverse relaxation rate ($1/T_2$) and those that increase the longitudinal relaxation rate ($1/T_1$).

T_1 contrast agents are prevalently paramagnetic contrast agents, they are used to enhance MR images and to detect hypervascularity and diseases. They have their strongest effect in T_1 weighted imaging because they predominantly alter the T_1 relaxation time in the tissues in which they have accumulated. MRI imaging is based on the signal derived from the behavior of water protons, their relaxation is affected by the surrounding tissues and, in presence of a paramagnetic contrast agent this parameter enhances. Paramagnetic Gadolinium (Gd) based on contrast agents are examples of T_1 agents[13]. Gadolinium (Gd) is a paramagnetic ion with seven unpaired electrons. It disturbs the relaxation of nearby water protons, causing

decreases of both T_1 and T_2 relaxation times being stronger with the concentrations used in clinical practice.

Free iones of Gadolinium (Gd) are toxic in vivo (lethal dose for 50 % of the population (LD50) for $GdCl_3$ in mice 100 – 200 mg/kg) [19] but its binding to a chelate complex makes it chemically inert. After chelation, the rate of renal excretion of the Gd complex is increased approximately 550-fold compared with pre-chelation values[12]. For all types of contrast agents exists a precise dose to administrate in relation to the weight of the patient and other details as the age or the presence of a specific desease[20].

The Gd chelates are approved for clinical use in the international market. For clinical use, the recommended dose is 0,1 mmol/Kg. The values of T_1 and T_2 can be measured or by region of interest (ROI) through MRI image or by relaxometer using two different types of applications that are called saturation recovery (SR) or inversion recovery (IR)[21]. Commonly non specific extracellular gadolinium chelates include[21]: Magnevist, Dotarem, ProHance, Gadovist, MultiHance, Omniscan, OptiMARK.

There are many advantages using contrast agents as include better lesion enhancement, delineation and detectability of Central Nervous System (CNS) but there are also some limitations and drawbacks. Fist limitation is toxicity. Free ion Gd is acutely toxic owing to its tendency to precipitate and be deposited in liver, lymph nodes, and bones. It may also obstruct calcium-ion passage through muscle

cells, and block the flow of calcium in bone epiphyses and nerve tissue cells, causing the arrest of neuromuscular transmission. A primary factor contributing to the toxicity of Gd complexes is its capability to replace some endogenous metals, especially Zinc, this phenomenon is called trans-metallation. Another important parameter which governs toxicity is the stability of the complex. The tolerance of Gd chelates is excellent at both standard and higher doses, with no clinically relevant difference among these agents, same adverse events are observed with an incidence of less than 2%, with most being mild and transient. The frequency of single adverse events is approximately 1% or less of all patients. The most frequently reported adverse events are nausea, headache and vomiting; they are not severe and do not require specific treatment[20]. Anaphylactic reactions, involving respiratory, cardiovascular, cutaneous, gastrointestinal and/or genitourinary manifestations have been reported with a prevalence of between 1/100.000 to 1/500.000[20]. Gd chelates have not been approved for use in pregnant women, because of the lack of information on potentially harmful effects on the embryo and fetus and on the clearance rate of Gd chelates from the amniotic fluid by the mother[22]. There are other types of risks as the renal insufficiency, one of the major risk factor using Gadolinium is Nephrogenic System Fibrosis (NFS) [23] [24]. NSF was observed for the first time in 1997 and it presents with rapidly progressive skin thickening, tethering and hyperpigmentation,

principally involving the extremities. It is a systemic disease that is associated with exposure to gadolinium-based MRI contrast in patients with compromised renal function. For those afflicted, this disorder has caused indescribable suffering, permanent disability and increased mortality[25]. Furthermore, recent concerns about the deposition of clinical relevant Gd-based Contrast Agents, linear and macrocyclic one are reported by Robert McDonald on neuroradiology[26] and other publications[27] [28]. Moreover, the recent opinion of the FDA suggests the limiting the Gadolinium-based CAs use to clinical circumstances in which the additional information provided by the contrast is necessary. On the same course of action, a general review also has summarized the literature on gadolinium-based contrast agents [29] and so the importance to protect the Gd, both linear and macrocyclic, and overcome the low specificity of the CAs. Furthermore, for linear and macrocyclic both, relaxivity is well below the required theoretical limits and the boost of the signal is still a challenge. Furthermore, in many cases, it is not the tissues under investigation being imaged, but the tracking agent. This can result in false positive results.

Positron Emission Tomography (PET) and Radiopharmaceuticals

The Positron Emission Tomography (PET) [30] is one of the nuclear medicine techniques, which allows the in vivo measure of the local concentration of radiopharmaceuticals which emits positrons and the

obtainment of functional images[31 32]. The sensitivity of a PET scan is about 10-11-10-12 mol/L. Usually, some millions of cells that include the radioactive probe are enough to discriminate a particular phenomenon. In PET, radioisotopes emitting positrons are used following a β^- decay. These, after traveling a short distance, annihilate with an electron of the surrounding medium. As a result, of the annihilation process, they are issued simultaneously two γ-ray energy of 511keV. The two photons are emitted simultaneously along the same direction, but in the opposite direction, and their flight direction is defined using a number of detectors in time coincidence places around the patient. The angle of emission of a γ ray respect to the other is about $180°$, for which it can be assumed that the two rays traveling on the same flight line. The aim of a PET survey is to calculate the measure of the activity of local density ρ (x, y, z) of the radioisotope, such information can be obtained from linear integrals. The instrumentation must, therefore, be capable of measuring the flight lines of a pair of annihilation photons. The γ-rays are then detected through a system of temporal coincidence between the detectors which classifies the spokes as belonging to the same annihilation event. It is measured so the line of response (LOR) and software uses this information to obtain the concentration of the radioisotope. Among the disadvantages of PET, there is the toxicity of its tracers, the low resolution and the possibility of obtaining

functional information without a structural support. Furthermore, in patients with altered chemical balance, there is a limitation in the detection of tumors smaller than 1 cm. The term "radiopharmaceutical" is defined as any medicinal product which contains one or more radionuclides (radioactive nuclei). Besides that according to their chemical structure, the localization mechanism and to the therapeutic action, radiopharmaceuticals are usually classified according to the type of "positive" or "negative" display that they can produce in the specific diagnostic application[33]. In particular, a positive indicator radiopharmaceutical accumulates electively where there is the disease process, highlighting directly the area of the specific metabolic alteration; on the contrary, a radiopharmaceutical negative indicator accumulates in the normal parenchyma and functioning of an organ and, therefore, the disease is highlighted as a defect of uptake process. If the radiopharmaceutical is able to bind specifically to cancer cells, it also becomes not only therapeutic and diagnostic. For the choice of a radiopharmaceutical is important to take into consideration that it must be possible to replace an atom of common biological molecules without significantly vary the metabolic and/or behavior must have a half-life compatible with the biological half life of the carrier molecule and with the time required to marking. For these reasons, the most widely used radionuclide for PET studies is the Fluorodeoxyglucose (^{18}F-FDG). ^{18}F-FDG is a glucose analog to which a oxydrile group is substituted by a

radioactive Fluorine (F) and its decay time is about 109 minutes[30]. The radioactive fluorine is taken up by cells that use large amounts of glucose, first of all the cells of the brain, kidney, heart and cancer cells. In particular, the cancer cells have an intense glycolytic activity and therefore accumulate greater amounts of the drug. The molecule is phosphorylated at position 6, so that they can not escape from the cell. In the form of FDG-6-phosphate it can not be catabolized in the glycolytic pathway and remains in this radioactive form visible to the PET, before its decay. the use of FDG, therefore, is an excellent method to assess the biodistribution of glucose and its phosphorylation in several districts of the organism. It is an extremely precise and clean instrument, also following the decay there is no cellular accumulation of biomolecules. This radiopharmaceutical is used to diagnose and/or evaluate the progression do monitor the effectiveness of treatment for a tumor: the Hodgkin and no lymphoma and lung cancer. Its use has also been approved for the diagnosis of Alzheimer's disease. Radioactive fluorine atoms on other molecules can from life to other radiopharmaceuticals used in clinical settings as ^{18}F-DOPA and ^{18}F-ET used above all for cerebral tumor detection; ^{18}F-MISO for the detection of cellular hypoxia or ^{18}F-FLT in order to characterize the uncontrolled cellular proliferation.

Simultaneous PET/MRI

Both just described diagnostic techniques, MRI and PET, can be combined in a unique machine to provide complementary anatomic, physiologic, metabolic and functional information. Moreover, the simultaneous acquisition immediately brings to mind the possibility of improving the performance and information content of one instrument using the information obtained from another instrument: the accuracy of the PET estimates might be improved by including the MRI information as the structural framework underlying the distribution of the PET signal[34]. Reciprocally, the strength of PET to provide absolute quantitative information might help validate several MRI techniques in vivo. Simultaneous PET/MRI offers the unique option of carefully addressing these issues through accurate MRI-based motion and Partial Volume Effects (PVE) correction[35]. Furthermore, PET/MRI is a useful tool for developing a normal control database based on FDG-PET[36] since they are yet coregistered and no alignment algorithm is required, in fact T_1-weighted MR images are solid and strong and provide a great morphologic improvement in PET analysis[37] otherwise there are several concerns about the attenuation correction and segmentation. Hence the birth of an integrated system PET/MRI[38, 39], which is still little used because its use is linked to the simultaneous administration of the means of magnetic resonance contrast and radiopharmaceutical for PET, increasing side effects for the patients.

Optical Imaging and Fluorescence Tomography (FMT)

Optical Imaging is a diagnostic technique that uses light at different wavelengths in order to detect cellular and molecular function in the living body[40]. The used wavelengths are in a range that comes from ultraviolet to infrared. The contrast of the images derived from the use of reporter genes, endogenous molecules with optical signatures and exogenous agents. The Optical Imaging includes different types of techniques, which use a different kind of light in order to reach the final objective such as Bioluminescent imaging (BLI) and Fluorescence Imaging. In particular, Fluorescence imaging uses endogenous or exogenous molecules or materials that emit light when activated by an external light source as a laser[41]. A light at a specific wavelength excites a target molecule which fluoresces by releasing longer-wavelength and lower-energy light[42]. This type of diagnostic technique is able to localize and measure genes, proteins; to evaluate the cell trafficking, to tag the superficial structures, to detect lesions, to monitor tumor growing and other pathophysiologic processes. In clinical practice, the fluorescence imaging is entering initial clinical testing in areas such as breast imaging and endoscopy[43]. Respect to other diagnostic techniques the optical one is able to provide real-time information in order to support surgeon during surgery and has exquisite sensitivity and resolution[44]. However, it has a lack of mainstream clinical instrumentation, it has different limitations related to absorption and scatter and furthermore, it is not able to penetrate deeper than few centimeters.

In the last years, this technique has been very used to study small-animal models, providing unique insights into disease pathogenesis, drug development and the effects of therapy. Future development of this technique will be the design of new probes and nanomaterials which can detect lesions a few centimeters deep in tissue; the development of the probes that can be used for multimodal applications or which can release a specific enzyme or defined target[44, 45].

Theranostic

The term "theranostics" is defined as the possibility of exploiting a single agent for diagnostic and therapeutic purposes simultaneously. Administering a theranostic agent gave the possibility of being able to combine different contrast agents or radiopharmaceuticals for diagnostic technologies developed over time with the release of specific drugs or supplements for different types of diseases, tumor lesions, tissue degenerations, neurodegenerative pathologies as Alzheimer`s disease and inflammations. Nowadays, the difficult to project the design of a theranostic nanovector (TPNs) is to combine the use of biocompatible materials to exploit their properties and peculiarities in order to achieve structures that can increase the efficiency of diagnosis, increase the therapeutic effects and at the same time control that the two mechanisms occur at different times of action. Indeed, the clearance of a vector in fact is another key factor, it must be fast enough to allow the elimination of a diagnostic

agent such as a contrast medium or a radiopharmaceutical from the blood stream but sufficiently slow to allow the controlled release of a drug, a supplement or a therapeutic substance that we want to encapsulate in. The development of effective TNPs will require some give and take between imaging sensitivity, the accuracy of targeting, and controlled drug release. Via a host of materials, many pathways are being explored to reach these goals.

In the therapeutic area, there are many different methods for administering a therapeutic agent, such as administration through the oral cavity, through injection in different sites of action, through the nasal mucosa, through the use of surgically implantable devices or through drug delivery by micro and nanocarriers. Controlled Drug Delivery technology represents one of the most rapidly advancing areas that offer numerous advantages compared to conventional dosage forms including improved efficacy and reduced toxicity[46]. In addition, the diagnostic field aims to reach an even more high resolution images in order to have an early detection of different kinds of diseases.

Nanomedicine and Nanostructures

The introduction of nanotechnology has led in the course of time to the development of a large number of medical applications including the formulation of new systems for the controlled delivery of the drugs and the development of new nanometric structures that can be

used both in diagnostic and in therapeutic applications (TNPs)[47]. The unusual properties of nanoparticles can be exploited to modify the kinetics of a drug carrier for the transport of hydrophilic and hydrophobic substances, to cross biological barriers as blood brain barrier (BBB) and to highlight some diseases as tumor microenvironment or neurodegenerative diseases. The difference between natural and engineered particles is deep. While the first are generally not very reactive, biodegradable and tend to interact with each other to form clusters poorly reactive, the others are, thanks to their high surface area which exposes the surface most of the atoms that compose them, highly reactive, much less available aggregation and persist in external ambient thanks to their poor biodegradability. The use of engineered materials and the production through the different production methods allow to obtain particles with different surface charge, size, shape and texture that can be used for different types of applications. The nanoparticles can be classified for morphology and architecture into two categories: the nanospheres and nanocapsules. The nanospheres have in fact a polymer matrix inside the particle itself while the nanocapsules have a liquid core surrounded by an outer polymeric membrane[48]. In particular, the latter allows a high encapsulation power of active ingredients and substances as drugs[49]. The particles are differentiated by type of material, for surface charge, size, shape and method of preparation with which they were obtained.

The main production methods are nanoprecipitation, Emulsion-Diffusion, Double Emulsification, Polymer-Coating, Layer by Layer and Emulsion-Coacervation[48]. Between them the emulsion-coacervation method is the less explored for theranostic and multimodal imaging applications although it appears to be a method of producing highly productive. The Emulsion-Coacervation is a chemical phenomenon during which a homogeneous aqueous solution of charged macromolecules, undergoes liquid-liquid phase separation, giving rise to a polyelectrolyte-rich dense phase and to a supernatant which remains in equilibrium with the coacervate phase. These two liquid phases are immiscible and hence, are incompatible. It is important to highlight the coacervation from the precipitation process, in the last case, in fact, there is not a liquid-liquid phase separation as in the first case but a solid-liquid one. The factors that can influence the coacervation process are many and very different from each other: Ionic Strenght (Salt concentration); The polyacid/polybase ratio; Total polymer concentration; pH; Molecular weight of polyelectrolytes; Temperature. The main mechanisms of coacervation process are the desolvation of polymer, the repulsion between two different polymers that are solved in the same solvent, the interactions between a polymer poly-ions with a polymer with an opposite charge and solvation, or dissolution, which is the process of attraction and association of molecules of a solvent with molecules or ions of a solute.

There are various types of coacervation in relation to the production process used, they can be divided in: Simple coacervation (Variation of temperature, Addition of salt, Variation of pH, Addition of a non-Solvent, Addition of Incompatible Polymer) and Complex Coacervation.

In simple coacervation the addition of salt or of a non-solvent or of an incompatible polymer or the variation of same conditions promotes the coacervation. Indeed, complex coacervation of polyelectrolytes can be achieved through electrostatic interaction with oppositely charged proteins or polymers. The charges on the polyelectrolytes must be sufficiently large to cause significant electrostatic interactions, but not so large to cause precipitation.

Coacervation has been used in processed food, cosmetics, paper and textiles, and in the pharmaceutical and food industries as microencapsulates for drugs and flavours[50]. Nanoparticles produced by the method of emulsion-coacervation are based on the creation of a template emulsion on which goes to deposit the coacervate material. In the first chapter of this thesis work it will be described some different applications of nanoparticles obtained by coacervation process and if they are in vivo tested in order to understand the limitations or drawback, to study the biodistribution, the toxicity and the clearance of the NPs themselves[51][52,53].

Aim, major findings and perspectives

The aim of this thesis work is the design and the development of theranostic multimodal NPs which can be used for simultaneous MRI/PET and Optical Imaging applications. Any efforts will be given to the design of the Nanoparticles to obtain an architecture able to boost the MRI signal over the typical relaxivity of clinical relevant contrast agents. At the same time the nanovector with improved relaxometric properties should be able to deliver a radiotracer and/or an optical tracer or even a drug. A such advanced probe would avoid the administration of a cocktail of different tracers for Multimodal Imaging applications. Furthermore, an active targeting of the nanostructures will be tested in order to make it specific for a disease or an organ for both therapeutically and diagnostic applications. In particular, in the second chapter, a specific application for a lymphoma B-cell is described. The selected peptides are described in the literature to induce the reduction of tumor mass after different administration[54]. In the first chapter, a variation of the classic coacervation. Investigations report the effect of the temperature and double crosslinking to improve the stability in presence of contrast agents. The Chitosan and HA are chosen for their biocompatibility, the different degradation times and the opposite charge of each. Moreover, HA is selected for its hydrophilicity as the coacervate polymer to create the external shell of the nanoparticle. The choice of an HA with a higher molecular weight (if compared to a lower

molecular weight of Chitosan) allows the complete coating of nanodroplets template of Chitosan. The diagnostic field is one of the less explored for this production process due to the difficulty of reaching very small dimension and of integrating different kinds of tracers for multimodal applications. The process is designed to be used in industrial context for its high productivity. In vivo results are reported for MRI and Optical Imaging application while for simultaneous PET/MRI scan in vitro tests are reported.

References

1.   Vizirianakis, I. S., Nanomedicine and personalized medicine toward the application of pharmacotyping in clinical practice to improve drug-delivery outcomes'. *Nanomedicine-Nanotechnology Biology and Medicine* **2011,** *7* (1), 11-17.

2.   Pathania, D.; Millard, M.; Neamati, N., Opportunities in discovery and delivery of anticancer drugs targeting mitochondria and cancer cell metabolism. *Advanced Drug Delivery Reviews* **2009,** *61* (14), 1250-1275.

3.   Pardridge, W. M., Drug transport across the blood-brain barrier. *Journal of Cerebral Blood Flow and Metabolism* **2012,** *32* (11), 1959-1972.

4.   Therasse, P.; Arbuck, S. G.; Eisenhauer, E. A.; Wanders, J.; Kaplan, R. S.; Rubinstein, L.; Verweij, J.; Van Glabbeke, M.; van Oosterom, A. T.; Christian, M. C.; Gwyther, S. G., New guidelines to evaluate the response to treatment in solid Tumors. *Journal of the National Cancer Institute* **2000,** *92* (3), 205-216.

5.   Rossi, L.; Mazzitelli, S.; Arciello, M.; Capo, C. R.; Rotilio, G., Benefits from Dietary Polyphenols for Brain Aging and Alzheimer's Disease. *Neurochemical Research* **2008,** *33* (12), 2390-2400.

6.   Hahn, M. A.; Singh, A. K.; Sharma, P.; Brown, S. C.; Moudgil, B. M., Nanoparticles as contrast agents for in-vivo bioimaging: current status and future perspectives. *Analytical and Bioanalytical Chemistry* **2011,** *399* (1), 3-27.

7.   Schmidt, G. P.; Haug, A.; Reiser, M. F.; Rist, C., Whole-body MRI and FDG-PET/CT imaging diagnostics in oncology. *Radiologe* **2010,** *50* (4), 329-338.

8.   Harrison, V. S. R.; Carney, C. E.; Macrenaris, K. W.; Meade, T. J., A multimeric MR-optical contrast agent for multimodal imaging. *Chemical Communications* **2014,** *50* (78), 11469-11471.

9.   Janib, S. M.; Moses, A. S.; MacKay, J. A., Imaging and drug delivery using theranostic nanoparticles. *Advanced Drug Delivery Reviews* **2010,** *62* (11), 1052-1063.

10.   Marti-Bonmati, L.; Sopena, R.; Bartumeus, P.; Sopena, P., Multimodality imaging techniques. *Contrast Media & Molecular Imaging* **2010,** *5* (4), 180-189.

11.   Drzezga, A.; Souvatzoglou, M.; Eiber, M.; Beer, A. J.; Fuerst, S.; Martinez-Moeller, A.; Nekolla, S. G.; Ziegler, S.; Ganter, C.; Rummeny, E. J.; Schwaiger, M., First Clinical Experience with Integrated Whole-Body PET/MR: Comparison to PET/CT in Patients with Oncologic Diagnoses. *Journal of Nuclear Medicine* **2012,** *53* (6), 845-855.

12.   Chang, C. A., MAGNETIC-RESONANCE-IMAGING CONTRAST AGENTS - DESIGN AND PHYSICOCHEMICAL PROPERTIES OF GADODIAMIDE. *Investigative Radiology* **1993,** *28*, S21-S27.

13.   Strijkers, G. J.; Mulder, W. J. M.; van Tilborg, G. A. F.; Nicolay, K., MRI contrast agents: Current status and future perspectives. *Anti-Cancer Agents in Medicinal Chemistry* **2007,** *7* (3), 291-305.

14.   Xu, R.; Wang, Y.; Wang, X.; Jeong, E.-K.; Parker, D. L.; Lu, Z.-R., In vivo evaluation of a PAMAM-Cystamine-(Gd-DO3A) conjugate as a biodegradable macromolecular MRI contrast agent. *Experimental Biology and Medicine* **2007,** *232* (8), 1081-1089.

15.   Guglielmo, F. F.; Mitchell, D. G.; Gupta, S., Gadolinium Contrast Agent Selection and Optimal Use for Body MR Imaging. *Radiologic Clinics of North America* **2014,** *52* (4), 637-+.

16.   Caravan, P., Strategies for increasing the sensitivity of gadolinium based MRI contrast agents. *Chemical Society Reviews* **2006,** *35* (6), 512-523.

17.   Geraldes, C.; Laurent, S., Classification and basic properties of contrast agents for magnetic resonance imaging. *Contrast Media & Molecular Imaging* **2009,** *4* (1), 1-23.

18.   Doble, D. M. J.; Botta, M.; Wang, J.; Aime, S.; Barge, A.; Raymond, K. N., Optimization of the relaxivity of MRI contrast agents: Effect of poly(ethylene glycol) chains on the water-exchange rates of Gd-III complexes. *Journal of the American Chemical Society* **2001,** *123* (43), 10758-10759.

19.   Heverhagen, J. T.; Krombach, G. A.; Gizewski, E., Application of Extracellular Gadolinium-based MRI Contrast Agents and the Risk of Nephrogenic Systemic Fibrosis. *Rofo-Fortschritte Auf Dem Gebiet Der Rontgenstrahlen Und Der Bildgebenden Verfahren* **2014,** *186* (7), 661-669.

20.   Shellock, F. G.; Kanal, E., Safety of magnetic resonance imaging contrast agents. *Jmri-Journal of Magnetic Resonance Imaging* **1999,** *10* (3), 477-484.

21.   Bellin, M.-F., MR contrast agents, the old and the new. *European Journal of Radiology* **2006,** *60* (3), 314-323.

22.   Webb, J. A. W.; Thomsen, H. S.; Morcos, S. K.; Esur, The use of iodinated and gadolinium contrast media during pregnancy and lactation. *European Radiology* **2005,** *15* (6), 1234-1240.

23.   Daftari Besheli, L.; Aran, S.; Shaqdan, K.; Kay, J.; Abujudeh, H., Current status of nephrogenic systemic fibrosis. *Clinical radiology* **2014,** *69* (7), 661-8.

24.   Bernstein, E. J.; Schmidt-Lauber, C.; Kay, J., Nephrogenic systemic fibrosis: A systemic fibrosing disease resulting from gadolinium exposure. *Best Practice & Research in Clinical Rheumatology* **2012,** *26* (4), 489-503.

25.   Do, C.; Barnes, J. L.; Tan, C.; Wagner, B., Type of MRI contrast, tissue gadolinium, and fibrosis. *American Journal of Physiology-Renal Physiology* **2014,** *307* (7), F844-F855.

26.   McDonald, R. J.; McDonald, J. S.; Kallmes, D. F.; Jentoft, M. E.; Murray, D. L.; Thielen, K. R.; Williamson, E. E.; Eckel, L. J., Gadolinium Deposition after Contrast-enhanced MR Imaging Response. *Radiology* **2015,** *277* (3), 925-925.

27.   Semelka, R. C.; Commander, C. W.; Jay, M.; Burke, L. M. B.; Ramalho, M., Presumed Gadolinium Toxicity in Subjects With Normal Renal Function: A Report of 4 Cases. *Investigative Radiology* **2016,** *51* (10), 661-665.

28.   Kartamihardja, A. A. P.; Nakajima, T.; Kameo, S.; Koyama, H.; Tsushima, Y., Impact of Impaired Renal Function on Gadolinium Retention After Administration of Gadolinium-Based Contrast

Agents in a Mouse Model. *Investigative Radiology* **2016,** *51* (10), 655-660.

29.   Zhang, L.; Liu, R. Q.; Peng, H.; Li, P. H.; Xu, Z. S.; Whittaker, A. K., The evolution of gadolinium based contrast agents: from single-modality to multi-modality. *Nanoscale* **2016,** *8* (20), 10491-10510.

30.   Akamatsu, G.; Ikari, Y.; Nishio, T.; Nishida, H.; Ohnishi, A.; Aita, K.; Sasaki, M.; Sasaki, M.; Senda, M., Optimization of image reconstruction conditions with phantoms for brain FDG and amyloid PET imaging. *Annals of nuclear medicine* **2016,** *30* (1), 18-28.

31.   Weber, S.; Bruyndonckx, P.; Chatziioannou, A. F.; Clark, J. C.; Daube-Witherspoon, M. E.; Di Domenico, G.; Zavattini, G.; Honer, M.; Huber, J.; Karp, J. S.; Laforest, R.; Muehllehner, G.; Pichler, B. J.; Seidel, J.; Siegel, S.; Spinks, T.; Tai, Y. C.; Vaquero, J. J., Performance measurements of small animal positron emission tomographs. *Journal of Nuclear Medicine* **2002,** *43* (5), 59P-59P.

32.   Chan, M. H., Electron-positron pair production near the Galactic Centre and the 511 keV emission line. *Monthly Notices of the Royal Astronomical Society* **2016,** *456* (1), L113-L116.

33.   Melendez-Alafort, L.; Nadali, A.; Zangoni, E.; Banzato, A.; Rondina, M.; Rosato, A.; Mazzi, U., Biokinetic and dosimetric studies of Re-188-hyaluronic acid: a new radiopharmaceutical for treatment of hepatocellular carcinoma. *Nuclear Medicine and Biology* **2009,** *36* (6), 693-701.

34.   Catana, C.; Drzezga, A.; Heiss, W.-D.; Rosen, B. R., PET/MRI for Neurologic Applications. *Journal of Nuclear Medicine* **2012,** *53* (12), 1916-1925.

35.   Rousset, O. G.; Ma, Y. L.; Evans, A. C., Correction for partial volume effects in PET: Principle and validation. *Journal of Nuclear Medicine* **1998,** *39* (5), 904-911.

36.   Dukart, J.; Mueller, K.; Horstmann, A.; Vogt, B.; Frisch, S.; Barthel, H.; Becker, G.; Moller, H. E.; Villringer, A.; Sabri, O.; Schroeter, M. L., Differential effects of global and cerebellar

normalization on detection and differentiation of dementia in FDG-PET studies. *Neuroimage* **2010,** *49* (2), 1490-1495.

37.   Friston, K. J.; Holmes, A.; Poline, J. B.; Price, C. J.; Frith, C. D., Detecting activations in PET and fMRI: Levels of inference and power. *Neuroimage* **1996,** *4* (3), 223-235.

38.   Mosconi, L.; Tsui, W. H.; Pupi, A.; De Santi, S.; Drzezga, A.; Minoshima, S.; de Leon, M. J., F-18-FDG PET database of longitudinally confirmed healthy elderly individuals improves detection of mild cognitive impairment and Alzheimer's disease. *Journal of Nuclear Medicine* **2007,** *48* (7), 1129-1134.

39.   Yankeelov, T. E.; Peterson, T. E.; Abramson, R. G.; Garcia-Izquierdo, D.; Arlinghaus, L. R.; Li, X.; Atuegwu, N. C.; Catana, C.; Manning, H. C.; Fayad, Z. A.; Gore, J. C., Simultaneous PET-MRI m oncology: a solution looking for a problem? *Magnetic Resonance Imaging* **2012,** *30* (9), 1342-1356.

40.   Hespos, S. J., What is Optical Imaging? *Journal of Cognition and Development* **2010,** *11* (1), 3-15.

41.   Kwong, T. C.; Lo, P. A.; Cho, J.; Nouizi, F.; Chiang, H. H. K.; Kim, C. S.; Gulseni, G., Multi-wavelength Fluorescence Tomography. In *Design and Quality for Biomedical Technologies Ix*, Raghavachari, R.; Liang, R., Eds. 2016; Vol. 9700.

42.   Chang, J. W.; Barbour, R. L.; Graber, H.; Aronson, R. In *Fluorescence optical tomography*, Conference on Experimental and Numerical Methods for Solving Ill-Posed Inverse Problems - Medical and Nonmedical Applications, San Diego, Ca, Jul 10-11; San Diego, Ca, 1995; pp 59-72.

43.   Napp, J.; Mathejczyk, J. E.; Alves, F., Optical imaging in vivo with a focus on paediatric disease: technical progress, current preclinical and clinical applications and future perspectives. *Pediatric Radiology* **2011,** *41* (2), 161-175.

44.   Hadjipanayis, C. G.; Jiang, H. B.; Roberts, D. W.; Yang, L., Current and Future Clinical Applications for Optical Imaging of Cancer: From Intraoperative Surgical Guidance to Cancer Screening. *Seminars in Oncology* **2011,** *38* (1), 109-118.

45.   Luker, G. D.; Luker, K. E., Optical imaging: Current applications and future directions. *Journal of Nuclear Medicine* **2008,** *49* (1), 1-4.

46.   Cho, K.; Wang, X.; Nie, S.; Chen, Z.; Shin, D. M., Therapeutic nanoparticles for drug delivery in cancer. *Clinical Cancer Research* **2008,** *14* (5), 1310-1316.

47.   Azzawi, M.; Seifalian, A.; Ahmed, W., Nanotechnology for the diagnosis and treatment of diseases Foreword. *Nanomedicine* **2016,** *11* (16), 2025-2027.

48.   Mora-Huertas, C. E.; Fessi, H.; Elaissari, A., Polymer-based nanocapsules for drug delivery. *International Journal of Pharmaceutics* **2010,** *385* (1-2), 113-142.

49.   Karponis, D.; Azzawi, M.; Seifalian, A., An arsenal of magnetic nanoparticles; perspectives in the treatment of cancer. *Nanomedicine* **2016,** *11* (16), 2215-2232.

50.   Priftis, D.; Tirrell, M., Phase behaviour and complex coacervation of aqueous polypeptide solutions. *Soft Matter* **2012,** *8* (36), 9396-9405.

51.   Mao, H. Q.; Roy, K.; Troung-Le, V. L.; Janes, K. A.; Lin, K. Y.; Wang, Y.; August, J. T.; Leong, K. W., Chitosan-DNA nanoparticles as gene carriers: synthesis, characterization and transfection efficiency. *Journal of Controlled Release* **2001,** *70* (3), 399-421.

52.   Elzoghby, A. O., Gelatin-based nanoparticles as drug and gene delivery systems: Reviewing three decades of research. *Journal of Controlled Release* **2013,** *172* (3), 1075-1091.

53.   Zhao, K.; Zhang, Y.; Zhang, X.; Li, W.; Shi, C.; Guo, C.; Dai, C.; Chen, Q.; Jin, Z.; Zhao, Y.; Cui, H.; Wang, Y., Preparation and efficacy of Newcastle disease virus DNA vaccine encapsulated in chitosan nanoparticles. *International Journal of Nanomedicine* **2014,** *9*, 389-402.

54.   Palmieri, C.; Falcone, C.; Iaccino, E.; Tuccillo, F. M.; Gaspari, M.; Trimboli, F.; De Laurentiis, A.; Luberto, L.; Pontoriero, M.; Pisano, A.; Vecchio, E.; Fierro, O.; Panico, M. R.; Larobina, M.; Gargiulo, S.; Costa, N.; Dal Piaz, F.; Schiavone, M.; Arra, C.; Giudice,

A.; Palma, G.; Barbieri, A.; Quinto, I.; Scala, G., In vivo targeting and growth inhibition of the A20 murine B-cell lymphoma by an idiotype-specific peptide binder. *Blood* **2010,** *116* (2), 226-238.

CHAPTER 1

1 Hybrid Core-Shell (HyCoS) Nanoparticles Produced by Complex Coacervation for Multimodal Applications
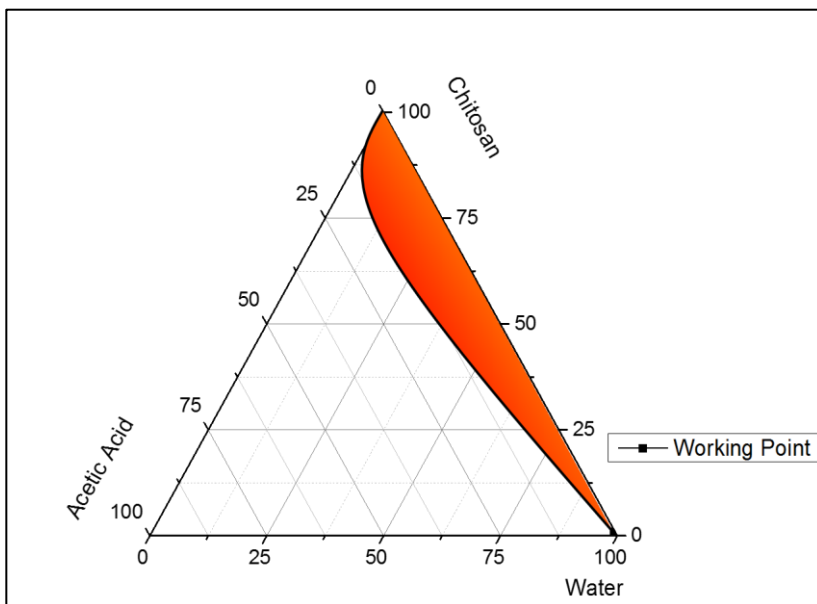
*Figure 1-1: **Graphical representation:** Ternary system Ch-CH$_3$COOH-H2O. The red area represents the miscibility range of Chitosan into an Acetic Acid solution.*

1.1 Introduction

Coacervation is defined as a spontaneous formation of a dense liquid phase from a macromolecular solution of poor solvent affinity. The Emulsion-Coacervation processes are considered a scalable, reproducible and relatively low-cost approaches; furthermore, they provide main advantages in terms of high payload (up to 99%) and controlled release properties. The coacervation process is primary used for the production of micrometric morphologies but thanks to the optimization of the process parameters different authors have presented some applications of nanoparticles obtained by coacervation process[5,7]. Furthermore, nanocapsules by coacervation are used in many different applications as drug delivery system in medicine and in food or cosmetic industries. In medicine, they are used both in therapeutic and in diagnostic applications. The ability of nanoparticles to manipulate the molecules and their structures has revolutionized the conventional drug delivery system[1]. Among materials that are used for nanoparticles production by coacervation there are many polymeric materials as PEG, PLLA, HA, Chitosan and other natural components as gum arabic, jelly or legumin[2]. Chitosan nanoparticles are usually applied because of their biodegradability, biocompatibility, better stability, low toxicity, simple and mild processing conditions and furthermore they offer a valuable tool to novel drug delivery systems in the present scenario[3]. Chitosan in a work by Lee et al. was applied for the production of

nanoparticles encapsulating siRNA[4]. Arnedo et al. [5] produced by coacervation albumin nanoparticles for drug delivery for antisense oligonucleotides[5]. The same type of nanoparticles was used by Das et al. to encapsulate Aspirin, a common anti-inflammatory and anti-platelet agent widely used for various conditions[6]. Other application of Coacervate nanoparticles came by Gallarate et al in 2010[1], where solid lipid nanoparticles for the encapsulation of peptides[1] were described. Differently from the simple coacervation, previously described, following different cases study of complex coacervation exploiting the combination of more materials as the HA and the Chitosan will be presented [4, 5, 7]. This method is called Complex Coacervation because is based on the phase separation of more than one encapsulation agent. In 2000 Mao et al. [8] obtained Chitosan-DNA nanoparticles (GNPs) by Complex Coacervation. The size of particles was optimized to 100-250 nm, with a composition of 35.6% and 64.4% by weight of DNA and Chitosan. The particles encapsulated plasmid DNA (GNPs) from nuclease degradation. Various types of crosslinkers were used to improve the physiochemical properties of GNPs, including aldehydes, genipin, carbodiimide/N-hydroxysuccinimide, and transglutaminase[8]. The GNPs, thanks to their biocompatibility and biodegradability, were chosen for the ocular drug delivery In 2014 Zhao et al. [9] created optimal preparation conditions of Newcastle disease virus (NDV) F gene deoxyribonucleic acid (DNA) vaccine encapsulated in Chitosan

nanoparticles (pFNDV-CS-NPs) through a Complex Coacervation process. In the application of the nanotechnology to the medical field (nanomedicine), optimization of the size is one of the most important parameters to perform an efficient delivery and overcome biological barriers reaching a specific organ or a tumor mass[10]. The production by complex coacervation of nanoparticles to be applied in the diagnostic field has not been fully explored/investigated because of the complexity to control all the process parameters simultaneously considering the concurrent presence of more than one active compounds. However, the exploitation of this approach could bring to the combination of different contrast agents, drugs and polymers before being processed or the use of not completely biocompatible materials, solving typically unstable behavior related to the nanoparticles in the diagnostic applications[7]. In 2008 Huang et al. [11] have presented a system in which polyelectrolytes complex (PECs) of 300nm in diameter were formed by a complex Chitosan Coacervation with dextran sulphate and presented nanoparticles having colloidal stability in simulated serum. The Gd was incorporated through two different procedures: first of all the DTPA with Gd chelate was grafted into Chitosan before the complexation with dextran sulphate. Then, the Gd was also incorporated into PECs, mixing them with $GdCl_3$, resulting in ionic trapping of Gd ions within the PECs. Another application of nanoparticles obtained by Coacervation process in MRI detection was discussed by

Saboktakin et al. in 2010, who used Chitosan–dextran sulphate (DS) nanoparticles coated with iron oxide as drug transporters, detectable using the magnetic resonance imaging (MRI) technique[12]. Studying various parameters such as pH, the concentration of the polymers, the percentage of crosslinkers, the reaction temperature and the volume of the different phases, Liu et al.[7] have shown how to develop a stable micro-system in an aqueous environment in the presence of an encapsulated chelate contrast agent too. The possibility to design a core-shell architecture thanks to coacervation process makes the vectors useful for theranostic or multimodal diagnostic applications combining different tracers or drugs. On the basis of the previously reported results, the application of the complex coacervation based processes to the production of nanoparticles forAdvanced Multimodal Imaging applications seems to be very promising. Indeed, despite the recent advances in the single diagnostic techniques[13], the study on diagnostic technology is still continuous, and it focuses on the disparity of diseases and the type of information provided by the single techniques[14]. In this scenario fits the Multimodal Imaging because it can combine two or more techniques based on different physical principles allowing the integration of functional information to structural ones[15], overcome limitations of the single diagnostic techniques and optimize therapies leading to a "personalized medicine"[16]. Among the multimodal applications, Nuclear Magnetic Resonance-Optical dual imaging

modality has the principle advantage to be completely free from ionization rays while anatomical and molecular, physiological or metabolic information are provided. Magnetic Resonance Imaging (MRI) is characterized by a relatively high spatial resolution, relatively no tissue penetrating limits but also it has a low sensitivity, high cost and long imaging time.

Differently from MRI, Optical Imaging has a higher sensitivity; it is a multicolor Imaging which allows visualizing target biological molecules (peptides, drugs, etc.) but it presents a low spatial resolution and a poor tissue penetration. Among different optical techniques, the Fluorescence Molecular Tomography (FMT) produces quantified 3D reconstructions of fluorescence activation or concentration. In this framework, their combination can provide information not available typically by applying the single methodologies and allows to distinguish finely in different tissues within the body[17]. The introduction of nanotechnology has led to the development of many medical products including the formulation of new probes that can be used for multimodal applications[18-22]. Among them, nanovectors can potentially provide early diagnosis and monitoring of therapeutic response [23, 24] and play a significant role in the dawning era of personalized medicine[25-27]. Nowadays, although many efforts are made in the development of instrumentations for Multimodal Imaging, this field still lacks biocompatible, biodegradable and Food and Drug Administration (FDA) approved

probes[28]. In literature, different studies about dual imaging MRI and Optical Imaging are reported [21, 29, 30]. In 2009, Xie et al. [31] produced Iron oxide nanoparticles (IONPs) for PET/NIRF/MRI applications labeled with Cy5.5 dye and ^{64}Cu-DOTA chelates. In the same period, Chen et al. [32] presented the IONPs nanoparticles coated with a PEGylated amphiphilic triblock copolymer conjugated with a near-infrared fluorescent (NIRF) dye IR-Dye800 and with a ^{64}Cu-DOTA chelates. In 2010, Nam et al. [33] reported tumor targeting nanoparticles for optical/MRI dual imaging based on self-assembled Glycol Chitosan (GC) which was chemically modified with 5β-Cholanic Acid (CA). For optical imaging, (GC-CA) was used as a chelate for Gd(III) and Cy5.5 was conjugated. Tan et al. [34] in 2011, presented a multimodal imaging system by co-encapsulating superparamagnetic iron oxides (IOs) and Quantum Dots (QDs) in Poly(lactic acid)-d-αtocopheryl polyethylene glycol 1000 succinate (PLA-TPGS). Then, in 2013 Huang et al. [35] produced $Mn_3[Co(CN)_6]^2$ nanocubes that can serve as MRI agents and two-photon fluorescence (TPF). Tian et al. in 2013, reported core-shell Fe_3O_4-Cu_9S_8 nanoparticles for dual-modal imaging and photothermal therapy [36], useful as a probe for T_2.

Among different probes, those combining MRI and FMT imaging modalities have been used to evaluate morphological and functional changes in tumors in response to chemotherapy by monitoring tumor growth and protease activity[37]. Currently, nanoparticles obtained by

coacervation for applications in MRI as contrast medium have been evaluated to allow the increase of the signal encapsulating substances such as Gd chelates, whose free molecule is toxic into the body[30].

As previously reported until now most of the efforts have been limited to grafting contrast-enhancing agents to the surface of hydrophobic particles where access to water is achievable or to enhance the delivery by an effective encapsulation[11]. In this chapter, is presented a Complex Coacervation Method to produce Hybrid Core-Shell NanoParticles (HyCoS NPs) made of a Chitosan-core and a Hyaluronic Acid-shell, and to the control of their properties for application in the MRI and Optical Imaging Field. Indeed, HyCoS NPs are designed to entrap rationally a relevant clinical CA, Gd-DTPA, enhancing its MRI performances and delivering an effective amount of optical tracer sufficient to achieve a high-intensity signal.

These nanovectors are engineered to own these peculiar properties and, at the same time, preserve fundamental characteristic of the delivery (e.g. size, charge, choice of shape and materials)[10, 38]. Furthermore, many efforts are made to overcome the interference of MRI agent with the coacervation process introducing a double crosslinking reaction, an intrachain crosslinking (between polymer chains of core-shell) and an interchain one (between the polymer chains of the shell), able to improve the stability of the system. Then, using the temperature, the proposed process has been speeded up to reduce the reaction time and stabilize the architectures.

1.2 Materials

1.2.1 NPs Production

Chitosan (Ch) low molecular weight; Divinyl Sulfone (DVS) 118.15 g/mol; Sodium Tripolyphosphate (TPP) 367.86 g/mol; Glacial Acetic Acid (CH₃COOH) molecular weight 60.05; Ethanol (EtOH) molecular weight 46.07; Gd-DTPA molecular weight 547.57; Mineral Oil 0.84 g/mL at 25°C (lit.); Span80 molecular weight 274.43; 1.005 g/mL at 20 ℃ (lit.); while Hyaluronic Acid (HA) 850 kDa parenteral grade is by Hyasis. MilliQ water is for all experiments.

1.2.2 Reactants used for the functionalization of NPs

EDC (1-ethyl-3-(3-dimethylaminopropyl) carbodiimide hydrochloride), NHS (N-hydroxysuccinimide) and Streptavidin are purchased by Sigma-Aldrich. Dyes (Cy5, Atto 633, FITC) are purchased by Sigma-Aldrich®.

1.3 Method of HyCoS NPs Production

1.3.1 Evaluation of the Phase behavior of the Ch-Acetic Acid-Water system

The behavior of the Ch- CH₃COOH-water system is evaluated experimentally starting from 1ml of water in which are added Ch and CH₃COOH at different percentages alternatively. After each addition, the vial is stirred for 15 min. After the behavior of the Ch-CH₃COOH-water system is observed, if the system resulted

completely solved that point was indicated on the ternary diagram with a green spot, alternatively with a red one. The region, in which the behavior of the ternary system is only partially dissolved, is displayed with a black line to underline the difference between the two different behaviors.

1.3.2 Emulsion preparation to produce core-shell nanoparticles by complex coacervation

A Complex Emulsion-Coacervation is used for the production of HyCoS nanostructures.

The first step consists in the preparation of a w/o emulsion (5%/95% v/v) used as a template. The water phase is made of an aqueous solution of Ch and CH_3COOH 8% v/v obtained by mixing 5 ml of MilliQ water at a Ch concentration ranging from 0.1% wt/v to 1% wt/v. Due to the hydrophobic nature of the Ch, the greater is the percentage of CH_3COOH in the solution; the lower is the gap of miscibility between Ch and water. The oil phase is obtained by dissolving the surfactant Span80 (0.5-1% wt/v) in 45 ml of Mineral Oil and homogenizing for 5min at 7000rpm (by L5MA purchased by Silverton). The primary emulsion, obtained by mixing both phases, is treated for 20 minutes at 7000 rpm. Then, the solution containing HA, as coacervate polymer, is added dropwise and the final volume is homogenized at 7000 rpm for further 30 min, keeping constant the Temperature at 37 °C. In a different preparation, a clinical relevant Contrast Agents (CAs), Gd-DTPA, at a concentration of 18 mM, is

added to the aqueous solution containing Ch before mixing to the oil phase. When Gd-DTPA is added to the aqueous solution, the preferred volume of CH_3COOH is of 10 μL to balance the acid nature of Gd-DTPA and to re-establish the pH conditions from 4.5 to 5 able to favor the activation of the –COOH group. The final concentration of Gd-DTPA within the total emulsion is of 1.8mM. After the preparation of a stable primary emulsion, the coacervant phase, composed of 0.1% wt/v HA in a water solution of 3ml at 30% wt/v, is added dropwise to the w/o emulsion template and homogenized at 7000 rpm for 30 min. The pH and temperature are continuously monitored and kept at a value ranging from 4.5 – 5. Coacervation starts as soon as HA reaches the surface of the droplet template containing the chitosan solution. Two crosslinking agents are added to the phases, to improve the stability of the coacervate. The preferred formulation is the addition of TPP to the coacervant phase and DVS to the aqueous phase. TPP concentration ranges from 20 – 40%wt/v increasing the pH of the coacervant phase to 10-11. The addition of DVS (8-24%v/v) to the aqueous phase kept the pH condition at the constant value of 4.5-5. DVS is always added to the aqueous phase to avoid an uncontrolled crosslinking reaction. The total formulation is stirred overnight at 300rpm at T ambient until coacervation completely occurs. Time of homogenization is also studied by stirring the w/o emulsion for 5-10-15 or 20 min at 7000rpm while the coacervation step is performed at 30 and 60 min

at 7000 rpm. In different protocols, the effect of the Temperature is also tested and the coacervation step is maintained at high constant temperature for 6h to promote the evaporation of the CH_3COOH or a controlled Temperature profile is performed from 40 to 23 °C. To follow the development of the chemical reaction, few microliter of the emulsion are collected at different time points and the formation of the nanoparticle is attempted by SEM.

1.3.3 Evaluation of Encapsulation Efficiency and Loading Capability

To study the Encapsulation Efficiency (EE) and the Loading Capability (LC) of several specific dyes, Cy5, Atto 633, FITC, are alternatively added to the aqueous phase at concentrations ranging from 0.1 to 1 mg/mL. For the determination of the EE and LC the protocol proposed by Ankrum et al. is followed[39]. Furthermore, Induced Coupled Plasma (ICP-MS) - NexION 350 by Perkin Elmer is used to assess the concentration of the metal chelate in the nanoparticle suspension. Nanoparticles were suspended in a solution of deionized (DI) water at a concentration of 150.000 particles/ml. All data are collected and processed using the Syngistix Nano Application Module. Gd is measured at m/z 157 using a 100 µs dwell time with no settling time.

1.3.4 Bioconjugation of the HyCoS NPs

230 µl of a solution of EDC at 70mM and 230 µl of a solution of NHS at 21mM are added to 500 µl of NPs to activate the carboxylic

groups on the external shell of HA. After 10 min of stirring, 40 µl of the selected dye are added. The conjugation reaction is kept under continuous stirring for two hours at room temperature. Purification protocols are performed to wash away the residual reaction components by dialysis or ultracentrifugation. The behavior of the NPs is observed in a range of pH values between 4.3 and 7. These pH values are chosen because: 4.3 is the inferior limit of the range in which the NPs result to be stable while 7 is the pH value at which in general are administred the injectable solutions in clinical practice.

HCl and NaOH are added to reach the selected pH values. In particular, 8 µl of a solution 1M of HCl are added to 5 ml of NPs to reach the pH of 4. Then, the suspension is split into 10 batches of 500 µl and kept under continuous stirring for 24h. NPs, hold at pH 4, are observed at different time points, 30 min, 1h, 2h, 3h, 6h, 8h, 12h, 24h by SEM. Alternatively, NPs are treated at pH 7, by adding 10 µl of a NaOH solution at 1M to 5 ml of the aqueous phase containing NPs at pH value of 5.5. The observation of NPs at pH 7 is done after 30 min, 1h, 2h, 3h, 6h, 8h, 12h, 24h at SEM. The experiments are repeated in triplicate.

1.3.5 Characterization of HyCoS Nanoparticles

A Field Emission Scanning Electron Microscope (FE-SEM) by Zeiss, Transmission Electron Microscope (TEM) by FEI® in DRY, CRYO and Tomography (TOMO) modes, Confocal Microscope (STED Stimulated Emission Depletion) and IR spectroscopy Thermo

are used in order to characterize morphologically and chemically the system. The SEM characterizations are made after 48 h of stirring withdrawing 200µl of the reaction and diluting in 50 ml of EtOH, after an ultracentrifugation (UC condition 15.000rpm 10min 4°C) and after the dialysis to control the integrity of the nanostructures. The SEM observations are made by collecting nanoparticles on an ISOPORE membrane of 100nm pore size. Nanoparticles are coated with 7nm Au or PtPd prior observation. The TEM analyses are conducted both in DRY, CRYO and Tomography (TOMO) modes. In the DRY mode, the samples are prepared using Formvar/Carbon 200 mesh Cu Agar using 20µl of the suspended nanoparticles. In CRYO mode the samples are prepared using VITROBOT FEI coating Lacey Carbon film 200 mesh Cu Agar with 3µl of nanoparticles suspension. The conditions of VITROBOT are blotting time 1s, humidity upper than 70% and temperature 20°C. Confocal Microscopy (Stimulated Emission Depletion) STED is used to evaluate the fluorescence of encapsulated or conjugated NPs. The observed samples are prepared by drying 20µl of nanoparticles suspension deposited in a FluorDish. FT-IR studies are conducted to investigate the interaction among Ch, TPP and HA in the nanoparticles formation process. The IR analysis is obtained by measuring solid samples of raw Chitosan, HA and TPP while 150µl of HyCOs NPs are deposited on silicon wafers to avoid interference.

1.3.6 In Vitro MRI

Analyses with Minispec 60mq BRUKER are performed to evaluate the relaxation times. 300µl of nanoparticles' suspension (1mg/ml) or Gd-DTPA solution are loaded within a glass tube. The Free Induction Decay sequence (FID) is used to evaluate the best value of the Gain to control the saturation of the signal and measure and to measure T_2^* signal. In addition, the Saturation Recovery and Inversion Recovery sequences are used to measure T_1 signal while the Carr-Purcell sequence (CPC) to evaluate T_2. The relaxation times distribution is obtained by CONTIN Algorithm. The relaxation spectrum is normalized with respect to the CONTIN processing parameters. The integral of a peak corresponds therefore to the contribution of the species exhibiting this peculiar relaxation to the relaxation time spectrum[40]. Experiments are repeated at least five times.

1.3.7 MRI acquisition on C57 bulb mice model

Animal studies are performed after approval of the Institutional Animal and Care Committee of the CEINGE, Biotecnologie Avanzate and the Italian Ministry of Health, Protocol n° 49/2015-PR e n° 50/2015-PR, in accordance with European guidelines of the 2010/63/EU Directive on the protection of animals used for scientific purposes.

All studies are performed on SWR/J mice model under general anesthesia, obtained with an intraperitoneal injection of

tribromoethanol solution at a final concentration of 12.5 mg/ml and administered at a dosage of about 250 mg/kg. Once anesthetized, mice are prepared for venous cannulation by bathing the whole tail in tap water warmed at 39.0°C to obtain proper vasodilation. A lab-made catheter, consisting of a 30 G needle mounted on a polyethylene tube, is delicately advanced in one of the lateral caudal veins, until blood could be seen in the tube. Hence, two-three drops of surgical glue are spilled on the needle /tail interface area and let dry. The tube is flushed with 20 µL of a heparinized solution and the tip of the tube is closed to avoid further bleeding. The mice are then positioned on magnetic compatible bedding within a head coil and the baseline acquisition is performed. Hereafter, 150 µL of the contrast agent solution is slowly injected, following any eventual reaction of the mouse or any change in the respiratory pattern. Acquisitions are performed every 10 minutes till one hour post injection, and then after three, six, eight and 24 hours. Following, the MRI protocol of acquisition for PET/MRI 3T Siemens reported. A basal MRI Acquisition has been conducted for all animals before the first Injection Protocol as control. T1_TSE_FS_CORE_192_1.2 Sequence is used for each acquisition. Following the main are reported the mail parameters of the used sequence.

Sequence Name: T1_TSE_FS_CORE_192_1.2
Slices: 1.2 mm (without GAP, contiguous slice)
Averages: 6

Turbo spin-echo

Sequence duration: 10 minutes -36 seconds

Signal to Noise Ratio: 1

VOF: 100 x 75

Matrix: 192 x 144

Spatial Resolution: 0.5 x 0.5

TR: 550

TE: 11

Saturation Sequence of fat (visible signal in kidneys after 3 hours).

150μl of HyCoS NPs 40μM (T_1 700 ms) are injected to each subject. Flip Angle is kept constant because the slices are very small.

After each injection, a MRI scan is performed at different time points to control the Gd-NPs distribution.The acquisition time is 10 minutes.

In the following table, the time points at which the MRI scans are performed after the administration of the dose are reported for each of the three tested subjects.

Subject	Time Point (h)
T1	0:00
	0:10
	0:20
	0:30
	0:40
	0:50
	3:00
	4:00
	24:00 (1 d)
	192:00 (8d)
T2	0:00
	0:10
	0:20
	0:30
	0:40
	0:50
	3:00
	24:00 (1 d)
	192:00 (8d)
T3	0:00
	0:10
	0:20
	0:30
	0:40
	0:50
	192:00 (8d)

*Table 1: **MRI acquisition at different time points:** After the injection of the nanoparticles, Animals are scanned at different time points to follow the biodistribution of the complex.*

After 8h the organs of each subject (liver, Kidney, lung, spleen, heart, blood and brain) are collected and weighted to be analyzed by ICP/MS. These analyses allow to evaluate the concentration of Gd-DTPA in each organ for each subject.

The DICOM files of each acquisition were stored on an external unit. The files were imported in dedicated software for imaging analysis (OsiriX$^{©}$ Lite, Pixmeo SARL, Bernex, Switzerland). A circular region of interest (ROI) of about 2 mm^2 was drawn and then saved, to be used in the analysis of all images. The anatomic areas studied were: renal cortices and medullas, the urinary bladder, the salivary glands. The mean intensity obtained for each organ (I_O) was normalized to the mean muscle intensity (I_M) applying the formula: $I_{Onorm} = I_O / I_M$, and the result was used to calculate the percentage of contrast enhancement (%CE) %CE $= [(I_{post} - I_{pre}) / I_{pre}] * 100$.

1.4 Results

1.4.1 Phase behavior of the Ch-CH$_3$COOH-Water system

Our first step is devoted to the understanding of the phase diagram of the ternary system Water-CH$_3$COOH –Ch (Figure 1- 2) to improve the knowledge and, therefore, the stability of the aqueous phase of the emulsion template. The thermodynamic system is extremely complex and sensitive to small changes in concentration among the components. The low solubility of the Ch creates a gap of miscibility that is overcome by adding the CH$_3$COOH dropwise. The ternary diagram reported in Figure 1- 1, is built analyzing the behavior of Ch at different concentrations of the CH$_3$COOH solution. The red working points show the concentrations at which the polymer is not dissolved into the solution while the green working points display the complete dissolution of the polymer chains. The black line, which

draws the border of miscibility gap, shows a scratched transition area between the two different behaviors. For a concentration of 1% of Ch, the complete dissolution of Ch in 5 mL of water is reached only at 2μl/ml of CH$_3$COOH.

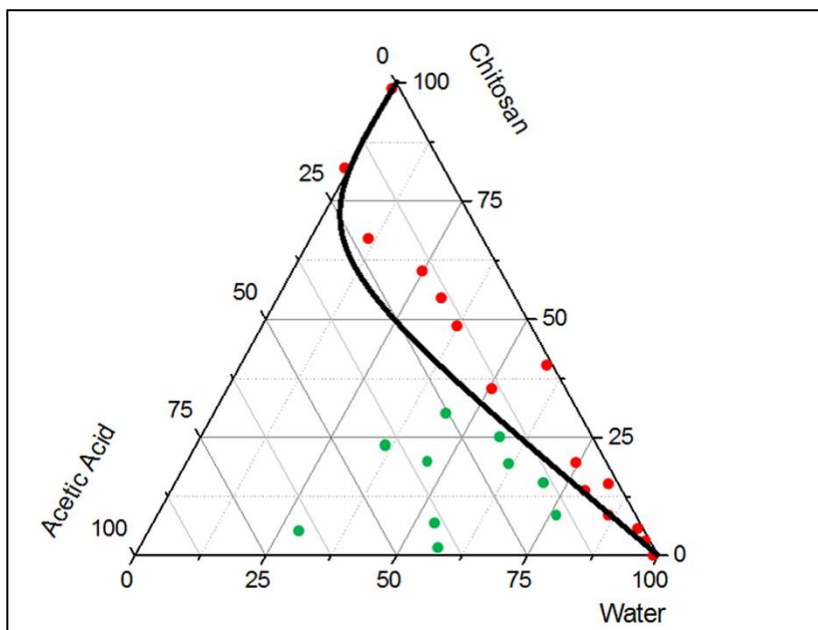Figure 1-2: **Experimental determination of the Phase Diagram of the ternary system Water-Acetic Acid-Chitosan.** Phase diagram is obtained adding dropwise the acetic acid to the Chitosan and Water, allowing the complete dissolution of the polymer. The green spots (-●-) represent the working point showing the complete dissolution of the polymer. The line drafts the miscibility gap between the two different behaviors.

1.4.2 Preparation of the Hybrid Core-Shell Nanoparticles (HyCoS NPs).

Nanoparticles are produced by coacervation performed at 0,1 % wt/v HA, 1% wt/v Ch, 30% wt/v TPP, showing a stable behavior also in water. However, when Gd-DTPA is added to the aqueous phase at the ratio 1:1 GdCA:Ch, morphologies of the nanoparticles results irreversibly compromised in water (Figure 1- 3). Indeed, even if the coacervation is properly occurred in the presence of Gd-DTPA, as observed in Figure 1- 3A and 3B reporting nanoparticles in EtOH, the spherical shape is not preserved in water and dissolved completely just after few minutes. This evidence shows a strong interference of Gd-DTPA with the crosslinking reaction that weakens the effectiveness of the coacervation. To avoid the instability of the architectures in the presence of Gd-DTPA, we have proposed the introduction of a second crosslinker, DVS able to create bis-sulfovylnil linkage between OH groups of HA[41, 42].

Figure 1-3: **Morphological characterization of nanoparticles by Fe-SEM**: *Coacervation performed at 0,1% wt/v HA, 1% wt/v Chitosan, 30% TPP wt/v, Gd-DTPA:Chitosan 1:1. (A) and (B) NPs collected in EtOH while (C) NPs collected in water. Results clearly show that if Gd_DTPA is added to the solutions, the stability of the CoA NPs in water is compromised and the spherical core-shell morphologies are not preserved.*

Adding the different percentage of DVS (8%, 16%, 24% v/v), it is noticed that there are also some regular swelling phenomena by increasing the volume of DVS for NPs with and without Gd-DTPA (Figure 1- 4A-C). Indeed, NPs maintain their structures, avoiding the complete dissolving phenomena only at DVS concentration of 8% v/v (Figure 1- 4A). At percentage of DVS higher than 8% v/v, (Figure 1- 4B and C) there is an increase in the size of the nanoparticles and the production of some irregular shapes. This effect is probably due to

interference between DVS and the system caused by a partial reaction of the crosslinker with the hydroxyl –OH groups of HA (Figure 1- 4B and C).
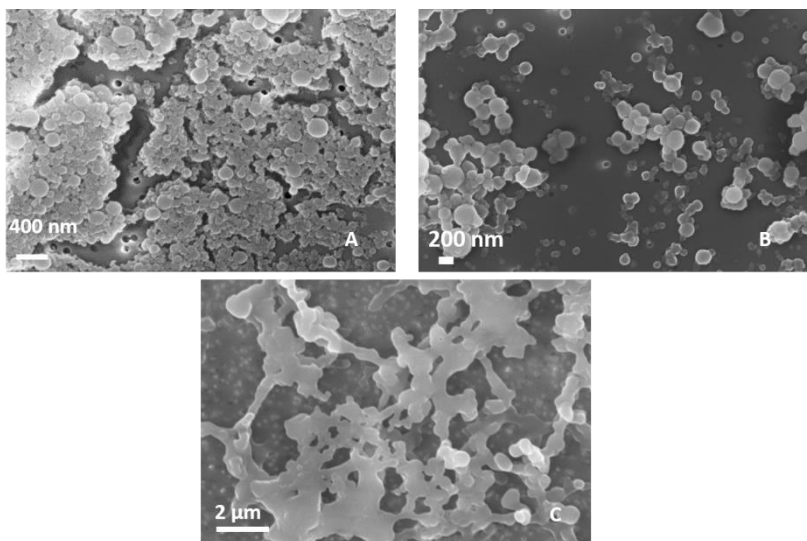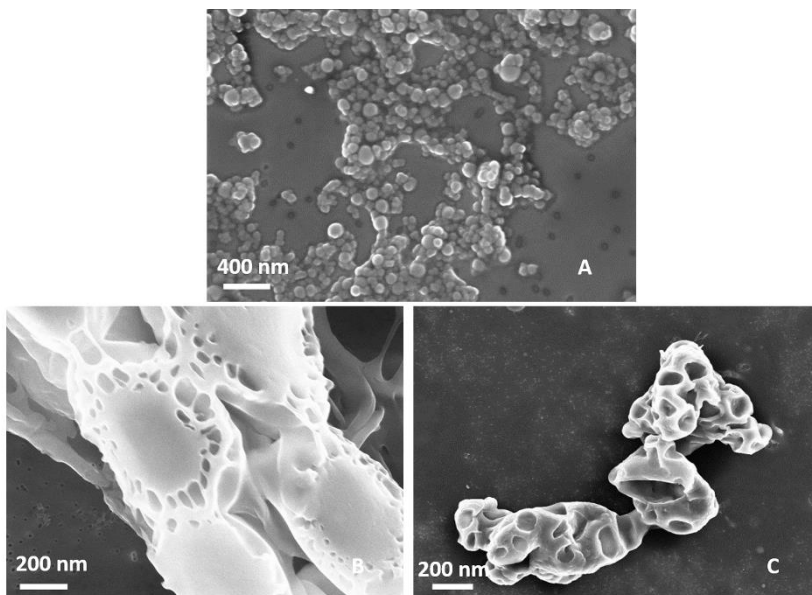

Figure 1-4: *Morphological characterization of nanoparticles by Fe-SEM:* Coacervation performed at 0,1% wt/v HA, 1% wt/v Chitosan, 30% TPP wt/v, Gd-DTPA: Chitosan 1:1. NPs collected in water obtained by using DVS at (A) 8% v/v ; (B) 16% v/v ; (C) 24% v/v DVS collected in water. Panel reports how the stability of the c ore shell nanovectors is reached only for DVS at 8 % v/v.

1.4.3 FT-IR analysis

To confirm the effectiveness of the chemical reaction, an FT-IR analysis is performed. Indeed, the favorable pH conditions reported

in the literature for HA and DVS[41] are not properly reached in our system, and an FT-IR study is conducted to investigate the interaction between the two polymers (Ch and HA) and the crosslinkers (TPP and DVS). In Figure 1- 5 of spectra of Ch-HA nanoparticles is shown. A band at 3450 cm^{-1} that can be attributed to $-NH_2$ and $-OH$ group stretching vibration in chitosan matrix is currently not detected in the spectra of HyCoS NPs particles[7]. The characteristic bands at 1658.64 cm^{-1} and 1730.92 cm^{-1} is attributed to C=O group stretching vibration in the HA matrix. A new sharp peak 1641 cm^{-1} has emerged and the 1585 cm^{-1} peak of $-NH_2$ bending vibration has shifted to 1582 cm^{-1}. Because of $-NH_2$ bending vibration shifts, the features bands at 1614 cm^{-1} and 1405 cm^{-1} have shifted to 1641 cm^{-1} and 1377 cm^{-1}respectively. The presentation of P=O vibration absorption at 1269 cm^{-1} is observed, indicating the reaction between Ch and TPP. The peaks at 2953.42 cm^{-1}, 2922.48 cm^{-1} and 2853.39 cm^{-1} show the -CH interaction. The characteristic peaks for DVS show absorptions at 1119.76 cm^{-1} (S=O symmetric stretching vibrations) and 720.99 cm^{-1} (S−C stretching vibrations).
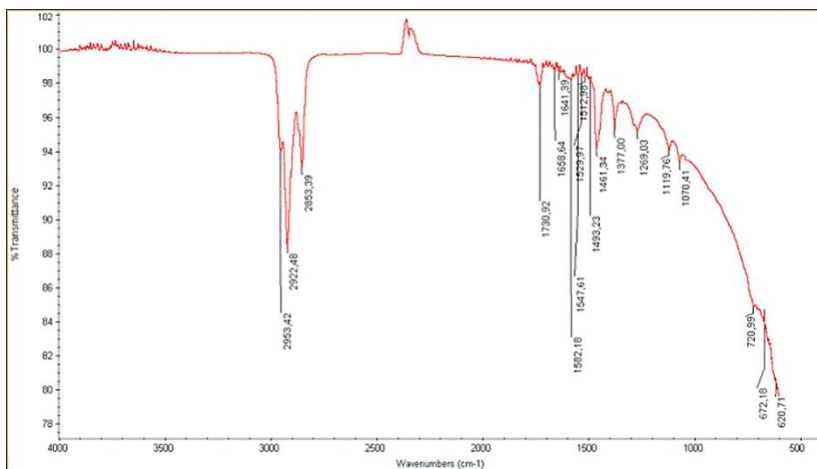
*Figure 1-5: **Linkage among the reactive groups analyzed by FT-IR.***

The DVS has an effect on the –OH groups of the HA chains and the favorable condition for this pH reaction is between 10 and 12. Furthermore, the linking between the aminic groups of Ch and the phosphoric groups of TPP and the –COOH groups of HA is not well promoted due to the strongly acid conditions of the chitosan-water phase. The acid state of the Ch phase is essential not only for the complete dissolution of the Ch in the CH_3COOH solution but also for the behavior of the Ch chains. In fact, at strongly acid condition, even if more groups are activated, they are set in a shape not favorable to the interaction with the TPP. On the contrary, at weak acid conditions, even if there are less free amine groups, they are set in a more favorable shape that allows them to interact with TPP through the $P_3O_{10}^{5-}$. To improve the stability of the polymeric NPs

58

different percentage of the two crosslinkers are tested. As previously shown 10%, 20% and 30% wt/v are tested for TPP while 8%, 16%, 24% v/v are tested for DVS. The results show not only a different stability of NPs in water but also a variation in their size. Increasing the TPP volume from 10% wt/v to 30% wt/v, the stability of the NPs is improved, and, at the same time, the size of the NPs decreases. The effect obtained in the case of DVS is completely different. In fact, an increasing of DVS percentage results in both an increasing of the size and the development of irregular shapes. It highlights the difficult of DVS to spread through the emulsion in the presence of a high concentrated oil phase. DVS concentration of 8% v/v and TPP concentration of 30% wt/v produce the stabilization of HyCoS NPs with a size in a range from 50nm to 200nm preserving also the coacervation process. It is important to note that the percentage of TPP is also increased from 20% to 30% wt/v in the HA phase (pH 10-11) to reach the final pH of the reaction (pH 5). In these conditions, the final values of pH is about 5, making stronger the linker between the two polymers. For the final reaction at pH value lower than 5, the crosslinking reaction of TPP between Ch and HA is not completed because the –COOH groups of HA are not fully activated while at pH higher than 5, available amine groups of Ch to the reaction are reduced.

1.4.4 Effect of the Temperature on the coacervation step

Furthermore, to minimize the time of the coacervation step, different gradients of temperature are tested (Figure 1- 6). The intent is to promote both the evaporation of the CH_3COOH and the chemical reaction of *inter* and *intra* chains. Several isothermal profiles are studied but the formation of nanoparticles is only observed at 35 °C, confirming that the coacervation step properly occurs even if the morphologies are not stable in water, probably due to an uncompleted chemical reaction among the compounds. Later, starting with the isothermal observations, we have studied the combination of an isothermal profile with a cooling step. In this experiment, the demixing is visible after 5,5 h of isothermic step at 35 °C followed by a ramp at 8°C/h from 35°C to 23°C, spending about 1.5 h to reach the final stable morphologies. It is important to note that, after the isothermal step, when the demixing visibly occurs, the cooling of the emulsion should be suddenly performed to avoid aggregation phenomena among the nanovectors.
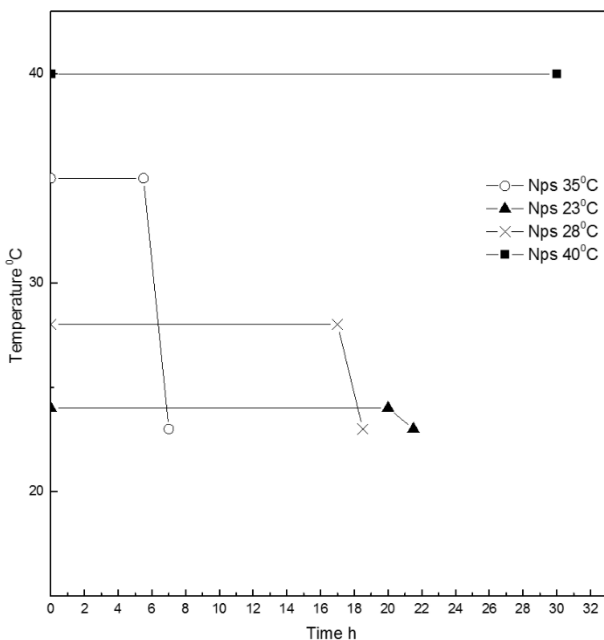
*Figure 1-6: **Profile of Demixing Reaction.** In the graph are shown the profiles of demixing of the coacervation at different gradients of temperature. Temperature enables a reduction of the process time from 24h to 6.5-7 h. Best results are obtained performing an Isothermal at 35 °C for 5.5h and a ramp from 35°C to 23°C for 1.5h. In details, after the isothermal step, the reaction of coacervation occurs, and a demixing of the prepared solution is observed. After the demixing phase, a variation of the temperature should be suddenly performed to avoid aggregation phenomena and the destruction of the nanovectors. Indeed, as soon as the demixing phase occurs, the produced nanoparticles are unstable and a further support of temperature needed to increase the stability of the system.*

Indeed, an additional cooling step is needed to increase the stability of the system. A reduction of the demixing time involves a decreasing in the evaporation time of the CH_3COOH, a faster coacervation reaction and an acceleration of the DVS reaction with the –OH groups on the polymer chain of HA. The use of temperature allows a reduction of the duration of time of coacervation from 24h to 6,5-7 h and it also allows a comparison in terms of swelling behavior with HyCoS NPs obtained at constant room Temperature, as reported in the next paragraphs. Images reported in Figure 1- 5 show nanoparticles obtained at the different demixing profile of the reaction at different temperatures. NPs obtained performing an Isothermal at 35 °C for 5.5h show the best stability and a defined core-shell morphology (Figure 1- 7 **-●-**). In Figure 1- 7E, a morphological characterization of core-shell nanoparticles obtained by TEM is shown. In details, several nanoparticles of 70 nm produced by our standard coacervation are reported while, in Figure 1- 7F, an enlargement is displayed highlighting the perfect core - shell architecture.
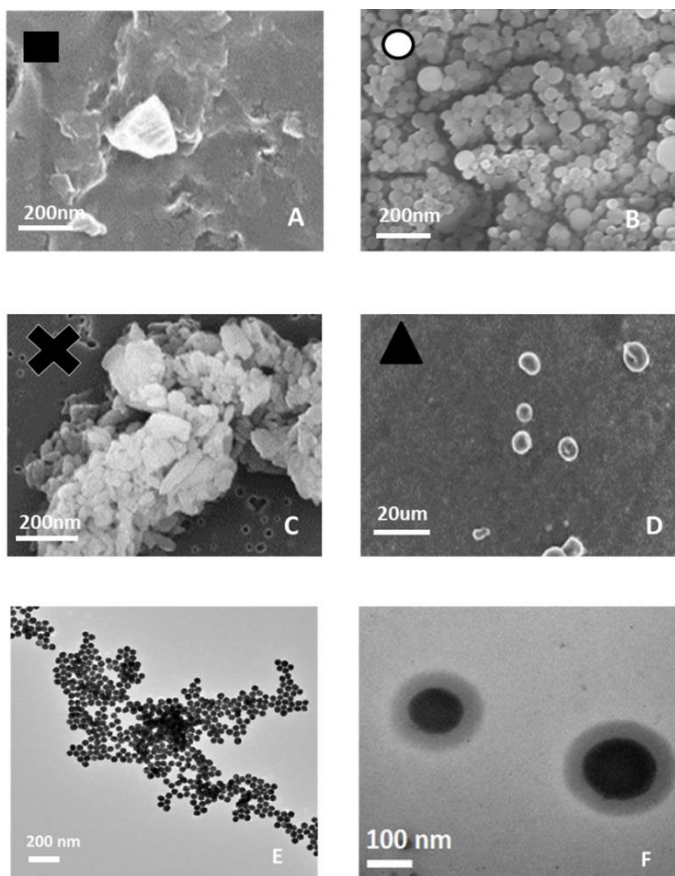
*Figure 1-7: **SEM images of nanoparticles produced by different calorimetric profile (A-D):** A (●)- NPs obtained performing an Isothermal at 35 °C for 5.5h; B (□)- Result obtained performing an Isothermal at 40 °C. No demixing is observed; C (X)- Result obtained performing an Isothermal at 28 °C until demixing (after 17h).D (▲)-Result obtained performing an Isothermal at 23 °C until demixing (after 20h). After that the demixing occurs, a ramp to 23°C for 1.5h is performed to complete the separation and to stabilize the morphologies. **Morphological characterization of nanoparticles by TEM (E-F):** Core-shell Gd-DTPA-NPs obtained without the use of the temperature profile collected in water. (E) NPs obtained at 0,1% wt/v HA, 1% wt/v Chitosan, 30% TPP wt/v, Gd-DTPA: Chitosan 1:1 and 8% v/v DVS and (F) Magnification of the previous image.*

1.4.5 pH-responsive behavior

Preliminary results on HyCoS NPs reports a peculiar yet interesting pH-sensitive behavior of the nanovectors. In details, for HyCoS NPs produced at room Temperature, at pH 4, they maintain their stability until the first hour, but after this time they dissolve completely. On the contrary, at pH 7 they preserve their stability at every different time (30 min, 1h, 2h, 3h, 6h, 8h, 12h, 24h). Nanoparticles obtained by using the cooling step do not seem to be pHsensitive and remain stable at any pH condition until 24 hr. Further details are reported in Figure 1- 8, showing images of the different behavior of the NPs by changing the pH conditions.
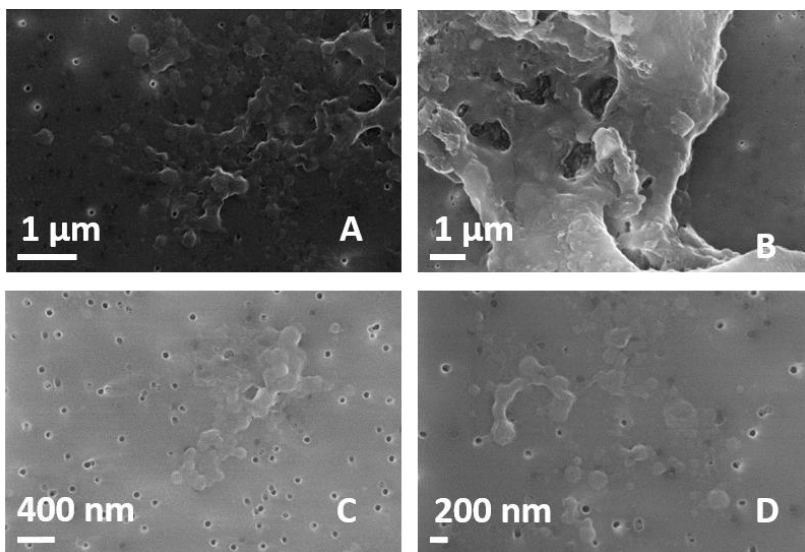
*Figure 1-8:**pH-Responsive NPs**:The behavior of the obtained NPs are tested at pH 4 and 7 at different time points: NPs maintained at pH 4 after 30 min (A); NPs maintained at pH 4 after 1h (B); NPs maintained at pH 7 after 30 min (C); NPs maintained at pH 7 after 24h (D).*

This characteristic pH triggering could provide significant advances in the use of the vector for the treatment of tumor pathologies. In fact, the tumor environment, besides to being devoid of oxygen, is also characterized by an acid pH by an impaired operation of the lymphatic system to drainage of fluids that instead tend to accumulate inside the interstitial space[38, 43-45]. First, the use of macromolecules and, later, nanocarriers is exploited to study the potential acidity of the tumor microenvironment to release any drugs encapsulated in the carriers directly in the tumor area to have a diffusion of the active agents within the tumor matrix and, therefore, performed a better diagnosis or therapy.

1.4.6   In vitro MRI

As already reported in the Materials and Method Section, ICP-MS is used to assess the concentration for Gd-DTPA loading within the HyCoS NPs. This data are also useful to evaluate the relaxometric properties of the nanovectors. Results clearly demonstrate that a relaxation rate T_1 of 1720 ms is achieved with 20 μM of Gd-loaded HyCoS while 100 μM of Gd-DTPA solution is required to reach similar T_1 (1724 ms) (Figure 1- 9). This effect of enhanced relaxivity potentially allows the administration of a reduced dosage of contrast medium keeping the same T_1 signal intensity. This peculiar behavior is probably ascribable to the combination between the hydrophobic nature of the Ch and the hydrophilic character of the HA tuning the water exchange with the coordination sites of the metal r. Intensity

on the ordinate axis is not reported because it represents a qualitative value related to the detector of the instrument and it is not considered in the MRI evaluation
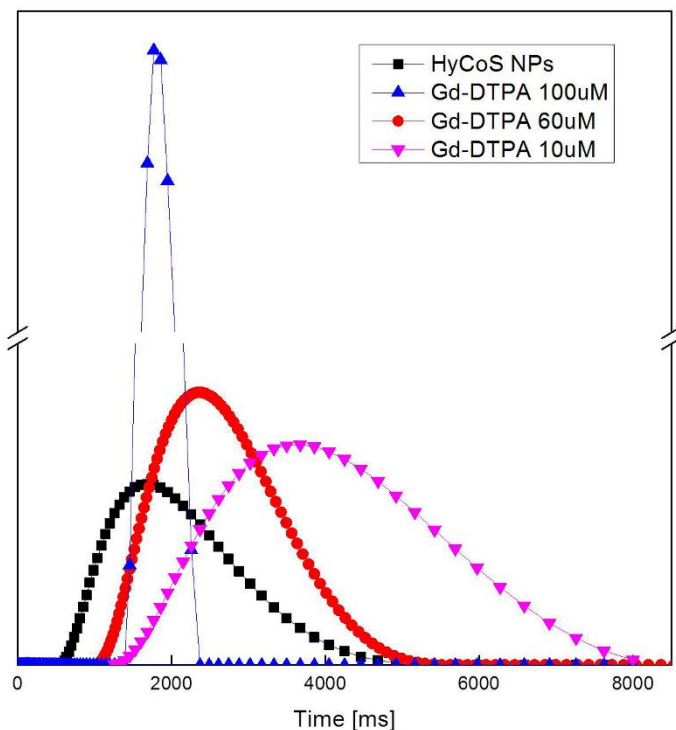
Figure 1-9: *In vitro MR:* Relaxation rate distributions of Gd-DTPA in solution at (-▼-)10µM; 60 µM (-●-), 100 µM (-▲-); and HyCoS NPs loaded with Gd-DTPA at (-■-)The results show an enhancement in r_1 of 6 times compared to the free Gd-DTPA. T_1.

1.4.7 Optical Imaging and bioconjugation

In Figure 1- 10, results related to the optical imaging of the nanoparticles observed under STED are reported. The first image (Figure 1- 10A) shows nanoparticles obtained by coacervation performed at 0,1% wt/v HA, 1% wt/v Ch, 30% TPP wt/v, Gd-DTPA: Ch 1:1, 8% v/v DVS. Cy5 ranging from 0.1 to 1 mg/mL (633 nm) are encapsulated into the NPs while, in Figure 1- 10B and C, the NPs are conjugated with FITC (488 nm). In (Figure 1- 10D), an intensity profile of the conjugated NPs of Figure 1- 10C is reported. Figure 1-10B and C reports the fluorescence due to the conjugation of the dye exclusively on the shell, highlighting the non-fluorescent core not involved in the reaction. We have also proved that nanoparticles are highly stable even after the reaction protocols and that are capable of preserving their cargo of Gd-DTPA as so their enhanced relaxometric properties. This is an important goal considering the relevance to candidate our product for the in vivo Integrated Multimodal Imaging.
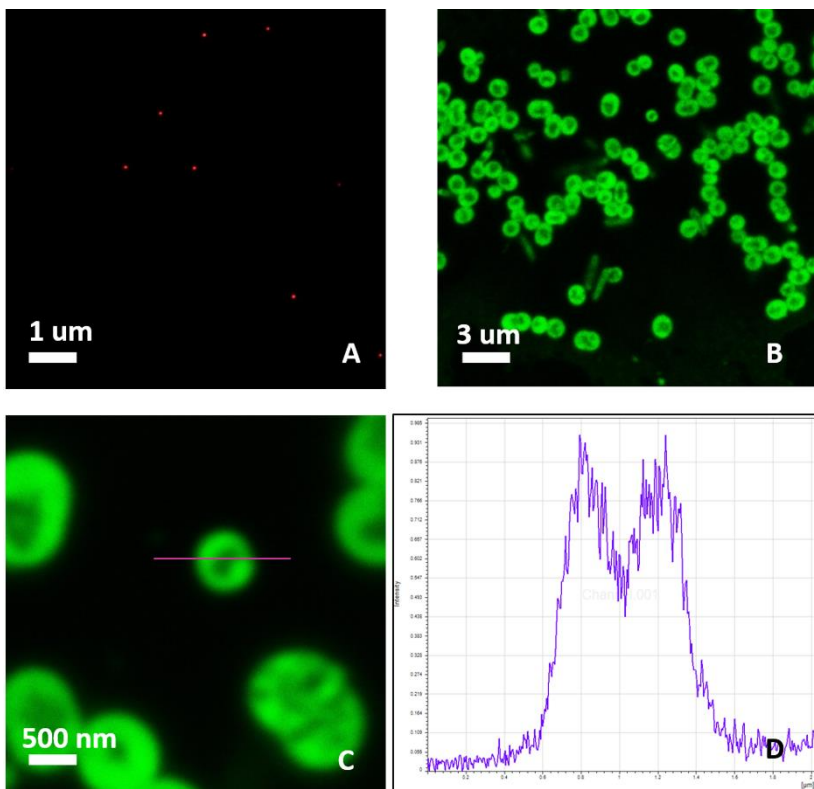
*Figure 1-10: **Optical Imaging of the nanoparticles observed under fluorescent microscope (Stimulated Emission Depletion STED):** NPs obtained at 0,1% wt/v HA, 1% wt/v Chitosan, 30% TPP wt/v, Gd-DTPA: Chitosan 1:1, 8% v/v DVS and Gd-DTPA: (A) Gd-DTPA and 100μl of Cy5 1mg/ml (633 nm) are encapsulated into the NPs;(B) The obtained nanoparticles are conjugated with FITC (488nm). The image shows the difference between the core and the shell structure;(C) Magnification of the image reported in figure (B); (D) intensity profile of fluorescent Nanoparticle in (B) calculated by the Region of Interest method (ROI).*

1.4.8   In vitro cytotoxicity

Typically, structural alterations of NPs in aqueous solutions, in cell-culture medium, might also affect and change the final results of the in vitro toxicological studies. Therefore, Cytotoxicity tests are

essential to preliminary asses the biocompatibility of the HyCoS NPs. Nasti et al.[46] suggest the cytotoxicity of the chitosan/TPP nanoparticle to be mostly dependent on their internalisation, which on its turn seems to be scarcely dependent on size and clearly dominated by surface composition/charge: indeed it is well known that positively charged nanoparticles are more quickly internalised than negatively charged ones and the HA-coating markedly reduces the nanoparticle toxicity. Results of chemical characterization studies show that the amount of covalently incorporated DVS into the structure of HA is largely controlled by the crosslinker concentration, thereby determining the mechanical stability and resistance against enzymatic degradation. Lai demonstrates good cytocompatibility of HA sheets treated with concentrations of DVS ranging from 0 to 50 mM.[47, 48 44] . For this study the toxicity of HyCoS NPs is tested using an WST-1 assay, which is based on the conversion of water-soluble tetrazolium salt (yellowish in color) to water insoluble formazan (purple color) by living cells. The WST assays have appeared to be advantageous over MTT because of its solubility in tissue culture medium and storage condition.

Scalar concentrations of HyCoS NPs are tested in a range between 200 ng/mL and 100 μg/mL. It is evidenced that the NPs showed no detectable cytotoxicity in vitro (Figure 1- 11).
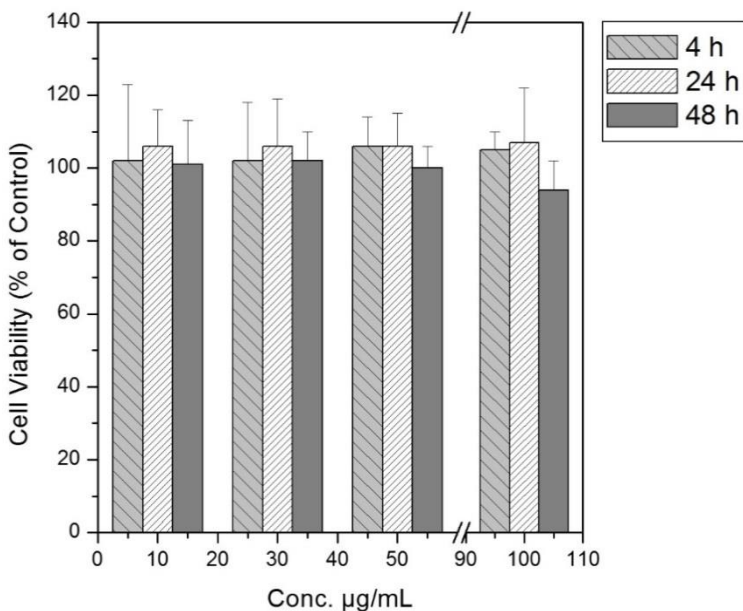
Figure 1-11: ***In vitro cytotoxicity:*** *A549 cell viability expressed as a percentage of the value obtained with a concentration of hyaluronic nanoparticles in a range between 10 μg/mL and 100 μg/mL for three different time intervals. The error bars represent the standard deviations calculated from three independent experiments.*

1.5   In vivo MRI analysis

Analysis is conducted on a PET/MRI 3 Tesla scanner to evaluate the % contrast enhancement (CE) of the images for a scanner used in a clinical practice. Two samples are studied: HyCoS NPs (Figure 1-12) and Gd-DTPA (Figure 1- 13).

In details, a multivariate analysis of variance for repeated measures (RM-MANOVA) is used to study the selected parameters of the treatment group with Gd-DTPA loaded HyCoS NPs and Gd-DTPA. No significant effect of the treatment group could be detected for renal medulla (0.96) and salivary glands (P=0.65) (Figure 1- 12). The urine %CE results significantly affected by the interaction of time over group (P=0.0008), with the HyCoS NPs having the highest %CE than Gd-DTPA treated mice (Figure 1- 13).

A significant difference between groups was detected for the renal cortex (P=0.03) and a significant effect of the interaction of time over the group (P=0.0007) is recorded, as well, with HyCoS NPs showing a higher and increasing %CE from 10 minutes to 1 hour (Figure 1- 12).
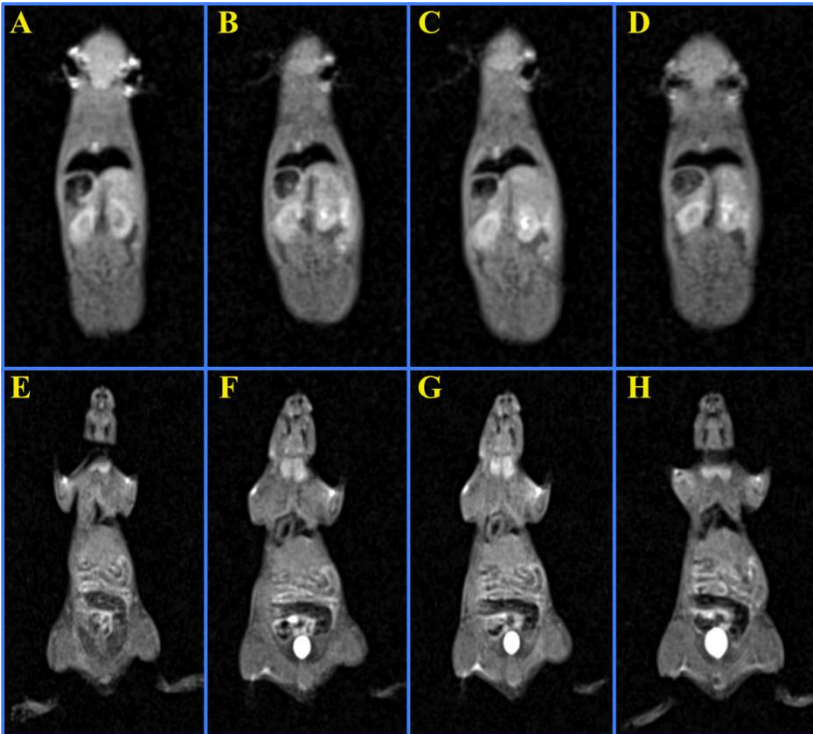
*Figure 1-12: **Dynamic MRI study:** coronal view of a mouse treated with HyCoS NPs. The slices selected include the kidneys (upper row) and the urinary bladder (lower row). Baseline acquisition (A, E) is followed by intravenous injection of the HyCoS NPs suspension, and the mice are scanned at 30 minutes (B, F), one hour (C, G) and 3 hours (D, H) post injection. The same window level (WL=320) and window width (WW=610) are used in all images.*
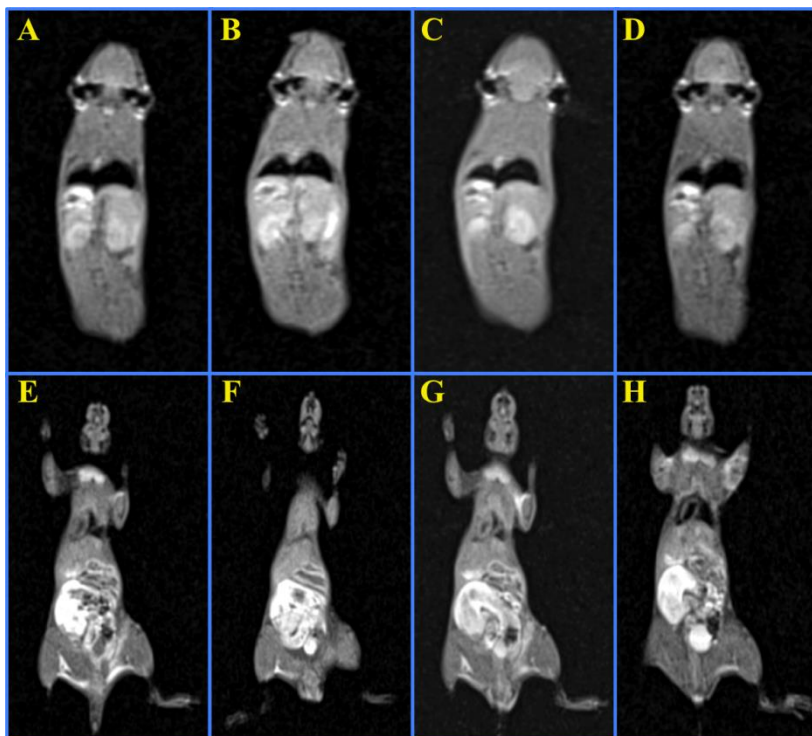
*Figure 1-13: **Dynamic MRI study**: Coronal view of a mouse treated with Gd-DTPA. The slices selected include the kidneys (upper row) and the urinary bladder (lower row). Baseline acquisition (A, E) is followed by intravenous injection of the Gd-DTPA solution, and the mice are scanned at 30 minutes (B, F), one hour (C, G) and 3 hours (D, H) post injection. The same window level (WL=320) and window width (WW=610) are used in all images.*

No accumulation of Gd-DTPA is shown from ICP-MS analysis following repeated administrations of HyCoS NPs (see Appendix par 5.2).

1.6 Discussion

The described process has led to the generation of NPs with a Chitosan core and an outer shell of HA. The innovations of process consist of a double crosslinking, by TPP and DVS, which allows controlling the stability and the degradation behavior of the two chosen polymers, and a heating/cooling step of the reaction to speed up the coacervation process and control the swelling behavior. TPP is considered as a small ion with a triple negative charge which is dissolved into the HA phase, able to link the hydrophobic core of Ch to the hydrophilic shell of HA. On the HA side, –OH(HA) and -COOH-(HA) can coexist in the tripolyphosphate solution at all pH values promoting the interchains reaction between the two polymers. Indeed, when the solution containing the HA and the TPP reaches the surface of the droplet template containing Ch and DVS, a coacervation layer has firstly formed on the surface of the Ch droplets, and anions and –COOH- (HA) reacts with caution. Simultaneously, the –OH groups of HA are linked by DVS, stabilizing the shell. (Figure 1- 14A), while TPP partially diffuses inside the template through the coacervation layer reaching the core and creating hydrogen bonding, linking the Ch core to the layer of the HA firmly (Figure 1- 14B). However, because HA has a molecular weight larger than the Ch, and Ch is a hydrophobic polymer, both HA and TPP cannot deeply penetrate the core, probably reaching only the surface of the Ch template. The above-

reported steps are here described for the first time and represent a significant advance in the understanding of the control of the interference due to the presence of Gd-DTPA in the crosslinking reaction and the coacervation process. A unique aspect of this system also lies in the double crosslinking promoting both an intrachain link among HA polymer chains and interchain links among Ch and HA able to control the loading of Gd-DTPA and its relaxometric properties. Furthermore, the TPP is added in HA coacervate phase while in literature is typically added to the chitosan phase. In details, phosphoric groups of TPP interact with the amine groups of Ch and with –COOH and –OH groups of HA, while sulfuric groups of DVS links –OH groups of HA. The reverse use of the two crosslinkers is fundamental to avoid the linkage between the chains of HA before the coacervation reaction occurs. In fact, the DVS is not able to interact with the Chitosan chains while TPP can link HA chains only partially [46]. The pH of the single polymeric solutions is deeply studied to control perfectly the reverse use of crosslinkers, t. Indeed, the pH of the Ch and HA phase are controlled to allow the activity of the crosslinkers only during the coacervation process and not during the preparation of the polymer solutions. The thermodynamics of the coacervation process can be explained in 3 steps by a ternary phase diagram at a specific heating/cooling step (Figure 1- 14C). First, referring to (Figure 1- 14C-I) after the preparation of the primary emulsion, the complete dissolution of the Ch in water is reached

through the utilization of the CH_3COOH. The working point is located outside of the miscibility gap that exists between water and Ch. In the second step (Figure 1- 14C-II), the Coacervation phase is added to the primary emulsion, promoting the dilution of the water phase: in this condition, the concentration of the CH_3COOH solution decreases below the saturation limit. At the same time, keeping constant the Temperature, CH_3COOH continues evaporating, inducing a further shifting of the working point in the miscibility gap, leading to the coacervation of HA on the chitosan template. In the last phase (Figure 1- 14C-III), a controlled cooling step is performed to increase the miscibility gap able to promote a faster supersaturation and the stability of the nanoparticle's architecture.
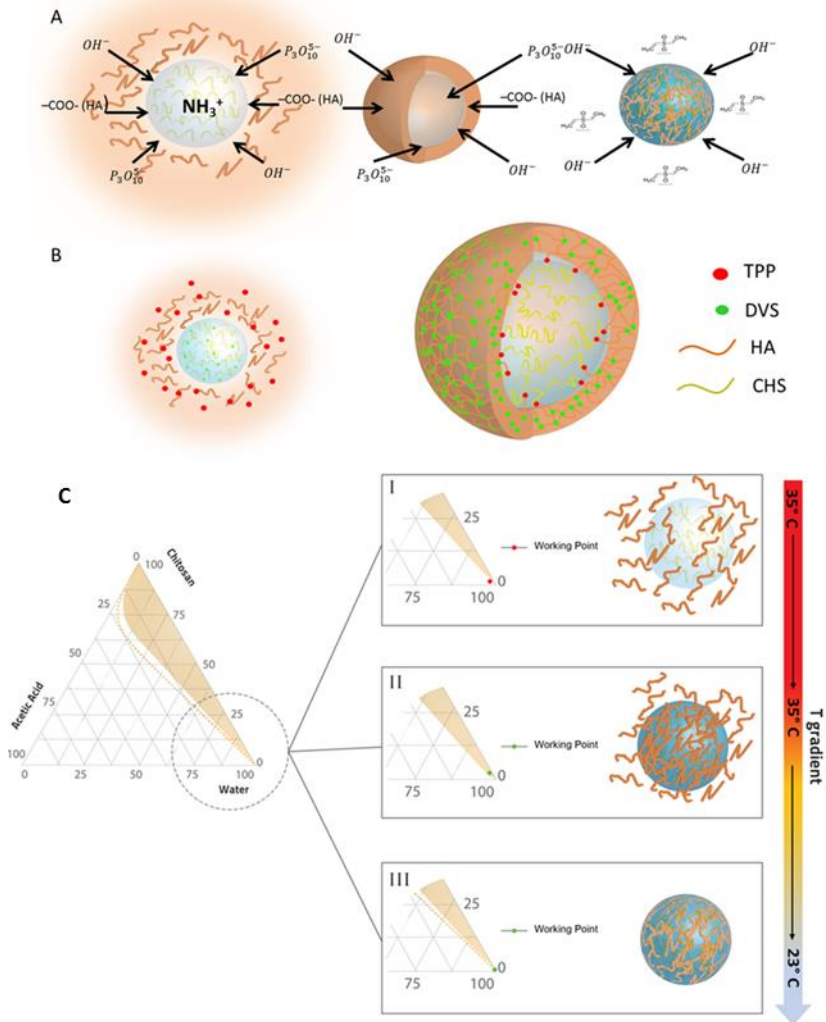
Figure 1-14: **Description of Double Crosslinking Reaction:** A) On the left the ionic interaction between TPP and Chitosan is described; later a crosslinking between Chitosan and HA is created through the TPP, on the right, in the last step the crosslinking between HA and DVS is obtained. B) Diffusion and formation of double-crosslinked core-shell. Schematical representation of the crosslinking at the

interface between the core and shell structure. C) **A schematical explanation of the process by the phase diagram change**: *I- After the preparation of the primary emulsion, disperse phase contains a homogeneous solution. Therefore, the working point represented in the phase diagram is located in the region of complete miscibility between water and Chitosan (brown area).*

II- Solution containing the coacervate is added to the primary emulsion, promoting the dilution of the disperse phase, promoting the supersaturation of the solute in the disperse phase and inducing the precipitation of the chitosan. At the same time keeping constant the temperature, Acetic acid continues to evaporate causing the further shifting of the working point into the miscibility gap. This last step will complete the formation of the chitosan template and the HA coacervation;

III- In the last phase, a controlled cooling step is performed to increase the miscibility gap able to promote a faster supersaturation and to enhance the stability of the nanoparticle's architecture.

The obtained HyCoS NPs result stable and retain their cargo even after the conjugation of fluorescent molecules, making them particularly suitable for multimodal imaging applications. Indeed, the process conditions allow the formation of the core-shell structure while the entrapment of Gd-DTPA is reached through the crosslinking reactions. The proposed approach describes the successful conditions to obtain the production of HyCoS Nanoparticles with improved MRI properties. This effect can be explained according to the Solomon Bloemberg model[49]. Indeed, in this theory, the metal complex can be schemed as having separate coordination spheres, the Inner Sphere (IS) and the Outer Sphere (OS) both described by the characteristic correlation times, such as the residence time of the coordinated water molecule (τM), which in turn determines the rate of the coordinated water molecule

exchanging with the bulk, and the rotational correlation time (τR), which is how quickly the contrast agent is tumbling in solution and the translational diffusional time (τD), which represent the diffusion of water molecules in the bulk near to the Gd complex[49, 50]. Because of these findings, we can assert that the improved MRI performances result from the double crosslinking able to control the entrapments of the Gd-DTPA at the Chitosan–HA interface and, therefore, to tune its physical characteristic parameters responsible for the relaxometric properties. The presented approach leverages the use of the coacervation kinetic and the crosslinking reaction, promoting the diffusion and exchange of the components at the interface HA-Ch and leading to a peculiar environment able to boost the relaxometric properties. The absence of these specific conditions will result in the absence of the MRI signal or even of the improved performances due to the hydrophobic nature of the Chitosan that would not allow the water exchange with the metal chelate limiting its relaxivity.

1.7   Conclusions

For diagnostic techniques, in particular MRI, the optimization of the size of particles obtained by complex coacervation is limited for the complexity of obtaining stable nanostructures in combination with a Gd-based contrast agents.

We obtained core-shell polymer NPs, which can be encapsulated with both Gd-DTPA and a Dye for Dual Imaging applications

through a complex coacervation that exploits an innovative double crosslinking to improve the stability of the nanostructure overcoming the interference of the coacervation process with the Gd-DTPA. Furthermore, the adjustment of the process parameters, the coacervation and chemical reaction kinetic promotes the interpolation of the hydrophobic core with the hydrophilic shell, controlling the water exchange and, consequently, the relaxation rate T_1, enhancing the MRI signal at reduced concentration compared to the relevant clinical CAs.

References

1.   Battaglia, L.; Gallarate, M.; Cavalli, R.; Trotta, M., Solid lipid nanoparticles produced through a coacervation method. *Journal of Microencapsulation* **2010,** *27* (1), 78-85.

2.   Irache, J. M.; Bergougnoux, L.; Ezpeleta, I.; Gueguen, J.; Orecchioni, A. M., Optimization and in vitro stability of legumin nanoparticles obtained by a coacervation method. *International Journal of Pharmaceutics* **1995,** *126* (1-2), 103-109.

3.   Nagpal, K.; Singh, S. K.; Mishra, D. N., Chitosan Nanoparticles: A Promising System in Novel Drug Delivery. *Chemical & Pharmaceutical Bulletin* **2010,** *58* (11), 1423-1430.

4.   Lee, D. W.; Yun, K.-S.; Ban, H.-S.; Choe, W.; Lee, S. K.; Lee, K. Y., Preparation and characterization of chitosan/polyguluronate nanoparticles for siRNA delivery. *Journal of Controlled Release* **2009,** *139* (2), 146-152.

5.   Arnedo, A.; Espuelas, S.; Irache, J. M., Albumin nanoparticles as carriers for a phosphodiester oligonucleotide. *International Journal of Pharmaceutics* **2002,** *244* (1-2), 59-72.

6.   Das, S.; Bellare, J. R.; Banerjee, R., Protein based nanoparticles as platforms for aspirin delivery for ophthalmologic applications. *Colloids and Surfaces B-Biointerfaces* **2012,** *93*, 161-168.

7.   Liu, F.; Liu, L.; Li, X.; Zhang, Q., Preparation of chitosan-hyaluronate double-walled microspheres by emulsification-coacervation method. *Journal of Materials Science-Materials in Medicine* **2007,** *18* (11), 2215-2224.

8.   Mao, H. Q.; Roy, K.; Troung-Le, V. L.; Janes, K. A.; Lin, K. Y.; Wang, Y.; August, J. T.; Leong, K. W., Chitosan-DNA nanoparticles as gene carriers: synthesis, characterization and transfection efficiency. *Journal of Controlled Release* **2001,** *70* (3), 399-421.

9.   Zhao, K.; Zhang, Y.; Zhang, X.; Li, W.; Shi, C.; Guo, C.; Dai, C.; Chen, Q.; Jin, Z.; Zhao, Y.; Cui, H.; Wang, Y., Preparation and efficacy of Newcastle disease virus DNA vaccine encapsulated in chitosan

nanoparticles. *International Journal of Nanomedicine* **2014,** *9*, 389-402.

10.   Jain, R. K.; Stylianopoulos, T., Delivering nanomedicine to solid tumors. *Nature Reviews Clinical Oncology* **2010,** *7* (11), 653-664.

11.   Huang, M.; Huang, Z. L.; Bilgen, M.; Berkland, C., Magnetic resonance imaging of contrast-enhanced polyelectrolyte complexes. *Nanomedicine-Nanotechnology Biology and Medicine* **2008,** *4* (1), 30-40.

12.   Saboktakin, M. R.; Tabatabaie, R.; Maharramov, A.; Ramazanov, M. A., Synthesis and characterization of superparamagnetic chitosan-dextran sulfate hydrogels as nano carriers for colon-specific drug delivery. *Carbohydrate Polymers* **2010,** *81* (2), 372-376.

13.   Key, J.; Leary, J. F., Nanoparticles for multimodal in vivo imaging in nanomedicine. *International Journal of Nanomedicine* **2014,** *9*, 711-726.

14.   Lee, D. E.; Koo, H.; Sun, I. C.; Ryu, J. H.; Kim, K.; Kwon, I. C., Multifunctional nanoparticles for multimodal imaging and theragnosis. *Chemical Society Reviews* **2012,** *41* (7), 2656-2672.

15.   Kim, J.; Piao, Y.; Hyeon, T., Multifunctional nanostructured materials for multimodal imaging, and simultaneous imaging and therapy. *Chemical Society Reviews* **2009,** *38* (2), 372-390.

16.   Vizirianakis, I. S., Nanomedicine and personalized medicine toward the application of pharmacotyping in clinical practice to improve drug-delivery outcomes'. *Nanomedicine-Nanotechnology Biology and Medicine* **2011,** *7* (1), 11-17.

17.   Kircher, M. F.; Mahmood, U.; King, R. S.; Weissleder, R.; Josephson, L., A multimodal nanoparticle for preoperative magnetic resonance imaging and intraoperative optical brain tumor delineation. *Cancer Research* **2003,** *63* (23), 8122-8125.

18.   Mora-Huertas, C. E.; Fessi, H.; Elaissari, A., Polymer-based nanocapsules for drug delivery. *International Journal of Pharmaceutics* **2010,** *385* (1-2), 113-142.

19.   Cai, W.; Hsu, A. R.; Li, Z.-B.; Chen, X., Are quantum dots ready for in vivo imaging in human subjects? *Nanoscale Research Letters* **2007,** *2* (6), 265-281.

20.   Jin, X. Y.; Fang, F.; Liu, J. H.; Jiang, C. H.; Han, X. L.; Song, Z. K.; Chen, J. X.; Sun, G. Y.; Lei, H.; Lu, L. H., An ultrasmall and metabolizable PEGylated NaGdF4:Dy nanoprobe for high-performance T-1/T-2-weighted MR and CT multimodal imaging. *Nanoscale* **2015,** *7* (38), 15680-15688.

21.   Osseni, S. A.; Lechevallier, S.; Verelst, M.; Perriat, P.; Dexpert-Ghys, J.; Neumeyer, D.; Garcia, R.; Mayer, F.; Djanashvili, K.; Peters, J. A.; Magdeleine, E.; Gros-Dagnac, H.; Celsis, P.; Mauricot, R., Gadolinium oxysulfide nanoparticles as multimodal imaging agents for T-2-weighted MR, X-ray tomography and photoluminescence. *Nanoscale* **2014,** *6* (1), 555-564.

22.   Wang, F.; Banerjee, D.; Liu, Y. S.; Chen, X. Y.; Liu, X. G., Upconversion nanoparticles in biological labeling, imaging, and therapy. *Analyst* **2010,** *135* (8), 1839-1854.

23.   Liu, Z.; Liu, X.; Yuan, Q. H.; Dong, K.; Jiang, L. Y.; Li, Z. Q.; Ren, J. S.; Qu, X. G., Hybrid mesoporous gadolinium oxide nanorods: a platform for multimodal imaging and enhanced insoluble anticancer drug delivery with low systemic toxicity. *Journal of Materials Chemistry* **2012,** *22* (30), 14982-14990.

24.   Utech, S.; Boccaccini, A. R., A review of hydrogel-based composites for biomedical applications: enhancement of hydrogel properties by addition of rigid inorganic fillers. *Journal of Materials Science* **2016,** *51* (1), 271-310.

25.   Xie, J.; Lee, S.; Chen, X. Y., Nanoparticle-based theranostic agents. *Advanced Drug Delivery Reviews* **2010,** *62* (11), 1064-1079.

26.   Pardridge, W. M., Drug transport across the blood-brain barrier. *Journal of Cerebral Blood Flow and Metabolism* **2012,** *32* (11), 1959-1972.

27.   Biasutti, M.; Dufour, N.; Ferroud, C.; Dab, W.; Temime, L., Cost-Effectiveness of Magnetic Resonance Imaging with a New

Contrast Agent for the Early Diagnosis of Alzheimer's Disease. *Plos One* **2012,** *7* (4).

28.   Janib, S. M.; Moses, A. S.; MacKay, J. A., Imaging and drug delivery using theranostic nanoparticles. *Advanced Drug Delivery Reviews* **2010,** *62* (11), 1052-1063.

29.   Jun, Y.-W.; Lee, J.-H.; Cheon, J., Chemical design of nanoparticle probes for high-performance magnetic resonance imaging. *Angewandte Chemie-International Edition* **2008,** *47* (28), 5122-5135.

30.   Zhang, L.; Liu, R. Q.; Peng, H.; Li, P. H.; Xu, Z. S.; Whittaker, A. K., The evolution of gadolinium based contrast agents: from single-modality to multi-modality. *Nanoscale* **2016,** *8* (20), 10491-10510.

31.   Xie, J.; Chen, K.; Huang, J.; Lee, S.; Wang, J.; Gao, J.; Li, X.; Chen, X., PET/NIRF/MRI triple functional iron oxide nanoparticles. *Biomaterials* **2010,** *31* (11), 3016-3022.

32.   Chen, K.; Xie, J.; Xu, H.; Behera, D.; Michalski, M. H.; Biswal, S.; Wang, A.; Chen, X., Triblock copolymer coated iron oxide nanoparticle conjugate for tumor integrin targeting. *Biomaterials* **2009,** *30* (36), 6912-6919.

33.   Nam, T.; Park, S.; Lee, S.-Y.; Park, K.; Choi, K.; Song, I. C.; Han, M. H.; Leary, J. J.; Yuk, S. A.; Kwon, I. C.; Kim, K.; Jeong, S. Y., Tumor Targeting Chitosan Nanoparticles for Dual-Modality Optical/MR Cancer Imaging. *Bioconjugate Chemistry* **2010,** *21* (4), 578-582.

34.   Tan, Y. F.; Chandrasekharan, P.; Maity, D.; Yong, C. X.; Chuang, K.-H.; Zhao, Y.; Wang, S.; Ding, J.; Feng, S.-S., Multimodal tumor imaging by iron oxides and quantum dots formulated in poly (lactic acid)-D-alpha-tocopheryl polyethylene glycol 1000 succinate nanoparticles. *Biomaterials* **2011,** *32* (11), 2969-2978.

35.   Huang, Y.; Hu, L.; Zhang, T.; Zhong, H.; Zhou, J.; Liu, Z.; Wang, H.; Guo, Z.; Chen, Q., Mn-3 Co(CN)(6) (2)@SiO2 Core-shell Nanocubes: Novel bimodal contrast agents for MRI and optical imaging. *Scientific Reports* **2013,** *3*.

36.   Tian, Q.; Hu, J.; Zhu, Y.; Zou, R.; Chen, Z.; Yang, S.; Li, R.; Su, Q.; Han, Y.; Liu, X., Sub-10 nm Fe3O4@Cu2-xS Core-Shell Nanoparticles for Dual-Modal Imaging and Photothermal Therapy. *Journal of the American Chemical Society* **2013,** *135* (23), 8571-8577.

37.   McCann, C. M.; Waterman, P.; Figueiredo, J. L.; Aikawa, E.; Weissleder, R.; Chen, J. W., Combined magnetic resonance and fluorescence imaging of the living mouse brain reveals glioma response to chemotherapy. *Neuroimage* **2009,** *45* (2), 360-369.

38.   Stylianopoulos, T.; Jain, R. K., Design considerations for nanotherapeutics in oncology. *Nanomedicine : nanotechnology, biology, and medicine* **2015,** *11* (8), 1893-907.

39.   Ankrum, J. A.; Miranda, O. R.; Ng, K. S.; Sarkar, D.; Xu, C.; Karp, J. M., Engineering cells with intracellular agent-loaded microparticles to control cell phenotype. *Nature Protocols* **2014,** *9* (2), 233-245.

40.   Provencher, S. W., CONTIN: a general purpose constrained regularization program for inverting noisy linear algebraic and integral equations. *Computer Physics Communications* **1982,** *27* (3), 229-242.

41.   Schante, C. E.; Zuber, G.; Herlin, C.; Vandamme, T. F., Chemical modifications of hyaluronic acid for the synthesis of derivatives for a broad range of biomedical applications. *Carbohydrate Polymers* **2011,** *85* (3), 469-489.

42.   Collins, M. N.; Birkinshaw, C., Investigation of the swelling behavior of crosslinked hyaluronic acid films and hydrogels produced using homogeneous reactions. *Journal of Applied Polymer Science* **2008,** *109* (2), 923-931.

43.   Jain, R. K., DETERMINANTS OF TUMOR BLOOD-FLOW - A REVIEW. *Cancer Research* **1988,** *48* (10), 2641-2658.

44.   Jain, R. K., TRANSPORT OF MOLECULES ACROSS TUMOR VASCULATURE. *Cancer and Metastasis Reviews* **1987,** *6* (4), 559-593.

45.   Nguyen, K. T.; Zhao, Y. L., Engineered Hybrid Nanoparticles for On-Demand Diagnostics and Therapeutics. *Accounts of Chemical Research* **2015,** *48* (12), 3016-3025.

46.   Nasti, A.; Zaki, N. M.; de Leonardis, P.; Ungphaiboon, S.; Sansongsak, P.; Rimoli, M. G.; Tirelli, N., Chitosan/TPP and Chitosan/TPP-hyaluronic Acid Nanoparticles: Systematic Optimisation of the Preparative Process and Preliminary Biological Evaluation. *Pharmaceutical Research* **2009,** *26* (8), 1918-1930.

47.   Soppimath, K. S.; Tan, D. C. W.; Yang, Y. Y., pH-triggered thermally responsive polymer core-shell nanoparticles for drug delivery. *Advanced Materials* **2005,** *17* (3), 318-+.

48.   Papadimitriou, S. A.; Achilias, D. S.; Bikiaris, D. N., Chitosan-g-PEG nanoparticles ionically crosslinked with poly(glutamic acid) and tripolyphosphate as protein delivery systems. *International Journal of Pharmaceutics* **2012,** *430* (1-2), 318-327.

49.   Caravan, P., Strategies for increasing the sensitivity of gadolinium based MRI contrast agents. *Chemical Society Reviews* **2006,** *35* (6), 512-523.

50.   Ponsiglione, A. M.; Russo, M.; Netti, P. A.; Torino, E., Impact of biopolymer matrices on relaxometric properties of contrast agents. *Interface Focus* **2016,** *20160061*.

CHAPTER 2

2 Functionalized HyCoS NPs for in vivo optical imaging applications: the case study of a B-cell lymphoma.
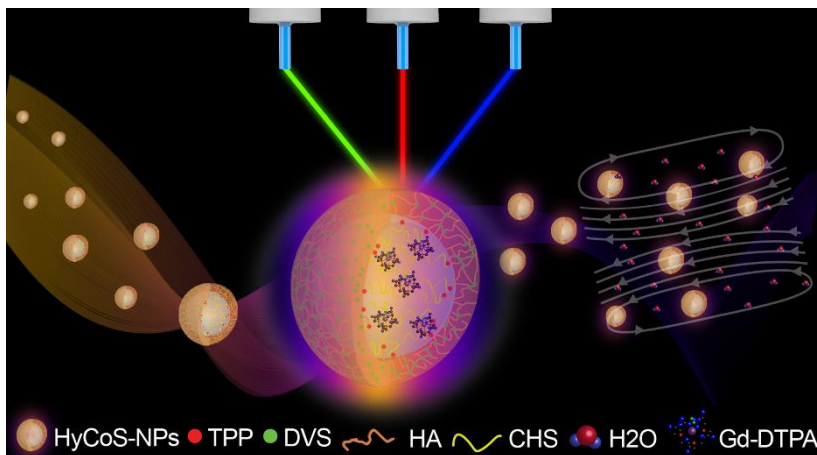
*Figure 2-1: **Graphical representation:** Multimodal designed nanovector for MRI and optical imaging applications.*

2.1 Introduction

Tumors are abnormal clusters of cells formed by alteration of genes which induce a single cell to proliferate, giving rise to a large number of elements, all equal to the cell that has undergone the "tumor transformation". Due to this transformation, the cells and their progeny are more or less completely released from the normal mechanisms of control of the body[1]. Cancer is due to many different causes with include environmental influences, ageing, life style and predisposition and in an attempt to predict the cynical behavior of a tumor and to establish useful criteria to treatment, tumors' classification is based on the degree of cytologic and histologic differentiation, clinical stage or protocols that describe the extent of the tumors' diffusion[2]. Tumors of low degree are well differentiated, while those of high degree tend to be anaplastic. The degree of cytologic and histologic differentiation, which are necessarily subjective and at best semi-quantitative, based on the degree of anaplasia and the number of proliferating cells. The presence of different features as shape or regularity of cells identifies a tumor as well differentiated or the opposite, the cells of poorly differentiated tumors show a very low similarity with their normal counterpart. Rapid or abnormal growth is made evident by the high numbers of mitoses, atypical mitoses, nuclear pleomorphism and giant cell tumor. Most of the schemes classify tumors in 3 or 4 degrees of malignancy growing. The general correlation between the cytological

degree and the biological behavior of a tumor is not immutable. The choice of a surgical conduct or selection of treatment modality is influenced more by the stage of a tumor than by its grade cytology. The criteria generally used to classify a tumor include the size of the tumor, the extent of local growth, if it contains all internal body or even out of it, the presence of lymph node metastases and the presence of distant metastases. These criteria have been codified in the international system of TNM staging of tumors, where T indicates the size of the primary tumor, N indicates metastasis to regional lymph nodes and the presence and M extension of distant metastases.

The tumor cells essentially behave in two ways, giving rise said benign tumors and other malignant said and liquid[a] and solid[b] tumor[3]. Differently from malignant tumors, benign tumors are composed of mature or nearly mature cells, which possess the features normally present in the cell type belonging to the first transformed cell. Furthermore, benign tumors appear to be localized, having reached a

---

[a] Leukemias ("liquid cancers" or "blood cancers") are cancers of the bone marrow (the site of blood cell production). The disease is often associated with the overproduction of immature white blood cells. These immature white blood cells do not perform as well as they should, therefore the patient is often prone to infection. Leukemia also affects red blood cells and can cause poor blood clotting and fatigue due to anemia.
[b] An abnormal mass of tissue that usually does not contain cysts or liquid areas. Solid tumors may be benign (not cancer), or malignant (cancer). Examples of solid tumors are sarcomas, carcinomas, and lymphomas.

certain size, they cease to grow, and from that time remain stationary or in some cases smaller. Differently malignant tumors generally derived from immature cells, the tissues that hold in reserve to replace wounds or lost items for injuries or diseases. In normal conditions, these immature cells before multiplying and completing their maturation, acquire organelles and properties, which allow them to the effective performance of the duties for which they are programmed. When neoplastic transformation affects immature daughter cells sometimes progressing towards a certain degree of maturity, are still immature at times, to the point that you do not always understand what type of cell they belong. In each case, the elements that have undergone the transformation tumor multiply with great rapidity without limits, and are completely subtracted in each adjustment. The tumor may expand as much as its mass or crevice available; creeps offshoots that fit into nearby organs deforming the structure and impair its function. In relation to the ways of propagation easier, metastases are found mainly in lymph nodes district but are also frequent distant metastases, which are derived from cells transported by the blood stream[4]. The malignant tissues are made up of cells in continuous and unlimited proliferation, survival and expansion which has only one limit: the contribution of nutrition. The presence of tumor cells in the connective adjacent tissue induces the formation of a structure of support in the context of which develops of newly formed blood vessels[5]. All these

characteristics aim to generate a specific representative microenvironment. The tumor microenvironment is completely different from that of healthy tissue starting from the blood vessels. Blood vessels deliver oxygen and nutrients to every part of the body, but also nourish diseases such as cancer[5]. The tumor vasculature is highly heterogeneous and does not conform to the standards of normal blood vessels[6]. Macroscopically it is possible to define two categories of tumor blood vessels: a peripheral one and a central one[5]. Microscopically the tumor vessels can be classified into nine categories: arteries and arterioles; non-fenestrated, fenestrated, and discontinuous capillaries; blood channels; capillary sprouts; postcapillary venules; venules and veins; and arteriovenous anastomoses[7]. The large and small arteries and arterioles are invested from smooth muscle cells and are capable of vasomotor adjustments. The terminal arterioles, the next branching order of arterial vessels, are invested proximally in vascular smooth muscle that gradually decreases until a single smooth muscle cell, spirally wrapped, marks the end of the muscular investment[6]. This final smooth muscle cell is referred to as the precapillary sphincter and serves as the final control site for blood flow into the capillary bed. Capillaries are vessels made of endothelial cells surrounded by a basement membrane. These vessels are devoid of smooth muscle cells and hence are incapable of active vasoconstriction/vasodilation[6]. They are ideal for the exchange of material between the blood and tissues.

Capillaries can be divided into three categories based on their wall structure: non-fenestrated (continuous); fenestrated; discontinuous[7]. Non-fenestrated capillaries are the most common type and are located in the skin, connective tissue, skeletal and cardiac muscle, alveolar capillaries of the lung, and the brain. In fenestrated capillaries, there are fenestrae or transendothelial circular openings of about 400-800 Å between the lumen and interstitium across the endothelial cells. These fenestrae may be open or covered by a thin 60-80 Å layered diaphragm similar to the diaphragm of vesicles. Discontinuous capillaries have large diameters and wide opening between endothelial cells[7]. The production process of these blood vessels following the creation of the tumor mass is called angiogenesis[8]. The angiogenesis process is a complex process of combination between factors which promote the formation of new blood vessels and those that inhibit this process. The loss of a correct balance between these elements causes the increasing of the blood vessel formation to the development of tumor diseases[6]. Between the different factors which are involved in the angiogenesis process there is the vascular endothelial growth factor (VEGF)[c] which can induce the division of cultured endothelial cells thus indicating a direct

---

[c] Vascular endothelial growth factor (VEGF) is a chemical signal produced by cells that stimulates the growth of new blood vessels. It is part of the system that restores the oxygen supply to tissues when blood circulation is inadequate. VEGF's normal function is to create new blood vessels during embryonic development, new blood vessels after injury, and new vessels (collateral circulation) to bypass blocked vessels.

action on these cells[9]. These new formed vessels supply the tumor of blood, in practice, oxygen and nutrients[10]. Very often, however, and especially in more aggressive tumors, in rapid growth, supplies are insufficient; it is not uncommon that large portions of the tumor remain suddenly without nutrient intakes and should be met necrosis[11]. This explains why the expansion of tumors is often irregular and subject to unpredictable regressions[12]. What it is going to determine is an environment made up of blood vessels resulting in conditions of oxygen deficiency, hypoxia, and high acidity[13,14]. The hypoxia causes changes in genetic activity that promotes the migration of endothelial cells through healthy tissue. Radiation and chemotherapy treatments used in the treatment that requires oxygen to kill tumor cells fail to do their job, immune cells that should attack the cancer cells cannot perform their function because of the acidity of the environment and the lack of oxygen[6]. With the passage of time the necrotic part developing in the center of the tumor increases in size due to the increasing difficulty on the part of the blood vessels to provide the necessary nutrients and oxygen, while the outlying areas increase thanks to the acquisition of the same from the outside[13]. So, the vascular-extravascular exchange is a key element in the study of tumors[15]. In normal tissues, substances that cross the blood vessels do not accumulate in the interstitial tissues but they are drained by the lymphatic system differently from what happens in the tumor tissues[16]. The tumor microenvironment [17] is characterized by the

presence of different kinds of cell, including endothelial cells, pericytes, smooth muscle cells, fibroblast, carcinoma-associated fibroblasts, myofibroblasts, neutrophils, carcinoma associated-fibroblasts, eosinophils, basophils, mast cells, T and B lymphocytes, natural killer cells and antigen presenting cells APC, such as macrophages and antigen presenting cells[4]. Because of poor and abnormal vascular development, the majority of solid tumors presents median O_2 levels lower than those of the tissue of origin[4]. In addition, the hypoxic areas are characterized by low levels of glucose, acid pH and cause an increase in the expression of proteins related to angiogenesis[14]. The hypoxic microenvironment present in solid tumors influences not only cancer cells, but also non-neoplastic stromal cells, such as macrophages and fibroblasts and gives the tumor a greater aggressiveness and an increased metastatic potential[13]. This effect seems to be due to overexpression in a hypoxic environment, gene products that can promote tumor progression allowing the cells to adapt to the deprivation of food and to escape from a hostile environment. Furthermore, the hypoxic tumor cells provide a microenvironment that facilitates the radio - and chemo – resistance, in fact, the hypoxic tumor cells are significantly more resistant than normal oxygenated cells to ionizing radiation[18]. It is due because, while in normoxic conditions the oxygen reacts with the radicals produced in the DNA damaged from ionizing radiation staring permanently, in the absence of oxygen

most of these radicals is converted into a form not damaged, following the donation of hydrogen by non-protein sulfhydryl groups present in the cell. The lack of oxygen also significantly affects the response of tumor cells to *hyperthermia*. Based on the results of experiments in preclinical models have proposed a classification of anticancer drugs into different groups, depending on their susceptibility to O_2 [4]. There is plenty of research showing the link between acidic pH and cancer. Cancer thrives in an acidic environment and does not survive in a normal, more alkaline environment. Cancer cells make body even more acidic as they produce lactic acid. , in fact acidic water holds very little oxygen, so the more acidic your cells are, the less oxygenated they will be. Diffusing into the normal tissue, the acid causes normal cell death which in turn allows the tumor to expand[14]. The possibility to have an early and effective diagnosis of a tumor disease can increase even chances of survival that ensuring patients receive the most appropriate treatments[19]. As it is known, the treatment of cancer, in general, more likely to succeed in the early stages.

Contrast media play an important role in allowing the display of a target with most conventional techniques (magnetic resonance imaging (MRI), computed tomography, optical and x-ray imaging (x-ray CT)[20]. However, most of the current contrast agents show instability in vivo, poor targeting, and an uncontrolled release. In addition, current in vivo imaging techniques are not always capable

of detecting tumors in the early stages because of their limited size. Molecular Imaging (MI) is a technique that controls the changes in vivo at the molecular level in order to detect diseases at an early stage. In this way, doctors are able to come up with a personalized therapy for the patient by examining closely the region of the body. For this purpose, vectors are used for the transport of polymer fluorescent agents because their physical-chemical properties offer several advantages including facilitation of the process endocytosis and cellular interaction; passing large amounts of the drug; ability of functionalization of surfaces with a variety of molecular signals and receptors for targeting, and theranostics capabilities to allow both the detection and treatment of specific diseases. As described in the Main Introduction of this thesis work, nanotechnology may help in the transfer of drugs or tracers across the biological barriers to reach the target organs in order to treat and/or detect diseases[21,22]. In this chapter, the multimodal designed vector (HyCoS) presented in chapter one is encapsulated with a dye ATTO680 during the coacervation process and consequently functionalized with different kinds of selected peptides in order to detect B-cell lymphoma[23] using Fluorescence Microscopy Tomography (FMT). The pA20-36, pA20-6 and pA20-S are the selected and tested peptides[24]. In 2010, Palmieri et al. demonstrated that pA20-36 binds specifically to the complementarity-determining regions of the A20 B-cell receptor (BCR) and enabling in vivo detection of neoplastic cells (B-cells

lymphoma) and at the same time the inhibition of tumor growth in vivo[25]. The B-cell lymphomas[26] is a solid tumor and it is a typical lymphoma affecting by B cells. They usually develop more frequently in older adults and in immunocompromised individuals. Lymphomas require intensive treatments and the patients are kept under control with long-term survival of many years. There are different kinds of lymphomas involving B cells as diffuse large B-cell lymphoma, follicular lymphoma, marginal zone B-cell lymphoma (MZL) or Mucosa-Associated Tissue lymphoma (MALT), small lymphocytic lymphoma (leukemia) and Mantle cell lymphoma (MCL) while other rare forms are much less common.

NPs structure intended for the carriage of medications is complicated because the effectiveness in achieving the target site depends on many factors. Physico-chemical properties as structure, density, type of ligand and the chemistry of conjugation contribute strongly to the effectiveness of the system. The effectiveness of the strategy of active targeting in vitro and especially in vivo is also influenced by other factors such as the route of administration and non-specific protein binding as they pass through the bloodstream. The specificity of targeting will be determined by the biodistribution of ligand-Functionalized and as the complex NPs interacts with molecules off-target and healthy cells. The aim of this work has been to test the different peptides combined with the produced HyCoS NPs to study their behavior when they are conjugated to our complex nanocarrier

to improve the detection power of the peptide thanks to the presence of a specific dye which is detectable by FMT without any interference with biological tissue. In addition, the MRI properties of the nanoparticles have been preserved and combined with these optical properties in order to perform perspectively the multimodal imaging- The obtained NPs are functionalized with peptides using two types of reactions: a direct one and an indirect one. The protocols of the reactions are designed to maintain the stability of the nanovectors and to reach the right concentration for in vivo applications. The resulted probes are administrated to C57 bulb mice engrafted with A20 lymphoma using the A20 and 5T33MM cell line used by Palmieri et al. for their work[25]. In this case, the NPs are used for both diagnostic and therapeutically purposes. In this work, peptides on nanoparticles surface may address the nanoparticles to the tumor area [27]. In fact, active targeting, also called ligand-mediated targeting[28], uses the affinity of the ligand, exposed on the surface of NPs, to molecules or overexpressed receptors in diseased organs, tissues, cells or subcellular domains[8]. The design of such systems is given then to increase the interactions between NPs and cells that the internalization of ligand optimized without altering the general biodistribution[26].

Such systems should be capable of selectively attack cancer cells, thanks to the modification of the surface with specific ligands for the tumor[29], sparing the healthy tissue toxic effects of medication that are

observed with conventional therapies. The ability to target specific cells could improve the effectiveness of reducing the toxicity[30]. Selective treatment based on nanoparticles would represent a significant improvement over the standard drug therapy, in which the drug can be internalized by virtually any cell with possible damage to normal tissues[31].

2.2 Materials

Materials used for Nanoparticle preparation: Chitosan (Ch) low molecular weight; Sodium Tripolyphosphate (TPP) 367.86 g/mol; Glacial Acetic Acid molecular weight 60.05; Ethanol (EtOH) molecular weight 46.07; Gd-DTPA molecular weight 547.57; Mineral Oil 0.84 g/mL at 25°C (lit.); Span80 molecular weight 274.43; 1.005 g/mL at 20 °C (lit.); ATTO680 652 g/mol are purchased by Sigma-Aldrich while Hyaluronic Acid (HA) 850 kDa parenteral grade is by Hyasis. MilliQ water is used for all experiments.

Reactants used for conjugation of peptide to Nanoparticles: REDC (1-ethyl-3-(3-dimethylaminopropyl) carbodiimide hydrochloride), NHS (N-hydroxysuccinimide) and Streptavidin are purchased by Sigma-Aldrich. Peptides A20-6S (ICSPVSCSK; MW: 1067 Da), A20-36 ((EYVNCDNLVGNCVIRG, MW:1922 Da) and A20-6 are produced by Caslo.

Polystyrene NPs by Thermo are used for PEG-FITC quantification.

Cell lines are the A20 and 5T33MM cell lines are used to induce B-cell lymphoma in C57 bulb mice model[9].

VivoTag® 750-S (Perkin Elmer) and Dimethyl sulfoxide (DMSO) by Sigma-Aldrich are used for the preparation of labeled peptide.

2.3 Methods

2.3.1 Nanoparticles (NPs) preparation

The Nanoparticles (NPs) are produced by an Emulsion-Coacervation method starting from a w/o emulsion (Chapter 1 paragraph 1.3). The starting emulsion is composed of a water phase of 1% wt/v Ch, 1:1 Gd-DTPA, 1mg ATTO680 in a solution of Acetic Acid at pH4.5, while the Oil solution is composed of 1% v/v Span80 and 45 ml of Mineral Oil. The two phases are homogenized for 20 minutes at 7000rpm, then a second water phase containing 0.1% wt/v HA and 30% wt/v of TPP is added dropwise to the previous emulsion and it is homogenized at 7000 rpm for further 30 min. The obtained emulsion is stirred at 300 rpm over night until that the coacervation of HA occurs. Then, different purification steps are made in order to remove the oil phase and to purify the obtained NPs.

2.3.2 Preparation of labeled peptide Biotin-EYVNCDNLVGNCVIRG-VivoTag 750S

Peptide Biotin-EYVNCDNLVGNCVIRG lyophilized is prepared by dissolving 1mg in 1mL of 50 mM carbonate/bicarbonate buffer, pH 8.5, with a concentration of 1mg/mL.

One mg of VivoTag® 750-S, a near infrared fluorescent imaging labeling agent containing an N-hydroxysuccinimide (NHS)-ester, is reconstituted with 100 µL of DMSO in a dark vial. 200 µL of peptide solution is incubated with 20 µL of VivoTag® 750-S solution for one hour without direct exposure to light at room temperature. After incubation, the reaction mix is purified by a size exclusion chromatography Sephadex™ G-25 Medium PD-10 Desalting (GE Healthcare). The elution monitoring and determination of protein concentration are performed spectrophotometrically at 280 nm and 750 nm. After the purification, a peptide at a concentration of 0.1 mg/mL is obtained and a fluorophore concentration of 169 µM. The solution is stored at 4 °C in a dark vial.

2.3.3 General strategies for the conjugation of peptides and PEGylation

The obtained NPs are conjugated with PEG and different peptides. In the following paragraphs, the conjugation protocols are presented.

2.3.3.1 Conjugation of NPs with peptides
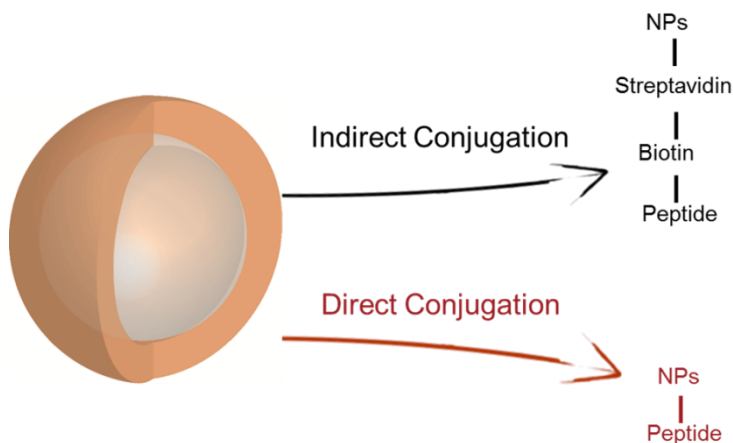
*Figure 2-2: **Set of performed reactions:** Schematically representation of the two types of performed reaction to conjugate the NPs with the selected peptides.*

To have an active targeting, the obtained NPs are conjugated with peptides A-20-6, A-20-36, A-20-S using two different strategies called *direct* and *indirect conjugation* (Figure 2- 2). The different peptides differ from each other for the terminal aminoacid.

Carbodiimide chemistry is used for bioconjugation of nanoparticles. Carboxyl groups exposed by an external shell made of HA are covalently bonded to amine group-bearing functional moieties through EDC/NHS linkers, forming an amide linkage. In the case of the direct reaction, the NPs are directly conjugated with the peptides after the activation by EDC/NHS of the carboxylic groups.

Differently, in the indirect strategy, the Carboxyl groups of HA are activated by EDC/NHS and the streptavidin covers the whole surface of the NPs. Only at the end, the peptides reacted by biotin covalently. These two strategies are performed in order to study the biodistribution of the conjugated NPs in presence and in absence of the streptavidin, which is already present naturally in the body and so it may accumulate easily in vivo.

2.3.3.2 Direct Conjugation Protocol

250 µl of EDC and 250 µl of NHS are added to 500 µl of NPs, after 10 min of stirring 50 µl of peptide 1mg/ml (A-20 S, A-20-36, A-20-6) are added. After 3h the reaction of conjugation is completed. After the addition of peptides or the PEG-Cy7, a purification protocol (ultracentrifuge: 7000rpm, 4°C, 15min) is erquired to clean the NPs solutions from the residual reaction components. In addition, after the purification through dialysis, the NPs are suspended in 1 mL PBS 1ml.

2.3.3.3 Indirect Conjugation Protocol

250 µl of EDC and 250 µl of NHS are added to 500 µl of NPs. After 10 min, 100 µl of Streptavidin (1mg/ml) are added and the final suspension is stirred overnight. After the overnight, the NPs are separated by the residual of Streptavidin using an Ultracentrifuge (Conditions: 20 min, 4°C, 7000 rpm). Then, 50 µl of peptide 1mg/ml are added to the suspension of NPs with Streptavidin obtained. The reaction of conjugation is completed after 3h.

After the addition of peptides, it is required a purification protocol to remove the residual reaction components from the NPs suspension. The NPs are purified using dialysis tubes 50kDa in a water phase. In addition, after the purification through dialysis, the NPs are suspended in PBS until 1ml.

2.3.3.4 PEGylation

230 µl of EDC and 230 µl of NHS are added to 500 µl of NPs in order to activate the carboxylic groups of the external shell made of HA. After 10 min of stirring 40 µl of PEG-FITC (1mg/ml) are added. The conjugation reaction is kept under continuous stirring overnight.

2.3.3.5 Cell line growth conditions

The A20 B-cell lymphoma cell line bear surface IgG (sA20-Ig), which is also secreted in the culture medium (A20-Ig). The A20 cells are adapted to growth in serum-free culture medium supplemented with 50 units/ml penicillin, 50 µg/ml streptomycin and 2 mM L-glutamine. Culture supernatant of A20 cell produced 2–10 µg/ml of A20-Ig, as estimated by ELISA. The surface IgG-positive 5T33MM B cell line was grown in RPMI medium, supplemented with 10% fetal bovine serum, 50 units/ml penicillin, 50 µg/ml streptomycin and 2 mM L-glutamine. The A20-Ig was purified from the culture supernatants by using the Mab Trap™ antibody purification Kit (GE Healthcare), according to the manufacturer's instructions.

2.3.4 Physical characterization

2.3.4.1 Advanced Electron Microscopy

A field emission gun (FEG) scanning electron microscope (SEM) Zeiss®, transmission electron microscope (TEM) FEI® in DRY and CRYO mode, Confocal Microscope (STED Stimulated Emission Depletion) are used in order to characterize the system morphologically. The SEM characterizations are made after the dialysis to control the integrity of the nanostructures by collecting the nanoparticle on an ISOPORE membrane (pore size 100nm.) The sputter coating of the samples is made with 7nm Au. The TEM analyses are brought forward both in DRY mode and Cryo Mode. In the DRY mode, the samples are prepared using Formvar/Carbon 200 mesh Cu Agar® using 20µl of the suspended nanoparticles. For CRYO-mode, lacey carbon membranes on 300-mesh copper grids are used. A sample of the diluted suspension is dropped on the grid, blotted to a thin film with filter paper, and immediately plunged into liquid propane/ethane (-186 °C) using a vitrification system (Vitrobot, purchased by FEI). A Gatan model 626 cryo-transfer station and a cryo-holder are used to transfer the grid containing the vitrified suspension into a TEM Tecnai FEI 200 kV. Hydrodynamic diameter and size distribution of the nanosystems are measured using a Zetasizer Nano ZS instruments (Malvern Instruments Ltd., Worcestershire, UK), at an operating wavelength of 532 nm. Measurements of size distribution and the Z-average size of

nanoparticles are performed at 25 °C with an angle detection of 173° in optically homogeneous glass cuvettes. The samples are taken from the suspension. The Zeta potential is used in the same way by determining the Electrophoretic Mobility in a Folded Capillary Zeta cell. Each sample is measured five times and average serial data are calculated. Stimulated Emission Depletion (STED) or Confocal Microscopy, dependence on the wavelength, are used to evaluate the fluorescence and stability of the NPs. The samples are prepared drying 20µl of nanoparticles suspension deposited on a FluorDish. Nanoparticles are diluted in Ethanol or in Phosphate-Buffered Saline (PBS). A typical dilution factor is 1:100.

2.3.5   Quantitative Analysis

2.3.5.1   PEG Concentration
The amount of PEG-FITC conjugated to the NPs is calculated by Spectrofluorimetry (EnSpire Multimode Plate Reader PerkinElmer). Different concentrations of the NPs suspension are investigated and compared with a calibration line. Each measurement is made in triplicate.

2.3.5.2   Bicinchoninic Acid Protein (BCA) Assay
To determine the concentration of the peptide on the surface of the NPs, the BCA assay (QuantiProTM BCA assay kit, Sigma-Aldrich) is used. This Assay is chosen because it is extremely precise, in fact, it has been able to detect an amount of 0.5µg/ml. The bicinchoninic

acid under alkaline conditions is a highly sensitive reagent, stable and specific for the Cu+, and forms with it a compound of the intensity of the purple color that is proportional to the amount of presented protein[10] [11].

The variation of the intensity of the signal is determined by absorbance spectrophotometer measures at 562nm.

150µl of NPs suspension are added to the same quantity of the working reagent solution and the obtained suspension is incubated at 37°C for 2h. The results are compared with a calibration line of Bovine Serum Albumin (BSA) and the concentration value is extrapolated by a calibration line designing by using BSA samples at a known concentration (0-40 µg/ml). All the measures are made in triplicate.

2.3.6   Fluorescence Tomography (FMT) Analysis Protocol

Mice blood clearance, organ distribution and in vivo imaging are investigated with an FMT 4000 TM fluorescence system (PerkinElmer, Massachusetts USA) equipped with four channels.

The FMT analysis are conducted on C57/BULB mice model subjects. After 12 days of tumor cells injections, all mice are divided into 4 groups divided for intravenously injection: the first (n = 12) received 100 µL of Vivotag 750S conjugated with peptide, the second (n = 12) received 100 µL of Peptide A-20-36-NPs, the third (n

= 12) received100 µL of Peptide A-20-s-NPs, the fourth group of ctrl mice received 100 µL of A-20-36-NPs. All nanoparticles are loaded with the ATTO680 and the FMT instrument is adequately calibrated. During FMT studies animals are maintained in general anesthesia and at 37 °C body temperature. Anesthesia is initially delivered in an induction chamber saturated with 5% isoflurane (Iso-Vet 1000 mg/g Inhalation Vapor, Piramal Healthcare UK Ltd., Northumberland, UK) in oxygen (2 L/min) and subsequently maintained during all procedures with isoflurane (2.5% during FMT examination) in oxygen at 2 L/min. For each mouse, we performed a basal scan of about 10 minutes and we injected 100 μl of contrast agent into the tail vein and wait 30 minutes for the dye biodistribution. Imaging is performed at 1, 2, 4, 6, 24 h post injection, which collected both 2D surface fluorescence reflectance images as well as 3D FMT imaging datasets, we used a proprietary software (TrueQuant 3.1) for the quantitation of three-dimensional fluorescence signal within mice body. At the end of the FMT study animals are sacrificed, tumors are surgically removed, and immediately frozen in liquid nitrogen and, for immunohistochemical analysis. A two-dimensional region of interest (ROI) is placed on the whole tumor area including about five millimeters of neighboring apparently normal tissue, or on the whole lower abdomen / pelvic area in the positive control mice, i.e. a tumor-bearing mice injected with VivoTag®-S 750 (PerkinElmer Inc., Waltham, MA, USA) and HyCoS. In each mouse, the ROI is

duplicated without changing its dimensions, to reduce this source of bias as much as possible. The signal intensity (I) obtained in counts/energy at each time point (I_t) is normalized to the background signal (I_B) according to the formula: $I_{norm} = (I_t - I_B) / I_B * 100$. The I_{norm} resulting significantly different between groups are reported as mean ± standard error of the mean (SEM). A multivariate analysis of variance for repeated measures (RM-MANOVA) is used to study the fixed effects of the treatment group (NPs + PEP, NPs + Scrambled PEP, VivoTag), of the time and of the interaction of the time over groups (a difference in the "slope" of the curves between groups).

The imaging sessions are rapid (2-3 minutes per animal) and for this range of time the mouse remains stable and immobilized for consistent, repetitive imaging results.

The FMT investigations are made at different time steps in order to control the biodistribution of the complex peptide-NPs. The animals are monitored until recumbent.

2.4   Results

In this second chapter, the effect of the chemical decoration of the HyCoS NPs is studied. Two different conjugation protocols are presented in order to functionalize HyCoS NPs with selected peptides and PEG. The functionalized NPs are used for optical imaging and active targeting to detect B-cell lymphoma in C57 bulb mice model.

2.4.1 Morphological and Super Resolution characterization

In Figure 2- 3, the produced NPs, obtained by the emulsion-coacervation method, are shown. During the process of production of the NPs both the dye (ATTO 680) and the MRI contrast agent (Gd-DTPA) are encapsulated. This peculiarity allows the NPs to be used for multimodal diagnostic applications.

The TEM analysis in Figure 2- 3 A shows a core-shell architecture of the obtained NPs shown in SEM image (Figure 2- 3 B) while the confocal image (Figure 2- 3 C) shows that the encapsulated dye (ATTO680) is presented in the whole NPs without any difference between the core and the shell.
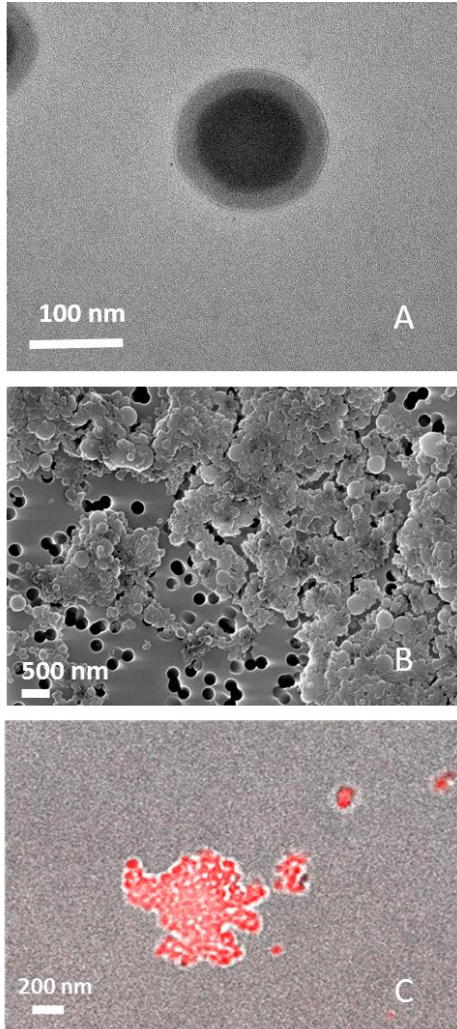
*Figure 2-3: **Morphological and Optical characterization of produced NPs.** NPs are morphologically characterized before the conjugation with PEG and peptides. A) TEM characterization of core-shell NPs, B) SEM image of NPs and C) Confocal image of NPs in which the encapsulated dye is shown in the whole nanovectors.*

2.4.2   Direct Conjugation Protocol

The NPs conjugated using the direct conjugation protocol are directly linked to the chains of the HA of the shell after their activation using EDC and NHS. In Figure 2- 4, NPs after the conjugation using the direct protocol are shown. In particular, the NPs conjugated with pA20-6 are shown in Figure 2- 4 A, the NPs conjugated with pA20-36 are shown in Figure 2- 4 B while the NPs conjugated directly with pA20-s are shown in Figure 2- 4 A.

*Figure 2-4: **SEM images of conjugated NPs using the direct protocol.** A) NPs conjugated with pA20-6, B) NPs conjugated with pA20-36 and C) NPs conjugated with pA20-s.*

2.4.3   Indirect Conjugation Protocol

In Figure 2- 5 it is possible to notice that the NPs continue to maintain their stability also after the conjugation. By this picture both the core and the shell can be clearly distinguished, furthermore, it is possible to notice a first layer of streptavidin and a final one of the peptide. In detail, in Figure 2- 5, NPs after the conjugation with the different peptides using the indirect conjugation reaction are shown. In particular, the NPs are conjugated with pA20-6 (Figure 2- 5 A), with pA20-36 (Figure 2- 5 B) and pA20-s (Figure 2- 5 C). The Figure 2- 5 shows that the NPs conjugated with the indirect conjugation protocol continue to maintain their stability and are completely covered by a layer of streptavidin linking the specific peptide.
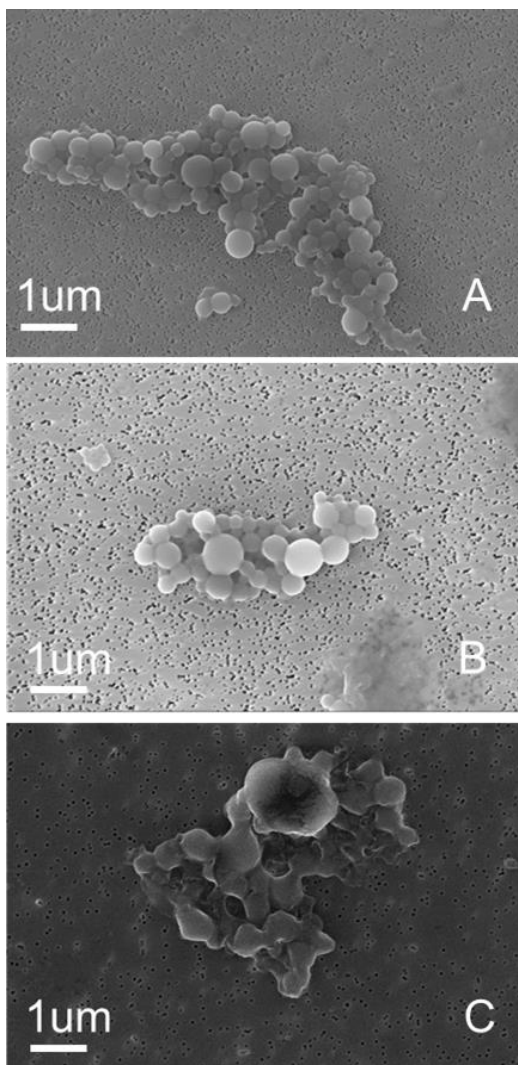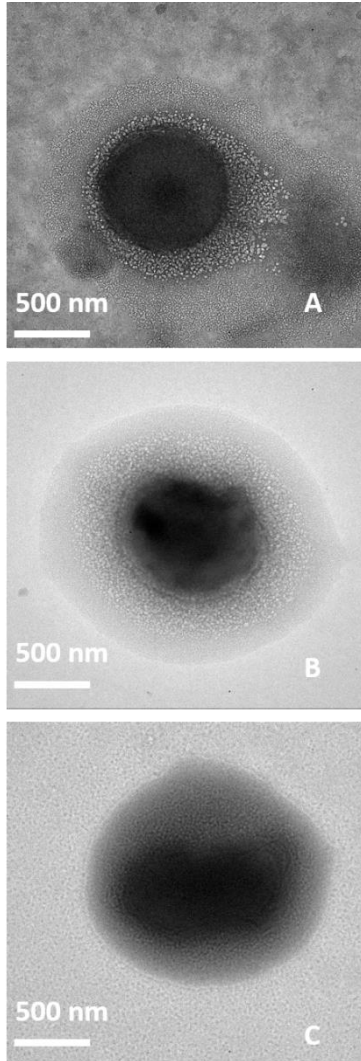
*Figure 2-5: **TEM images of conjugated NPs using the indirect protocol.** A) NPs conjugated with pA20-6, B) NPs conjugated with pA20-6 and C) NPs conjugated with pA20-s.*

2.4.4 PEG Conjugation Protocol

In addition to the conjugation with the peptides, the NPs are subjected to a second conjugation with a PEG-FITC 1KDa. In Figure 2- 6 A is reported a TEM image of PEG-FITC-NPs in which can be noticed the presence of chains of PEG-FITC of about 100nm arranged all around the NPs. The Figure 2- 6 B shows the NPs at confocal microscopy, in particular the image shown confirms the presence of a layer of dye which is conjugated with the PEG. In the case of fluorescent polystyrene (PS) NPs it has been possible to evaluate the simultaneous presence of the two dyes, the one which is already present in the polymeric NPs and the conjugated one.
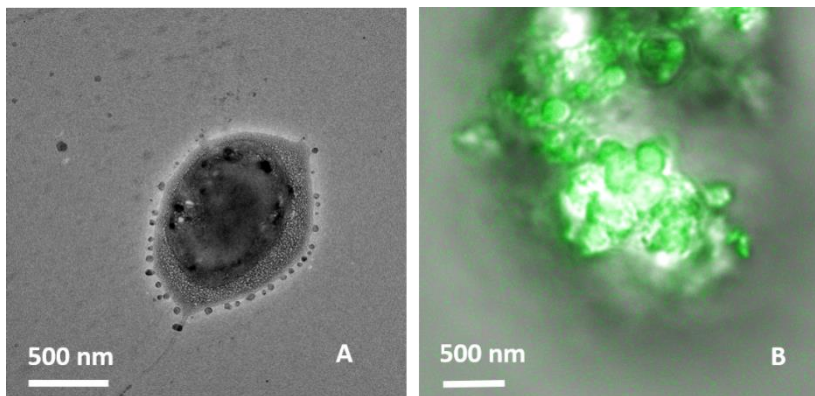
*Figure 2-6: **NPs conjugated with PEG-FITC 1kDa.** A) TEM image of PEG-FITC-NPs and B) Confocal Image of PEG-FITC-NPs 488nm.*

In order to evaluate the correct protocol for the NPs conjugation, the –COOH groups presented on the surface of the NPs are evaluated by volumetric titration.

In Figure 2- 7 there is a graphical representation of the equivalence point obtained by volumetric titration HCl-NaOH.
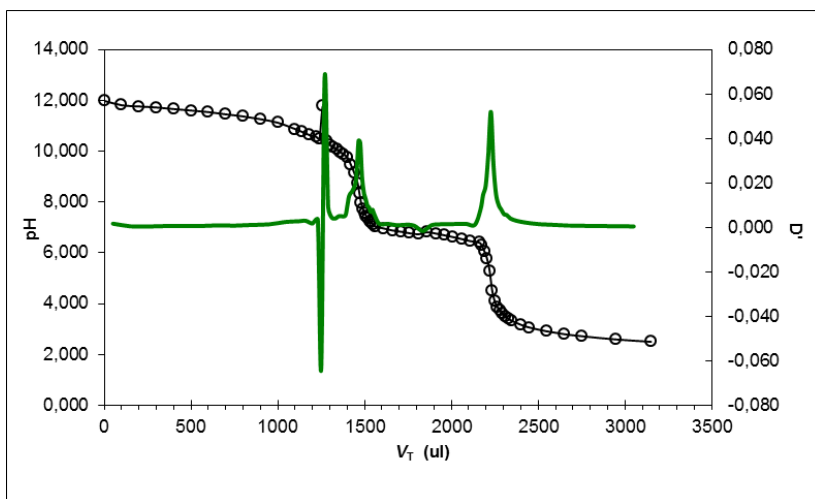
Figure 2-7: **Volumetric Titration:** *Representation of the equivalence point obtained by volumetric titration HCl-NaOH*

The results of the volumetric titration report 4 mol/ml of –COOH groups for HyCoS NPs. The amount of PEG-FITC which is conjugated to the NPs is evaluated by the spectrofluorimeter using polystyrene NPs as model NPs. For the polystyrene NPs (Ex/Em

650/680 nm) the range of concentration in which it is possible to detect the fluorescence has been evaluated as 1-150 µg/ml. In this range, there are no saturation events of the signal and the performed experiments made at different dilutions confirm there are no shielding effects of the NPs. After the purification steps, and due to the analyses to quantify the pegylation and bioconjugation the loss of an amount of NPs is confirmed. The initial concentration of NPs is 1250 µg/ml while that one measured after the reaction is 1077 µg/ml, it confirms the 14% w/v of loss of NPs using the calibration line reported in Figure 2- 8.
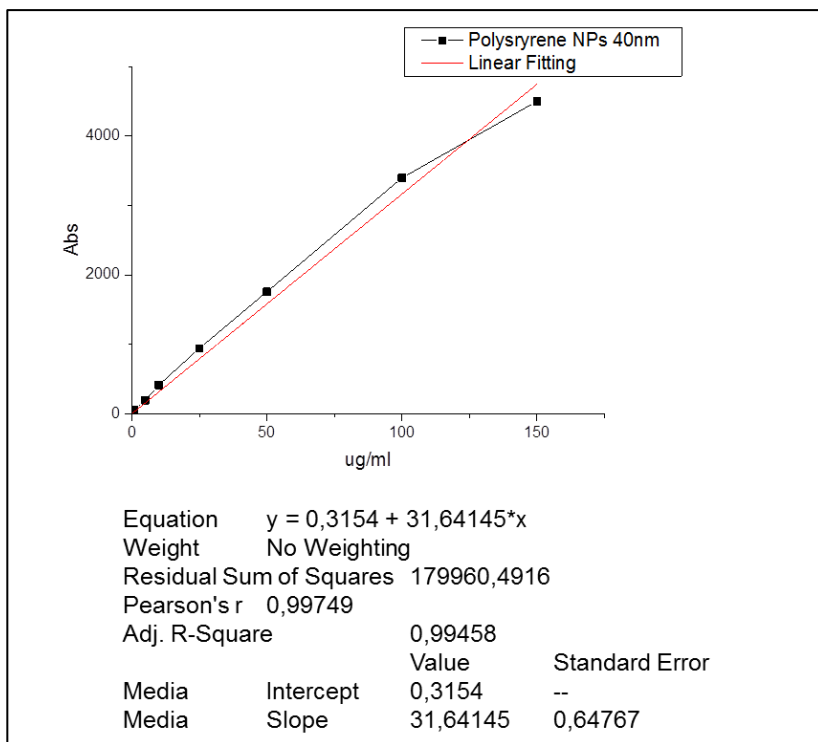
Figure 2-8: **PS NPs:** Calibration Line range 0-150 µg/ml.

The amount of conjugated PEG is measured by comparison of different ratios of the suspension dilutions of NPs with a calibration line of PEG-Cy-7 (Ex/Em 730-820) in a range of 0-40 nmol/ml (Figure 2- 9). The result of this investigation reports 27.8 nmol/ml with a final yield of 68.95% w/v.
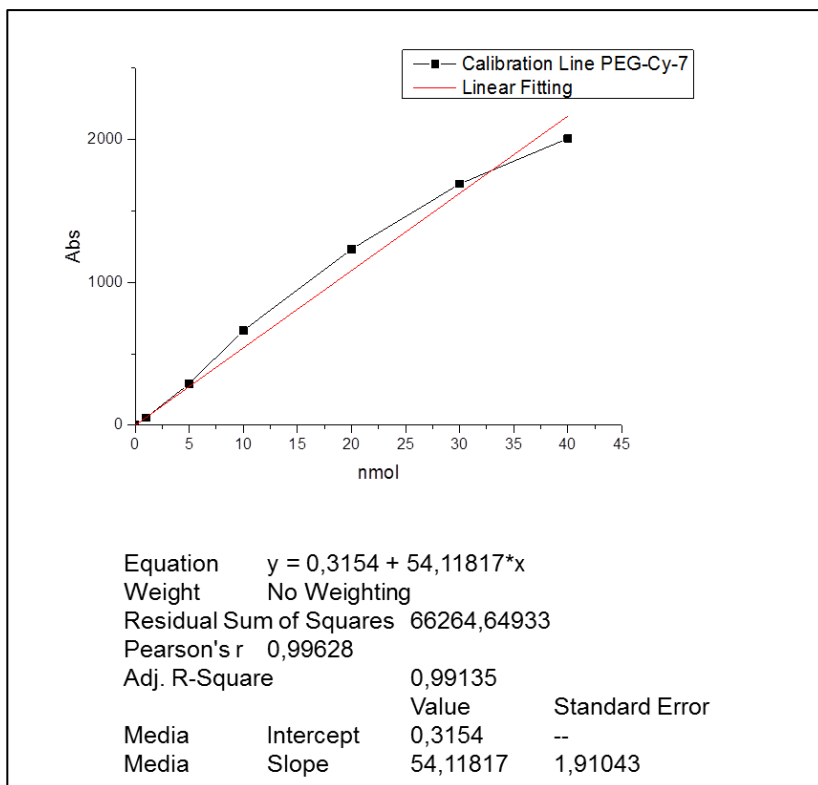
*Figure 2-9: **PEG Cy-7**: Calibration line in the range 0-40 nmol/ml.*

.

In the case of NPs the spectrofluorimeter analysis is made in the range 0-100 nmol/ml (Figure 2- 9). The result of this analyze reports a concentration 26.74 nmol/ml with a final yield of 66.85% w/v for the HyCoS NPs.
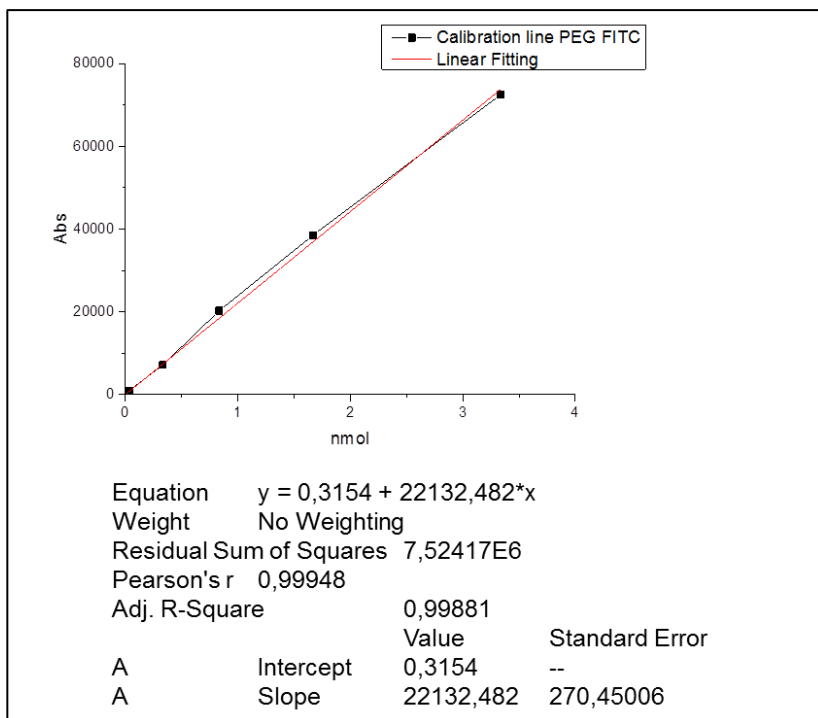
*Figure 2-10: **PEG-FITC 1KDa:** Calibration line in the range 0-80 nmol/ml.*

In order to determine the concentration of the specific peptide which is presented on the surface of the NPs the BCA assay has been used (Figure 2- 11). In particular, for the indirect reaction a double quantification is performed, the first analysis is made on the sample after the conjugation with the streptavidin while the second one on the final sample after the conjugation with the peptide.

Equation   y = a + b*x
Weight   No Weighting
Residual Sum of Squares 2,7365E-4
Pearson's r   0,99914
Adj. R-Square   0,99794
                          Value   Standard Error
A   Intercept -0,00839   0,00363
A   Slope   0,02245   4,16687E-4
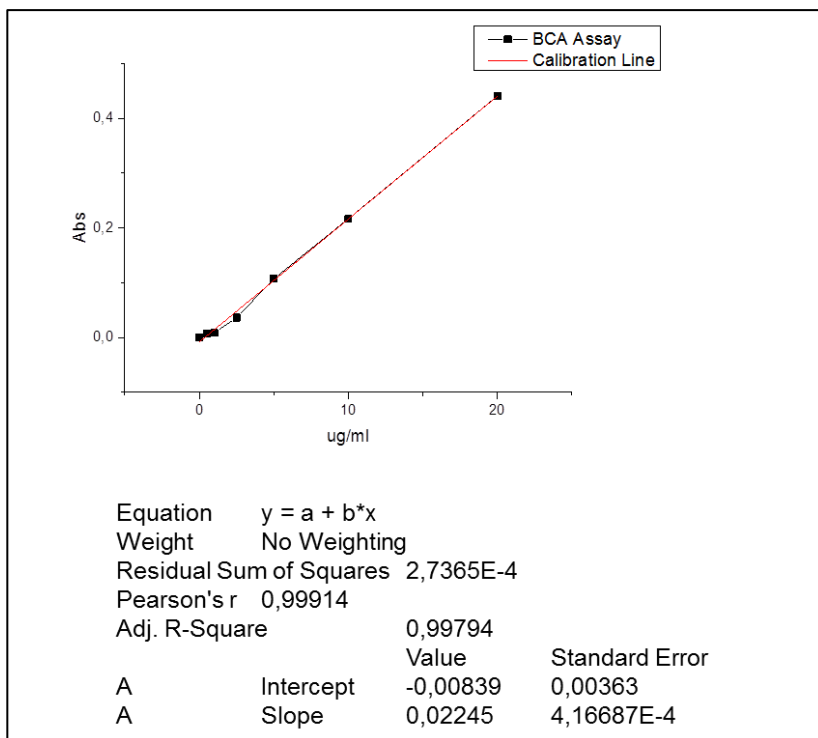
*Figure 2-11: **BCA Assay**: Calibration line Bovine Serum Albumin (BSA) 562 nm.*

The results are respectively 47.5 nmol/ml with a yield of 47.5% after the conjugation with the streptavidin and 40 nmol/ml with a yield of 80% after the conjugation with the peptide pA20-36 respect to that Polystyrene NPs with 200 nmol/ml and a yield of 66% after the streptavidin and 130 nmol/ml with a yield of 65% after the conjugation with the same peptide.

In the case of direct conjugation, the quantification of the peptide is made only on the final sample. The analysis reported 22 nmol/ml after the conjugation with the pA20-36 peptide with a yield of 73% respect to 135 nmol/ml for PS NPs with a yield of 33%.

For the reaction of double functionalization, PEG-FITC and peptide, both a quantification of PEG-Cy7 by spectrofluorimeter and proteic quantification are performed. The results are 2 nmol/ml (yield 25%) and 15 nmol/ml (yield 75%).

2.4.5   pH-triggering behavior
The obtained NPs have demonstrated a pH triggering behavior; in fact they tend to dissolve at pH strong acid while they tend to maintain their shape at basic conditions. Thanks to the pH triggering in the presence of a tumor mass, which is characterized by acid pH conditions, the NPs could swell releasing the cargo of dye and contrast agent directly in the tumor mass improving the detection.

2.4.6   *In vivo* results
The in vivo FMT studies are performed at baseline, i.e. prior to the i.v. injection of NPs, to obtain the background signal, and hence, based on previous results, 1, 2, 4, 6 and 24 hours after the NPs injection. The main results of FMT *in vivo* acquisitions are presented In Figure 2- 12 for NPs conjugated with A-20-36 and A-20-s peptides using the direct strategy. The NPs conjugated with A-20-36 peptide is the unique that has shown an accumulation compared to

the control peptide A-20-s. The Figure 2- 12 A, B and C represent the FMT acquisitions at 0h (basal acquisition), 6 and 24 hours respectively after the injection of NPs conjugated with A-20-36, while the Figure 2- 12 D, E and F represents the FMT acquisition respectively at 0h (basal acquisition), 6 and 24 hours after the injection of NPs conjugated with A-20-s. In the basal acquisition Figure 2- 12 A and D in the images there is not an intensity profile in correspondence of the tumour. Post 6h after the NPs injection, only in the Figure 2- 12 B it is possible to notice an accumulation of the nanotracers while it is not present in Figure 2- 12 E in which the NPs with the control peptide A-20-s are injected. After 24h, Figure 2- 12 C and F in both the images there is not an accumulation of the probe highlighting the clearance of the NPs themselves.
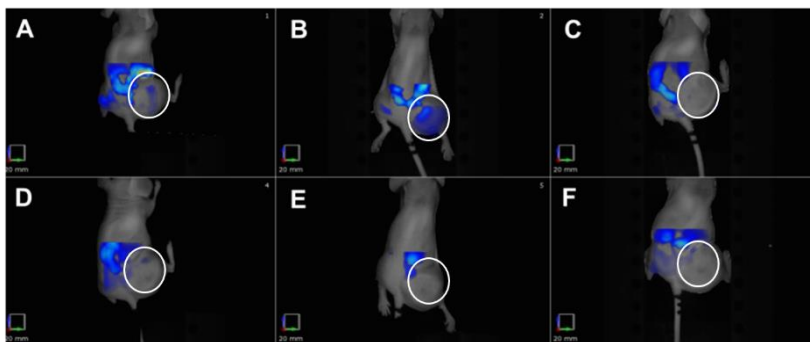
Figure 2-12: **In vivo FMT analysis:** Results of administration of NPs conjugated with A-20-36 (Upper image) and with A20-s (Lower images): Basal FMT acquisition (On the left), post 6h FMT acquisition (center) and post 24h FMT acquisition (on the right).

The graphic in Figure 2- 13 shows an accumulation of VivoTag 680 conjugated with peptide A-20-36 after 1h from the injection (blue line) of 67 pmol. Differently, the NPs conjugated with A-20-s peptide present an accumulation in the tumor microenvironment after 6h from the injection (red line) of 43 pmol. These results are obtained by performing a quantitative analysis of the Region of Interest by FMT measurements. The clearance profile of the two probes is similar, in fact both the tested probes are completely expelled from the body after 24h from the administration. The designed NPs unlike the only dye conjugated to the peptide remain for the same time in the body but have an accumulation peak later.
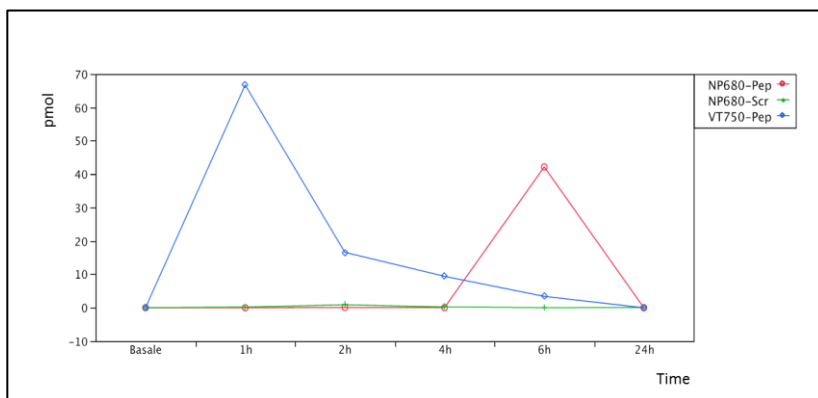
Figure 2-13: **Concentration Profile:** Measure of the pmol of NPs conjugated with peptide by FMT: A-20-36(red line), A-20-s (green line) and VivoTag conjugated with A-20-36 peptide (blue line).

The RM-MANOVA highlighted a significant influence of all the above-mentioned effects (P=0.001; Figure 2- 14). The *post hoc* analysis identified the following significant differences: at one hour post injection, the VivoTag group had a normalized signal intensity significantly higher than both the NPs-A-20-36 and NPs-A-20-s groups (21.1 ± 3.4 vs. 4.7 ± 1.1 vs. 2.7 ± 1.7 %, respectively; P=0.004); at four and six hours, the NPs-A-20-36 had a normalized signal intensity significantly higher than both the VivoTag and NPs-A-20-s groups (four hours: 38.9 ± 6.9 vs. 2.1 ± 0.4 vs. 14.8 ± 3.1, respectively; P=0.0005 and P=0.02, respectively – six hours 24.2 ± 0.4 vs. 1.5 ± 0.3 vs. 8.5 ± 3.5 %, respectively; P=0.0002 and P=0.002, respectively). At six hours, a difference between NPs-A-20-s and VivoTag groups was detected, as well (P=0.047).
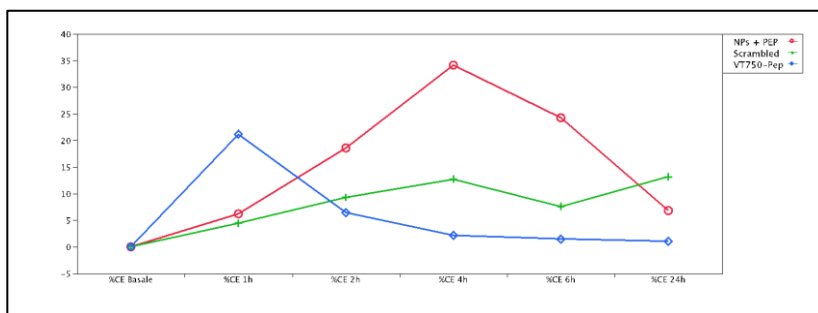
Figure 2-14: **Graphic representation:** Mean normalized intensity of the ROI over time (P<0.01). In red, the negative control group; in green, the NPs-A-20-36 group; in blue the NPs-A-20-s group.

2.4.7　Ex vivo Results

Based on the *in vivo* biodistribution, *ex vivo* fluorescent confocal microscopy is performed. Briefly, three mice from each group are euthanized under general anesthesia after three hours of biodistribution of the injected contrast agent (NPs-A-20-36, NPs-A-20-s, VivoTag). The tumors are removed from each mouse under a dissecting microscope, snap frozen in liquid nitrogen into a 50 ml falcon vial, and stored at -80°C until analysis. Five µm slices are obtained with a cryostat microtome and stained with 4',6-diamidino-2-phenylindole (DAPI). The slices are hence studied with the opportune excitation/emission wavelengths. The results of the fluorescent confocal microscopy confirm the *in vivo* results (Figure 2- 15). In particular, the results show an accumulation of NPs –A-20-36 (Figure 2-15 A and B) higher than what obtained for VivoTag®-S 750 (Figure 2-15 C).
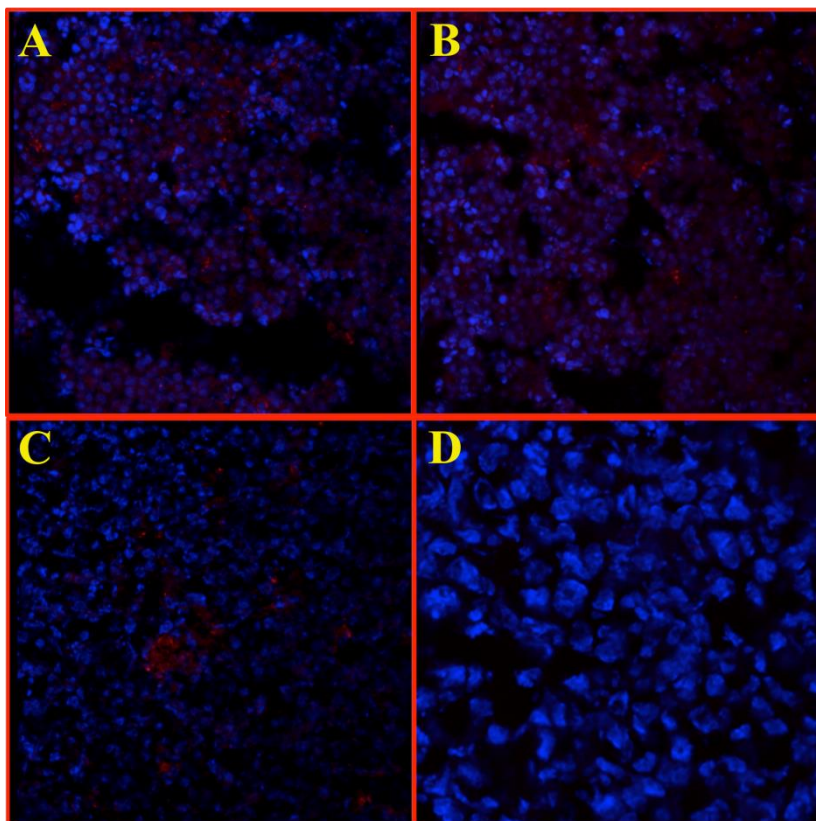
*Figure 2-15: **Ex vivo:*** Confocal fluorescent microscopy of tumors stained with DAPI after three hours of biodistribution. In A and B: two different mice injected with NPs-A-20-36. In C: mice injected with VivoTag®-S 750. In D: mice injected with NPs-A-20-s. The images have obtained with the identical settings of background thresholding and fluorescence intensity.

2.5 Discussion

The described nanoparticles produced by the coacervation method have been shown to maintain their stability, assessed by SEM and TEM analysis, even after conjugations.

Despite the many application advantages in the use of NPs, some fundamental problems hamper their distribution such as the uptake by the Reticulo-Endothelial System (RES), accompanied by rapid expulsion from circulation to the liver, the spleen or the bone marrow and the possibility of incurring the formation of non-specific binding with the healthy areas or which do not represent the biological target. The addition of PEG to the surface (PEGylation) can reduce modify the layer at the interface of the nanoparticles and biological barriers, increasing the timing of movement and half-life ($t½$) and enable long circulation of more than 50% of the injected NPs. This effect is also obtained for a compound eventually entrapped within the probe. In this way, it will be possible to control the residual interference of NPs with the RES lowering also the potential exposure of healthy organs to the drug.

In addition to the PEGylation, the two conjugation protocols used to functionalize NPs with different kinds of peptides are carried out in order to evaluate the different biodistribution of the functionalized nanoparticles in the presence or not of streptavidin. Streptavidin is in fact highly similar with biotin tending to bond more to tissues when it is injected into the body. The surface coated with streptavidin is

presented as a powerful and universal tool for tying all types of biotinylated molecule. For this reason, the conjugated nanoparticles using the direct protocol show a significant accumulation than those linked to the peptide in a non-specific manner that begins probably to stick to all tissues indiscriminately from the time of injection without accumulating in the tumor area of interest. Furthermore, due to the above described pH-sensitive behavior reported in vivo, it is possible that, once NPs reach the tumor environment, characterized by an acid pH, they could disintegrate, releasing the dye encapsulated thus allowing a better localization of the optical tracer. This peculiar yet interesting behavior required further investigations as so the ability of the A20 -36 –HyCoS NPS to reduce the tumor growth.

2.6 Conclusions

The obtained NPs can be functionalized and PEGylated without altering the stability of the designed nanovector. The resulted probes can be used for multimodal imaging applications, in particular their use is devoted to the MRI and Optical Imaging for the detection a specific disease thanks to the active targeting. Indeed, the NPs oppurtunely functionalized have accumulated in the tumor microenvironment of a B-cell lymphoma allowing the optical detection of the tumor lesion. Currently, the acquisitions of the data to evaluate the reduction of the tumor due to the accumulation of the HyCos NPs decorated with the peptide and in vivo MRI experiments on animal MRI 9.4 Tesla are work in progress.

References

1   Hanahan, D. & Weinberg, R. A. Hallmarks of Cancer: The Next Generation. *Cell* **144**, 646-674, doi:10.1016/j.cell.2011.02.013 (2011).

2   Aggarwal, B. B., Shishodia, S., Sandur, S. K., Pandey, M. K. & Sethi, G. Inflammation and cancer: How hot is the link? *Biochemical Pharmacology* **72**, 1605-1621, doi:10.1016/j.bcp.2006.06.029 (2006).

3   Jain, R. K. & Stylianopoulos, T. Delivering nanomedicine to solid tumors. *Nature Reviews Clinical Oncology* **7**, 653-664, doi:10.1038/nrclinonc.2010.139 (2010).

4   Lorusso, G. & Ruegg, C. The tumor microenvironment and its contribution to tumor evolution toward metastasis. *Histochemistry and Cell Biology* **130**, 1091-1103, doi:10.1007/s00418-008-0530-8 (2008).

5   Carmeliet, P. & Jain, R. K. Molecular mechanisms and clinical applications of angiogenesis. *Nature* **473**, 298-307, doi:10.1038/nature10144 (2011).

6   Jain, R. K. Taming vessels to treat cancer. *Scientific American* **298**, 56-63 (2008).

7   Jain, R. K. DETERMINANTS OF TUMOR BLOOD-FLOW - A REVIEW. *Cancer Research* **48**, 2641-2658 (1988).

8   Gullotti, E. & Yeo, Y. Extracellularly Activated Nanocarriers: A New Paradigm of Tumor Targeted Drug Delivery. *Molecular Pharmaceutics* **6**, 1041-1051, doi:10.1021/mp900090z (2009).

9   Byrne, J. D., Betancourt, T. & Brannon-Peppas, L. Active targeting schemes for nanoparticle systems in cancer therapeutics. *Advanced Drug Delivery Reviews* **60**, 1615-1626, doi:10.1016/j.addr.2008.08.005 (2008).

10   Fraisl, P., Mazzone, M., Schmidt, T. & Carmeliet, P. Regulation of Angiogenesis by Oxygen and Metabolism. *Developmental Cell* **16**, 167-179, doi:10.1016/j.devcel.2009.01.003 (2009).

11   Fang, J., Nakamura, H. & Maeda, H. The EPR effect: Unique features of tumor blood vessels for drug delivery, factors involved, and limitations and augmentation of the effect. *Advanced Drug Delivery Reviews* **63**, 136-151, doi:10.1016/j.addr.2010.04.009 (2011).

12   Schomber, T. *et al.* Differential effects of the vascular endothelial growth factor receptor inhibitor PTK787/ZK222584 on tumor angiogenesis and tumor lymphangiogenesis. *Molecular Cancer Therapeutics* **8**, 55-63, doi:10.1158/1535-7163.mct-08-0679 (2009).

13   De Bock, K., Mazzone, M. & Carmeliet, P. Antiangiogenic therapy, hypoxia, and metastasis: risky liaisons, or not? *Nature Reviews Clinical Oncology* **8**, 393-404, doi:10.1038/nrclinonc.2011.83 (2011).

14   Smallbone, K., Gavaghan, D. J., Gatenby, R. A. & Maini, P. K. The role of acidity in solid tumour growth and invasion. *Journal of Theoretical Biology* **235**, 476-484, doi:10.1016/j.jtbi.2005.02.001 (2005).

15   Jain, R. K. Delivery of molecular and cellular medicine to solid tumors. *Advanced Drug Delivery Reviews* **64**, 353-365, doi:10.1016/j.addr.2012.09.011 (2012).

16   Jain, R. K. TRANSPORT OF MOLECULES ACROSS TUMOR VASCULATURE. *Cancer and Metastasis Reviews* **6**, 559-593, doi:10.1007/bf00047468 (1987).

17   Albini, A. & Sporn, M. B. The tumour microenvironment as a target for chemoprevention. *Nature Reviews Cancer* **7**, 139-147, doi:10.1038/nrc2067 (2007).

18   Matsumura, Y. & Maeda, H. A NEW CONCEPT FOR MACROMOLECULAR THERAPEUTICS IN CANCER-CHEMOTHERAPY - MECHANISM OF TUMORITROPIC ACCUMULATION OF PROTEINS AND THE ANTITUMOR AGENT SMANCS. *Cancer Research* **46**, 6387-6392 (1986).

19   Decuzzi, P. *et al.* Size and shape effects in the biodistribution of intravascularly injected particles. *Journal*

of Controlled Release **141**, 320-327, doi:10.1016/j.jconrel.2009.10.014 (2010).

20 Ferrari, M. Cancer nanotechnology: Opportunities and challenges. *Nature Reviews Cancer* **5**, 161-171, doi:10.1038/nrc1566 (2005).

21 Florence, A. T. "Targeting" nanoparticles: The constraints of physical laws and physical barriers. *Journal of Controlled Release* **164**, 115-124, doi:10.1016/j.jconrel.2012.03.022 (2012).

22 Chauhan, V. P., Stylianopoulos, T., Boucher, Y. & Jain, R. K. Delivery of Molecular and Nanoscale Medicine to Tumors: Transport Barriers and Strategies. *Annual Review of Chemical and Biomolecular Engineering, Vol 2* **2**, 281-298, doi:10.1146/annurev-chembioeng-061010-114300 (2011).

23 Renschler, M. F., Bhatt, R. R., Dower, W. J. & Levy, R. SYNTHETIC PEPTIDE LIGANDS OF THE ANTIGEN-BINDING RECEPTOR INDUCE PROGRAMMED CELL-DEATH IN A HUMAN B-CELL LYMPHOMA. *Proceedings of the National Academy of Sciences of the United States of America* **91**, 3623-3627, doi:10.1073/pnas.91.9.3623 (1994).

24 Mori, T. Cancer-specific ligands identified from screening of peptide-display libraries. *Current Pharmaceutical Design* **10**, 2335-2343, doi:10.2174/1381612043383944 (2004).

25 Palmieri, C. *et al.* In vivo targeting and growth inhibition of the A20 murine B-cell lymphoma by an idiotype-specific peptide binder. *Blood* **116**, 226-238, doi:10.1182/blood-2009-11-253617 (2010).

26 Renschler, M. F., Wada, H. G., Fok, K. S. & Levy, R. B-LYMPHOMA CELLS ARE ACTIVATED BY PEPTIDE LIGANDS OF THE ANTIGEN-BINDING RECEPTOR OR BY ANTIIDIOTYPIC ANTIBODY TO INDUCE EXTRACELLULAR ACIDIFICATION. *Cancer Research* **55**, 5642-5647 (1995).

27 Cho, K., Wang, X., Nie, S., Chen, Z. & Shin, D. M. Therapeutic nanoparticles for drug delivery in cancer. *Clinical Cancer*

Research **14**, 1310-1316, doi:10.1158/1078-0432.ccr-07-1441 (2008).

28   Reubi, J. C. & Waser, B. Concomitant expression of several peptide receptors in neuroendocrine tumours: molecular basis for in vivo multireceptor tumour targeting. *European Journal of Nuclear Medicine and Molecular Imaging* **30**, 781-793, doi:10.1007/s00259-003-1184-3 (2003).

29   Scott, J. K. & Smith, G. P. SEARCHING FOR PEPTIDE LIGANDS WITH AN EPITOPE LIBRARY. *Science* **249**, 386-390, doi:10.1126/science.1696028 (1990).

30   Sun, L. C., Fuselier, J. A., Murphy, W. A. & Coy, D. H. Antisense peptide nucleic acids conjugated to somatostatin analogs and targeted at the n-myc oncogene display enhanced cytotoxity to human neuroblastoma IMR32 cells expressing somatostatin receptors. *Peptides* **23**, 1557-1565, doi:10.1016/s0196-9781(02)00096-7 (2002).

31   Brannon-Peppas, L. & Blanchette, J. O. Nanoparticle and targeted systems for cancer therapy. *Advanced Drug Delivery Reviews* **64**, 206-212, doi:10.1016/j.addr.2012.09.033 (2012).

CHAPTER 3

3 Gd-DTPA-HyCoS NPs (HyCoS) entrapping ¹⁸F-FDG for simultaneous PET/MRI acquisitions.
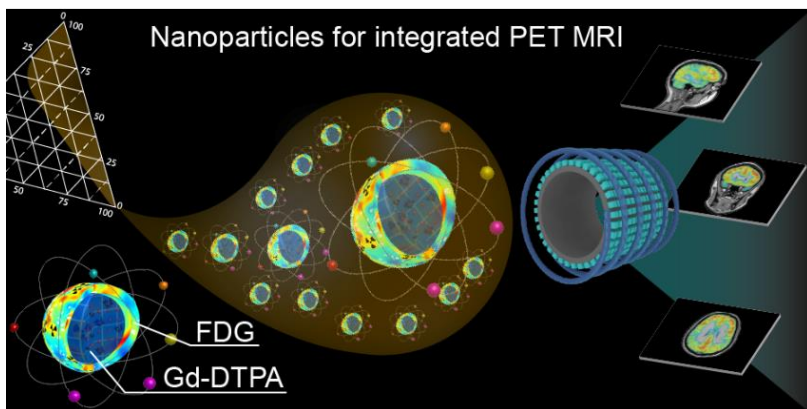
*Figure 3-1: **Graphical Abstract:** HyCoS NPs encapsulating ¹⁸F-FDG and Gd-DTPA for PET-MRI applications.*

3.1 Introduction

Nowadays, the modalities available for clinical imaging include optical imaging, magnetic resonance imaging (MRI)[1], nuclear imaging (Positron Emission Tomography (PET), Single Positron Emission Tomography (SPECT), computer tomography (CT), ultrasound (US) and dual imaging techniques as PET-CT or PET-MRI[2, 3]. In particular, the combination of both morphological (CT and MRI) and functional (PET and SPECT) methods[4], are used to increase the diagnostic accuracy[5]. These current technologies could have a huge impact in the early diagnosis[6] of different pathologies as neurodegeneration diseases[7] and, therefore, in the clinical management of cognitive decline in early-stage. In this context plays a key role the PET/MRI[4, 8]. The integrated PET/MRI system was born in 1997 [3] and has substantially transformed in the last years allowing the development of a new instrument that can be able to acquire the information simultaneously and to combine them in a unique high-resolution image[9]. The guarantee of having in a single image with a high anatomical detail which provides the information on the metabolic processes associated with a disease not only leads to save time and money but also gives the opportunity to make an early detection[10] and so to improve the effectiveness of the treatments[11]. Moreover, the simultaneous acquisition immediately brings to mind the possibility of improving the performance and information content of one instrument using the information obtained

by the other instrument: the accuracy of the PET might be improved by including the MRI information as the structural framework underlying the distribution of the PET signal. Reciprocally, the strength of PET to provide absolute quantitative information might help validate several MRI techniques in vivo[5]. With the combination of these two diagnostic techniques is also possible to monitor the therapy and to control if the suggested dose is enough for the disease. MRI and PET provide complementary anatomic, physiologic, metabolic and functional information. At the beginning, the use of these two techniques consisted of two sequential acquisitions and only after the two images, the PET one and the MRI one, are superimposed in a unique image. This type of acquisition has acted to different problems such as the effects of partial volume. Simultaneous PET/MRI allows for both spatial and temporal correlation of the signals, creating opportunities impossible to realize using sequentially acquired data[3]. The features of this new technology may be particularly appealing to applications in neuroscience[12] and translational neurologic and psychiatric research[13], considering that MRI represents the first-line diagnostic imaging modality for numerous indications and that a great number of specific PET tracers are available today to assess functional and molecular processes[14]. Nowadays, even though there are on sale a lot of different contrast agents and radiotracers there is not a single probe that can be used for the simultaneous PET/MRI acquisition.

Thanks to nanotechnology, the design of new probes that provide to the delivery of drugs and to the combination of different molecular targeting is possible[15]. In literature, various works of new multimodal probes for PET/MRI are presented but they are mainly based on the conjugation of a radiotracer to a carrier through a bioconjugation[16] and on the use of not completely biocompatible materials. Until now, the only way to use this technique is limited to the administration of a cocktail of contrast agents or tracers[17]. Lee et all [18] in 2008 presented a study in which Arginine-Glycine-Aspartic (RGD) were conjugated to Iron Oxide NPs to develop a PET/MRI probe for the detection of tumor integrin $\alpha_v\beta_3$. Hwang et al. [19] in 2010, presented a review in which is reported state of the art about the development of new nanoprobe for PET/MRI acquisitions. In 2010, Zhu et al [20] presented a new probe for PET/MRI formed by Mn-doped Fe_2O_4 (MnMEIO) with serum albumin (SA) conjugating them with [124]I. In 2011, a different probe for the multimodal imaging PET/MRI was presented by Uppal et al.[21], this probe was created combining Gd and ^{64}Cu to evaluate fibrin imaging effect on rats. Yang et al [22] demonstrated a drug delivery function for tumor application combining a tracer for MRI with a ^{64}Cu and a drug (Doxorubicin) conjugating them to SPIOs. In 2013, de Rosales [17] described the use of cocktails of imaging agents and bimodal agents to acquire information by PET/MRI technique and he presented a probe (SPIONs) conjugated with [64]Cu. Furthermore, already in 2011, he

presented a new probe for PET/MRI applications to demonstrate the high potential of bisphosphonates (BP)-iron oxide conjugation using ^{99m}Tc-dipicolylamine (DPA)-alendronate for SPECT/PET-MRI applications[23]. An important characteristic of the presented literature studies is the use of radiopharmaceuticals which have a very high half-life and that are not used in the clinical practice for their higher radioactive power. In this work, a core-shell polymeric probe which can be used as a tracer for integrated PET/MRI applications will be presented. Thanks to an active targeting, as showed in Chapter 2 for the Optical Imaging, the NPs could not follow the common metabolic pathway of the radiotracer but it would be able to reach the district of interest increasing safety for the patient following the clearance of nanoparticles[24]. The chosen radiopharmaceutical is Fluorodeoxyglucose (F^{18}-FDG)[24], which is the most commonly used in clinical practice for different kinds of diseases[25, 26]. This choice has been done in order to easily introduce the designed probe in clinical practice.

3.2 Materials

Chitosan (Ch) low molecular weight; Divinyl Sulfone (DVS) 118.15 g/mol; Sodium Tripolyphosphate (TPP) 367.86 g/mol; Glacial Acetic Acid molecular weight 60.05; Ethanol (EtOH) molecular weight 46.07; Gd-DTPA molecular weight 547.57; Mineral Oil 0.84 g/mL at 25°C (lit.); Span80 molecular weight 274.43; 1.005 g/mL at 20 C (lit.) are purchased by Sigma-Aldrich® while Hyaluronic Acid (HA)

850 kDa parenteral grade is by Hyasis. MilliQ water is for all experiments. Fluorodeoxyglucose (F^{18}-FDG) (0.014 mg/ml) is synthesized and provided by IRCCS SDN of Naples.

3.3 Methods

3.3.1 Preparation of HyCoS Nanoparticles and their collection

As previously reported in Chapter 1 (paragraph 1.3), HyCoSNPs are produced through a complex coacervation process in order to obtain a core-shell architecture (Chapter 1 paragraph 1.3). Briefly, the HyCoS NPs are composed of a Chitosan core o and a shell of HA. First of all, a w/o emulsion is prepared in order to obtain the core template. 50 ml of a solution of Mineral Oil at 1% v/v Span80 is homogenized at 7000rpm for 5 min. Then, an Acetic Acid (CH_3COOH) solution (34.93 mM) at 1% w/v Ch and 1% w/v Gd-DTPA is added to the previous oil solution and homogenized for 20min at 7000rpm in order to obtain a w/o nanoemulsion. Consequently, a water solution at 30% w/v of TPP and 0.1% w/v of HA is added to the previous emulsion and homogenized at 7000rpm for other 30min. At the end, the emulsion is kept under continuous stirring overnight at 300rpm. After that, the coacervation occurs HyCoS NPs a purified and collected in water using the same protocols detailly described in Chapter I (paragraph 1.3). After the purification step of the NPs, a step of concentration is necessary. 50 ml of NPs suspended in aqueous solution are concentrated in 5 ml by

Rotavapor R-215 Buchi (temperature of bath 37°C, 14mbar), achieving a concentration ranging from 3 to 5 mg/mL

3.3.2 Synthesis of ^{18}F-FDG

One of the most challenging aspects of this experimental part regards the synthesis of ^{18}F-FDG. The radiotracer has been produced in the laboratories of the diagnostic center IRCCS SDN located in Naples. First, the ^{18}F is produced by a cyclotron, then, through an automated system, the ^{18}F is transported in radiopharmacy inside the so-called Hot Cells where the reaction with the glucose for the formation of ^{18}F –FDG takes place. During the experimental campaign a whole batch of the just prepared radiotracers has been dedicated to the testing of the nanoparticles.

3.3.3 Absorption of ^{18}F-FDG in HyCoS NPs containing Gd-DTPA

The absorption procedure is conducted at the Radiopharmaceutical Department inside the Diagnostic Center IRCSS SDN in Naples where the laboratories and the equipment are adequate to manage a radiotracer in a safe way. Here, 100µl of NPs ($T_1=300 \pm 20$ms) are added to 100µl of ^{18}F-FDG (0.014 mg/ml) at about 60µCi/ml and kept under continuous shaking for 10min. This procedure is repeated at least four times for at least 4 batches to achieve the minimum detectable concentration to perform the PET/MRI test. Later, all the batches are collected added into a Concentrator Corning Disk (SPIN-X UF 30kDa of 20ml by SIGMA) with 1 ml of MILLIQ water and

all the system is put under vacuum allowing the separation of the residual radiotracer by the HyCoS NPs

Both the solution of water and the residual ^{18}F-FDG and the suspension of NPs are then collected in different tubes in order to measure their activities.

The radioactivity and the MRI signal of the Gd-DTPA-NPs absorbed ^{18}F-FDG are measured by an integrated PET/MRI Scanner at 3 Tesla by Siemens, Germany.The same experiments are made with decayed ^{18}F-FDG in order to establish by Mass Spectrometry (Agilent Technologies 6530 Accurate-Mass Q-TOF LC/MS) the amount of glucose presented into the NPs after the contact and purification process.

3.3.4 Simultaneous PET/MRI Acquisition

The radioactive HyCoS NPs are collected and together with the eluates of the relatives samples, inserted into dedicated phantom (NEMA 2012/IEC NEMA IEC Body Phantom) with fillable spheres (Figure 3-2) adequate to guarantee the measurement of the PET and MRI acquisition. The phantom is placed at the isocenter of the PET/MRI field of view to perform simultaneous PET/MRI acquistion. The eluates of the related samples are also measured to assess the efficacy of the sorption. The radioactivity in Becquerel (Bq) and the relaxometric properties in terms of T1 (ms) are simultaneously obtained by the PET/MRI scan.

Figure 3-2: **Phantom:** Ad hoc Phantom utilized to perform PET/MRI acquisition of HyCoS NPs by filling the low volume glass burette with a sample at a specific concentration.

3.3.5   In vitro MRI

Relaxation times are measured on a Bruker Minispec (mq 60) benchtop relaxometer operating at 60 MHz for protons (magnetic field strength: 1.41 T). The acquisitions are performed at 37°C, and before each measurement, the sample is placed into the NMR probe for about 15 min for thermal equilibration. Longitudinal relaxation times, T_1, are determined by both saturation (SR) and inversion recovery (IR) pulse sequences. The relaxation recovery curves are fitted using a multi-exponential model. Relaxivity values, r_1, are calculated from the slope of the regression line of $1/T_1$ [s^{-1}] versus concentration [mM] with a least-squares method using Origin Pro 9.1 SRO software (OriginLab Corporation, USA).

3.4 Results

In the design of a synthesis process that can be integrated in an industrial and certificated quality system currently in use in radiopharmaceutical laboratories for the development of a new multimodal probe, the first endeavor was to try to integrate the production process of polymeric NPs with the synthesis process of ^{18}F-FDG. Indeed, the starting idea has been to encapsulate glucose during the manufacturing process and later to perform in the Hot Cell the substitution of the glucose with the 18F directly within the nanoparticles. Unfortunately, the synthesis protocol of ^{18}F-FDG, such as the others radiopharmaceutical tracers, is made at a temperature profile not suitable for polymeric materials(104 ℃) (Figure 3- 2).
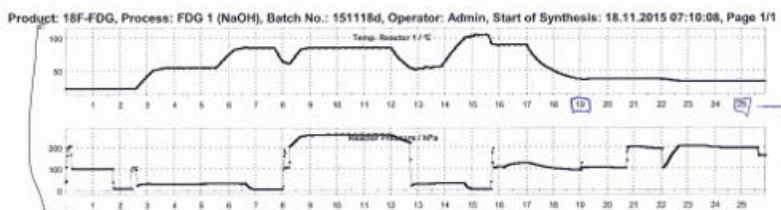
*Figure 3-3: **Profile of Pressure and Temperature:** ^{18}F-FDG synthesis. The top profile represents the temperature profile of the ^{18}F-FDG synthesis process (°C). The integration of NPs with the ^{18}F-FDG is performed from the minute 19 (signed in blue). The bottom profile is the pressure profile of ^{18}F-FDG synthesis (MPa).*

Beyond the difficulties related to the stability of the nanoparticles, even the quality controls of the products are compromised and our aim is to obtain a product as much as possible transferable to the

clinical applications. For this reason, the direct production of a polymeric NPs in the Hot Cells results not effective and extremely expensive. The second strategy we have carried out regards the combination of the ^{18}F-FDG with the polymeric NPs by absorption of the radiotracer. Indeed, after their production, HyCoS NPs are subjected to freeze-drying to remove the excess of water before keeping in contact the materials as described in the Method Section of this chapter. In conclusion, the best conditions of sorption in terms of the stability of the NPs and encapsulation efficiency are obtained by adding 100µl of a solution ^{18}F-FDG, at 0.014 mg/ml and about 60µCi/ml (t_0), to 500µl of NPs, at a concentration of 1 mg/ml and loading Gd-DTPA having a relaxation rate of (T_1= 300±20ms).

3.4.1 Evaluation of decay ^{18}F-FDG absorbed by NPs and their stability

In the following Figure (Figure 3- 3), a calibration line of glucose (range 0-0.014 mg/ml) used for the evaluation of the concentration of decayed ^{18}F-FDG (glucose) by Mass Spectroscopy is shown.
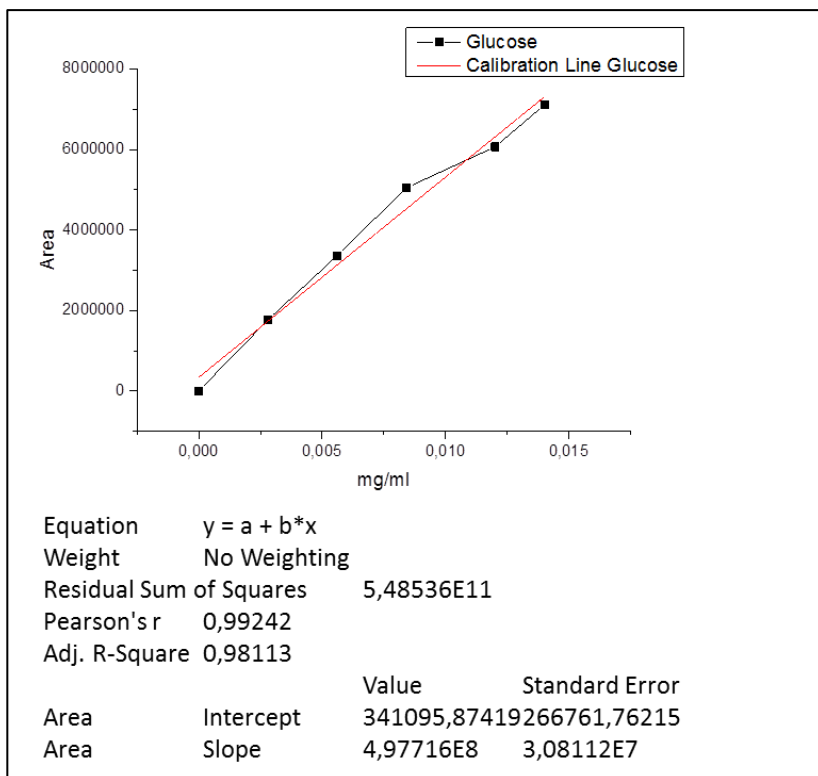
Figure 3-4: **Calibration Line of Glucose:** The quantification of the amount of decayed ^{18}F-FDG presented in the flowthrough and in the NPs is measured considering the calibration line of glucose.

After the contact and the purification protocols, glucose (decayed ^{18}F-FDG) concentration of 0.00325 mg/ml is measured on the flow-through collected at the bottom of the flask. The difference between the starting amount of used ^{18}F-FDG and what has been found in the flowthrough is reported in Table 2. The difference between the

Flowthrough (mg/ml) and the initial amount of ^{18}F-FDG gives us the quantity absorbed into the NPs.

*Table 2: **Mass spectrometry (MS):** Measures are made on eluate after a purification step of the particles. The results show a sorption of about 60% of the FDG after the contact of 10 min with the NPs. The stability of NPs is evaluated by SEM.*

Nps (µl)	FDG 0,014 mg/ml (µl)	Pre-filtration (mg/ml)	Nps InStability	Flowthrough (mg/ml)	Difference (mg/ml)	Sorption (%)
500	100	26,283E+13	Yes	ND	ND	ND
500	10	2,6283E+13	No	1,02715E+13	1,60115E+13	61

In the following figure (Figure 3- 4) a SEM image of NPs after the contact protocol with ^{18}F-FDG is reported, the image shows that the NPs maintain their stability after the absorption too.
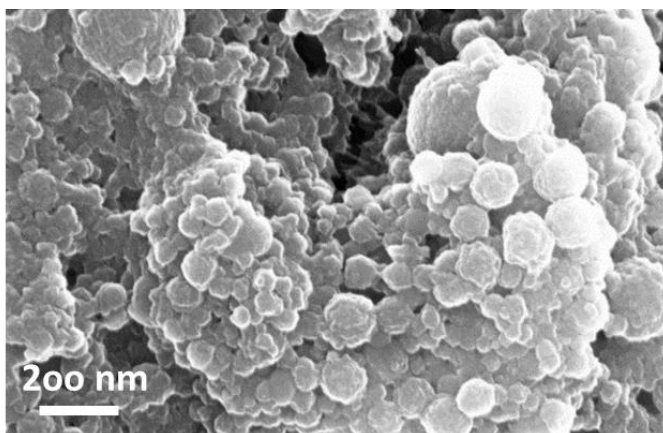
Figure 3-5: **Morphological characterization of nanoparticles by Fe-SEM:.** *NPs with Gd-DTPA after the sorption step performed with FDG decayed at 0.014 mg/ml.*

3.4.2 In vitro simultaneous PET/MRI acquisition

The simultaneous acquisition PET/MRI showed an absorption of the ^{18}F-FDG by the HyCoS NPs measuring activity in a range between 1.87 µCi (Figura 3-6 A) and 3.32 µCi (Figura 3-6 B)after about 90 min from the synthesis of ^{18}F-FDG (60 µCi/ml). The analysis of the radioactivity performed on the eluates showed an activity of about 6µCi at the same time point (Figura 3-6 C and D). The time point is been chosen in relation to the half-life of the radiotracer of about one hour. The co-registration PET/MRI (Figure 3-6) of the signals on the samples do not presents interference, enabling the measurements of a T1 equal to 300 ms (Figura 3-6– right – A) and 600 ms (Figura 3-6– right – B) and the PET in a range between 1.87 (Figura 3-6– middle – A) and 3.32 µCi (Figura 3-6 middle-B), 90 min after the synthesis of ^{18}F-FDG (60 µCi/ml). Results clearly show that the amount of radiotracers absorbed by the HyCoS NPs is sufficient to obtain a Human Administration dosage. The amount of radiotracers not absorbed has been also measure to compare the results.
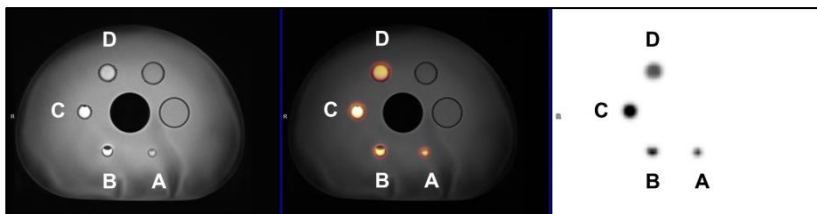
Figure 3-6: **Simultaneous PET/MRI acquisition:** *On the left the Hybrid PET/MRI scan, in the center the PET acquisition and on the right the MRI one (Inner Diameters: 10 mm (A), 13 mm (B), 17 mm(C), 22 mm (D)).*

3.5 Discussion

The proposed protocol could integrated at the downstream of the synthesis of ^{18}F-FDG. Indeed, the radiotracer can be entrapped into the NPs taking advantages by the positive charge of the chitosan core which can attract the radiotracer and control its release by sorption. Furthermore, using the method described in this chapter, it is possible to integrate directly in radiopharmacy the designed nanovectors with the radiotracers mantaining their stability and making the product available as a ready-to-use compound in the clinical practice. The sorption of the radiotracer within the nanoparticles may be due mainly to the concentration gradient obtained by freeze drying between the external and the internal phase but the entrapment of the radiotracer is probably due to the positive charge of the chitosan scorekeeping the radiopharmaceutical compound (negatively charged) trapped in the polymer mesh. Further in vivo study needed will assess the biodistribution of the

nanoparticles. Indeed, when the tracers are entrapped within nanoparticles they will follow the biodistribution of the nanoparticles. Particularly, the radiotracer will not follow the traditional metabolic pathway of the glucose but a new one dictated by the nanoparticles. The protocol used enables preparing an injectable suspension usable for simultaneous acquisitions PET / MRI without altering the chemical nature of the molecules as approved by the Food and Drug Administration. (FDA). In addition, the boosted relaxometric properties of the HyCoS NPs are also preserved providing a probe with improved efficacy. Furthermore, it is important to point out that the formulation of the HyCoS NPs in terms of amount of radiotracer and metal chelates concentration respect the administration dosage and the acquisition window currently in clinical use. It represents a significant and unique result, paving the way to a new class of probes that could add notable development to the diagnostic field and to the nanomedicine in general.

3.6 Conclusions

In conclusion, the obtained NPs already encapsulated with Gd-DTPA for MRI are be able to absorb ^{18}F-FDG if previously partially dried. Future development of this project will be the study of the biodistribution of the multimodal nanovectors to evaluate the stability of the complex and the difference between the

biodistribution of the ^{18}F-FDG and of the complex ^{18}F-FDG-Gd-DTPA HyCos NPs.

References

1.   Do, C.; Barnes, J. L.; Tan, C.; Wagner, B., Type of MRI contrast, tissue gadolinium, and fibrosis. *American Journal of Physiology-Renal Physiology* **2014,** *307* (7), F844-F855.

2.   Janib, S. M.; Moses, A. S.; MacKay, J. A., Imaging and drug delivery using theranostic nanoparticles. *Advanced Drug Delivery Reviews* **2010,** *62* (11), 1052-1063.

3.   Yankeelov, T. E.; Peterson, T. E.; Abramson, R. G.; Garcia-Izquierdo, D.; Arlinghaus, L. R.; Li, X.; Atuegwu, N. C.; Catana, C.; Manning, H. C.; Fayad, Z. A.; Gore, J. C., Simultaneous PET-MRI m oncology: a solution looking for a problem? *Magnetic Resonance Imaging* **2012,** *30* (9), 1342-1356.

4.   Drzezga, A.; Souvatzoglou, M.; Eiber, M.; Beer, A. J.; Fuerst, S.; Martinez-Moeller, A.; Nekolla, S. G.; Ziegler, S.; Ganter, C.; Rummeny, E. J.; Schwaiger, M., First Clinical Experience with Integrated Whole-Body PET/MR: Comparison to PET/CT in Patients with Oncologic Diagnoses. *Journal of Nuclear Medicine* **2012,** *53* (6), 845-855.

5.   Pimlott, S. L.; Ebmeier, K. P., SPECT imaging in dementia. *British Journal of Radiology* **2007,** *80*, S153-S159.

6.   Biasutti, M.; Dufour, N.; Ferroud, C.; Dab, W.; Temime, L., Cost-Effectiveness of Magnetic Resonance Imaging with a New Contrast Agent for the Early Diagnosis of Alzheimer's Disease. *Plos One* **2012,** *7* (4).

7.   Weissleder, R.; Pittet, M. J., Imaging in the era of molecular oncology. *Nature* **2008,** *452* (7187), 580-589.

8.   Wermke, M. D.; Sorg, C.; Wohlschlaeger, A.; Drzezga, A., A New Integrative Model of Cerebral Activation, Deactivation and Default Mode Function in Alzheimer's disease. *European Journal of Nuclear Medicine and Molecular Imaging* **2008,** *35*, S315-S316.

9.   Key, J.; Leary, J. F., Nanoparticles for multimodal in vivo imaging in nanomedicine. *International Journal of Nanomedicine* **2014,** *9*, 711-726.

10.   Small, G. W.; Bookheimer, S. Y.; Thompson, P. M.; Cole, G. M.; Huang, S. C.; Kepe, V.; Barrio, J. R., Current and future uses of neuroimaging for cognitively impaired patients. *Lancet Neurology* **2008,** *7* (2), 161-172.

11.   Lee, D. E.; Koo, H.; Sun, I. C.; Ryu, J. H.; Kim, K.; Kwon, I. C., Multifunctional nanoparticles for multimodal imaging and theragnosis. *Chemical Society Reviews* **2012,** *41* (7), 2656-2672.

12.   Jack, C. R., Alzheimer Disease: New Concepts on Its Neurobiology and the Clinical Role Imaging Will Play. *Radiology* **2012,** *263* (2), 343-360.

13.   Catana, C.; Drzezga, A.; Heiss, W.-D.; Rosen, B. R., PET/MRI for Neurologic Applications. *Journal of Nuclear Medicine* **2012,** *53* (12), 1916-1925.

14.   Brechbiel, M. W., Bifunctional chelates for metal nuclides. *Quarterly Journal of Nuclear Medicine and Molecular Imaging* **2008,** *52* (2), 166-173.

15.   Hahn, M. A.; Singh, A. K.; Sharma, P.; Brown, S. C.; Moudgil, B. M., Nanoparticles as contrast agents for in-vivo bioimaging: current status and future perspectives. *Analytical and Bioanalytical Chemistry* **2011,** *399* (1), 3-27.

16.   Melendez-Alafort, L.; Nadali, A.; Zangoni, E.; Banzato, A.; Rondina, M.; Rosato, A.; Mazzi, U., Biokinetic and dosimetric studies of Re-188-hyaluronic acid: a new radiopharmaceutical for treatment of hepatocellular carcinoma. *Nuclear Medicine and Biology* **2009,** *36* (6), 693-701.

17.   de Rosales, R. T. M., Potential clinical applications of bimodal PET-MRI or SPECT-MRI agents. *Journal of Labelled Compounds & Radiopharmaceuticals* **2014,** *57* (4), 298-303.

18.   Lee, H. Y.; Li, Z.; Chen, K.; Hsu, A. R.; Xu, C. J.; Xie, J.; Sun, S. H.; Chen, X. Y., PET/MRI dual-modality tumor imaging using arginine-glycine-aspartic (RGD) - Conjugated radiolabeled iron oxide nanoparticles. *Journal of Nuclear Medicine* **2008,** *49* (8), 1371-1379.

19.   Hwang, D. W.; Ko, H. Y.; Lee, J. H.; Kang, H.; Ryu, S. H.; Song, I. C.; Lee, D. S.; Kim, S., A Nucleolin-Targeted Multimodal

Nanoparticle Imaging Probe for Tracking Cancer Cells Using an Aptamer. *Journal of Nuclear Medicine* **2010,** *51* (1), 98-105.

20.   Zhu, H.; Zhao, J.; Lin, X. F.; Hong, Y.; Li, C.; Yang, Z., Design, Synthesis and Evaluation of Dual-Modality Glyco-Nanoparticles for Tumor Imaging. *Molecules* **2013,** *18* (6), 6425-6438.

21.   Uppal, R.; Catana, C.; Ay, I.; Benner, T.; Sorensen, A. G.; Caravan, P., Bimodal Thrombus Imaging: Simultaneous PET/MR Imaging with a Fibrin-targeted Dual PET/MR Probe-Feasibility Study in Rat Model. *Radiology* **2011,** *258* (3), 812-820.

22.   Yang, X. Q.; Hong, H.; Grailer, J. J.; Rowland, I. J.; Javadi, A.; Hurley, S. A.; Xiao, Y. L.; Yang, Y. A.; Zhang, Y.; Nickles, R.; Cai, W. B.; Steeber, D. A.; Gong, S. Q., cRGD-functionalized, DOX-conjugated, and Cu-64-labeled superparamagnetic iron oxide nanoparticles for targeted anticancer drug delivery and PET/MR imaging. *Biomaterials* **2011,** *32* (17), 4151-4160.

23.   de Rosales, R. T. M.; Tavare, R.; Glaria, A.; Varma, G.; Protti, A.; Blower, P. J., Tc-99m-Bisphosphonate-Iron Oxide Nanoparticle Conjugates for Dual-Modality Biomedical Imaging. *Bioconjugate Chemistry* **2011,** *22* (3), 455-465.

24.   Iseki, E.; Murayama, N.; Yamamoto, R.; Fujishiro, H.; Suzuki, M.; Kawano, M.; Miki, S.; Sato, K., Construction of a F-18-FDG PET normative database of Japanese healthy elderly subjects and its application to demented and mild cognitive impairment patients. *International Journal of Geriatric Psychiatry* **2010,** *25* (4), 352-361.

25.   Larson, S. M.; Schwartz, L. H., F-18-FDG PET as a candidate for "Qualified Biomarker": Functional assessment of treatment response in oncology. *Journal of Nuclear Medicine* **2006,** *47* (6), 901-903.

26.   Akamatsu, G.; Ikari, Y.; Nishio, T.; Nishida, H.; Ohnishi, A.; Aita, K.; Sasaki, M.; Sasaki, M.; Senda, M., Optimization of image reconstruction conditions with phantoms for brain FDG and amyloid PET imaging. *Annals of nuclear medicine* **2016,** *30* (1), 18-28.

4 Major findings and Future Perspectives

This work of thesis is divided in 3 main section: in the first chapter is presented an innovative complex coacervation process to produce Hybrid Core-Shell (HyCoS) NPs, which can used for Optical Imaging and MRI applications, therefore, for theranostic and multimodal applications. In particular, in this chapter is demonstrated that there is an enhancement of the MRI signal in order to possibly reduce the administration dosage clinically used for MRI acquisition. Furthermore, in the second chapter it is demonstrated that the process presented previously is able to obtain stable NPs, which can maintain their stability after the conjugation with different kinds of peptides, (A-20-36, A-20-6 and A-20-s) and the PEGylation reaction too. In addition, two different protocols of conjugation, a direct one, by conjugating the peptide to the surface, and an indirect one using as intermediate streptavidin-biotin affinity. Both protocols are tested to verify the various effectiveness and evaluate the biodistribution of the functionalized HyCoS NPs after their injection in an in vivo mice model engrafted with cellB lymphoma. The results are considered significant only for the peptide A-20-36, and in particular the direct reaction has shown a significant accumulation within the tumor mass respect to the HyCoS NPs conjugated with the indirect strategy. In fact, the HyCoS NPs opportunely functionalized for a specific tumor, a B-cell lymphoma, are detected by FMT for optical imaging application presenting an accumulation in the tumor

microenvironment after 6h from the injection and a clearance at 24h. The in vivo results are confirmed by ex vivo analysis, highlighting the presence of the functionalized HyCoS NPs with the peptide A-20-36 conjugated by the direct strategy into the tumor lesion.

In the third chapter, the ability of HyCos NPs to become a probe for Multimodal PET/MRI imaging is presented and the preparation of the nanoparticles is integrated with the production protocol of a radiotracer for nuclear magnetic applications (^{18}F-FDG). A precise protocol is introduced to obtain the absorption of the selected radiotracer by the HyCoS NPs for simultaneous PET/MRI applications. The HyCoS NPs preserve a boosting of the MRI signal and can absorb a detectable dosage of a radiotracer if opportunely pre-freeze-dried.

The in vitro results performed on a PET/MRI Scan have shown that the nanovecors improve the relaxometric properties and preserve the radioactivity without any chemical modification of the Food and Drug Administration Approved molecules. Furthermore, both the MRI and the PET signal acquired by co-registration are not influenced by the presence of the polymer nanovector and any interferences are detected allowing their simultaneous acquisition.

The future perspectives of this research work are:

- Test *in vitro* and *in vivo* the biodistribution of the multimodal radiotracer-HyCoS NPs to study if exists a difference with the distribution of the only radiotracer by simultaneous PET/MRI acquisition;

- Deepen the pH-sensitive behavior of the HyCoS NPs in vitro e in vivo

- Evaluate the reduction of the tumor by using A20-36 peptide for the different proposed protocols.

- Develop a new protocol for the functionalization of the PET/MRI nanovector before its integration with the radiotracer that does not adversely affect the absorption of the radiotracer by the nanovector.

Study Limitations:

- Evaluation of the safety profile regarding the ability of nanoparticles to improve the stability of the Gd- based compounds compared to the clinically approved CAs.

- Characterization in terms of concentration of the radiotracers entrapped in the nanoparticles directly at the downstream the hot cell for the production of the ^{18}F-FDG.

5 Appendix

5.1 Preliminary Results of Cellular Uptake of HyCoS NPs

In Figure A-1 is presented the uptake by cells of HyCoS NPs. It is important to note that most of the NPs incubated with the A549 cells are internalized after overnight incubation, as shown in Figure A-1. With an incubation time less than 12 hours, the nanoparticles do not have the necessary time to cross the membrane in any appreciable way, but it is possible to observe a strong interaction between the nanoparticles and the A549 at the level of the cell membrane.
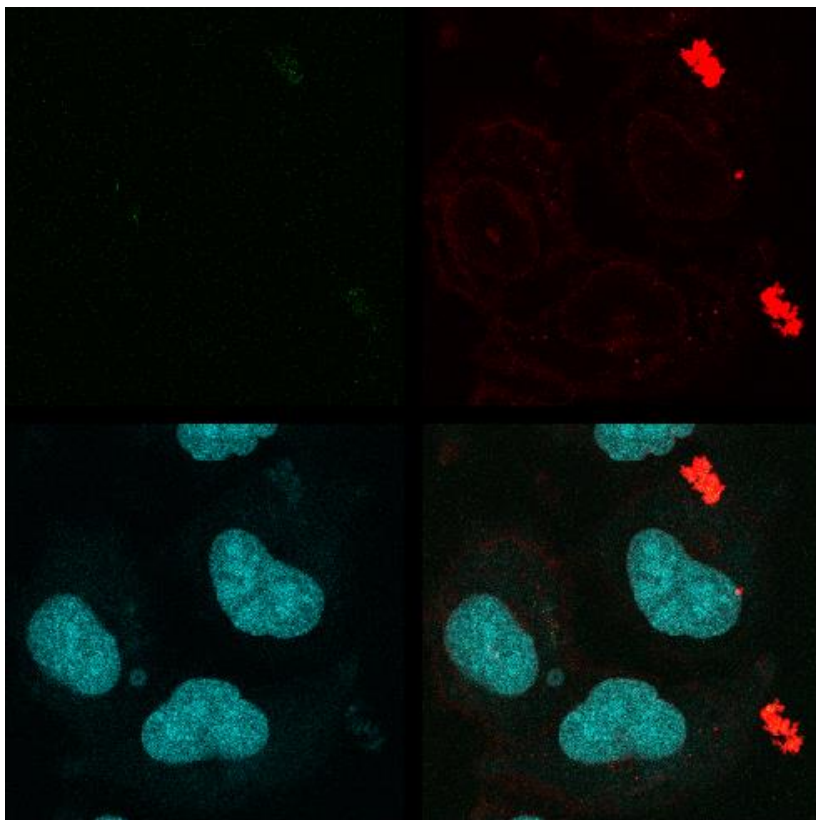
Figure A-1: *Confocal laser scanning microscopy observations of A549 cells incubated with nanoparticles loaded with atto633. For each panel, the images from left to right show fluorescence of nanoparticles in cells (green), WGA555 fluorescence in cells (red), cell nuclei stained by DRAQ5 (blue), and the merged one of the left four images. All images share the same scale bar. In the last panel is possible to observe the fluorescence of the nanoparticles in the cytoplasm following an overnight incubation.*

5.2 ICP-MS Results

In the following table ICP-MS results are reported for organs (brain,

liver, spleen, kidneys, heart and lung) of the tested animals.

Table 3: ICP-MS results reported for brain, liver, spleen, kidneys, heart and lung of the 3 tested animals after different administration of HyCoS NPs. (Chapter 1- in vivo results).

Sample	Gd 158 (cps)	gr/L	Dil ratio	TQ	Gd-DTPA (P.M.)	M	μM
T1 Heart.1	540,3	0,00054	100	0,054031	547,57	9,86736E-05	98,67357
RSD	*1,4%*						
T1 Heart.2	573,8	0,000574	100	0,057379	547,57	0,000104789	104,7888
RSD	*1,4%*		100		547,57		
T1 Heart.3	544,6	0,000545	100	0,054456	547,57	9,94503E-05	99,45029
RSD	*3,0%*		100		547,57		
T1 Lung.1	553,5	0,000554	100	0,055353	547,57	0,000101088	101,0876
RSD	*1,6%*		100		547,57		
T1 Lung.2	529,9	0,00053	100	0,05299	547,57	9,67725E-05	96,77249
RSD	*1,3%*		100		547,57		
T1 Lung.3	535,4	0,000535	100	0,053536	547,57	9,77706E-05	97,77059
RSD	*2,4%*		100		547,57		
T1 Kidneys.1	1698,9	0,001699	100	0,169894	547,57	0,000310269	310,2693
RSD	*2,3%*		100		547,57		
T1 Kidneys.2	1777,1	0,001777	100	0,177711	547,57	0,000324545	324,5446
RSD	*4,0%*		100		547,57		
T1 Kidneys.3	1603,4	0,001603	100	0,160342	547,57	0,000292824	292,8243
RSD	*1,0%*		100		547,57		
T1 Spleen.1	1650,1	0,00165	100	0,16501	547,57	0,00030135	301,3502
RSD	*4,3%*		100		547,57		
T1 Spleen.2	1761,7	0,001762	100	0,176172	547,57	0,000321734	321,7338

RSD	*8,6%*		100		547,57		
T1 Spleen.3	1808,5	0,001808	100	0,180847	547,57	0,000330271	330,2713
RSD	*3,7%*		100		547,57		
T1 Brain.1	615,0	0,000615	100	0,061504	547,57	0,000112321	112,3213
RSD	*2,1%*		100		547,57		
T1 Brain.2	650,7	0,000651	100	0,065072	547,57	0,000118839	118,8386
RSD	*1,0%*		100		547,57		
T1 Brain.3	608,2	0,000608	100	0,060821	547,57	0,000111075	111,0746
RSD	*0,6%*		100		547,57		
T1 Liver.1	2628,5	0,002628	100	0,262847	547,57	0,000480024	480,0245
RSD	*6,2%*		100		547,57		
T1 Liver.2	2570,6	0,002571	100	0,257058	547,57	0,000469453	469,4526
RSD	*2,4%*		100		547,57		
T1 Liver.3	2640,6	0,002641	100	0,264061	547,57	0,000482241	482,2409
RSD	*1,7%*		100		547,57		
T2 Heart.1	723,6	0,000724	100	0,072362	547,57	0,000132151	132,1512
RSD	*3,9%*		100		547,57		
T2 Heart.2	766,7	0,000767	100	0,076674	547,57	0,000140026	140,0257
RSD	*4,1%*		100		547,57		
T2 Heart.3	702,1	0,000702	100	0,070214	547,57	0,000128229	128,2291
RSD	*1,4%*		100		547,57		
T2 Lung.1	527,2	0,000527	100	0,052715	547,57	9,62709E-05	96,27086
RSD	*0,7%*		100		547,57		
T2 Lung.2	842,8	0,000843	100	0,084276	547,57	0,000153909	153,9093
RSD	*0,3%*		100		547,57		
T2 Lung.3	605,0	0,000605	100	0,060504	547,57	0,000110495	110,4948
RSD	*2,8%*		100		547,57		
T2 Kidneys.1	736,5	0,000737	100	0,073654	547,57	0,00013451	134,5098
RSD	*3,4%*		100		547,57		
T2 Kidneys.2	801,0	0,000801	100	0,080097	547,57	0,000146277	146,2767
RSD	*4,3%*		100		547,57		
T2 Kidneys.3	748,9	0,000749	100	0,074888	547,57	0,000136765	136,7651
RSD	*2,2%*		100		547,57		

T2 Spleen.1	1949,3	0,001949	100	0,194931	547,57	0,000355992	355,9921
RSD	*2,7%*		100		547,57		
T2 Spleen.2	1799,3	0,001799	100	0,179931	547,57	0,000328598	328,5984
RSD	*3,1%*		100		547,57		
T2 Spleen.3	1930,3	0,00193	100	0,193028	547,57	0,000352518	352,5175
RSD	*0,6%*		100		547,57		
T2 Brain.1	514,8	0,000515	100	0,051485	547,57	9,40241E-05	94,0241
RSD	*3,9%*		100		547,57		
T2 Brain.2	523,0	0,000523	100	0,052305	547,57	9,55212E-05	95,52125
RSD	*3,8%*		100		547,57		
T2 Brain.3	521,0	0,000521	100	0,052103	547,57	9,51526E-05	95,15258
RSD	*0,5%*		100		547,57		
T2 Liver.1	2019,8	0,00202	100	0,201976	547,57	0,000368858	368,8583
RSD	*5,7%*		100		547,57		
T2 Liver.2	2190,4	0,00219	100	0,219037	547,57	0,000400017	400,0167
RSD	*0,9%*		100		547,57		
T2 Liver.3	2197,7	0,002198	100	0,219775	547,57	0,000401364	401,364
RSD	*3,4%*		100		547,57		
T3 Heart.1	533,6	0,000534	100	0,053358	547,57	9,74443E-05	97,44428
RSD	*3,6%*		100		547,57		
T3 Heart.2	520,8	0,000521	100	0,05208	547,57	9,51106E-05	95,1106
RSD	*2,7%*		100		547,57		
T3 Heart.3	537,4	0,000537	100	0,053737	547,57	9,81379E-05	98,13792
RSD	*1,2%*		100		547,57		
T3 Lung.1	536,7	0,000537	100	0,053673	547,57	9,80209E-05	98,02089
RSD	*4,1%*		100		547,57		
T3 Lung.2	577,4	0,000577	100	0,057742	547,57	0,000105451	105,4508
RSD	*1,7%*		100		547,57		
T3 Lung.3	520,5	0,00052	100	0,052046	547,57	9,50498E-05	95,04979
RSD	*3,2%*		100		547,57		
T3 Kidneys.1	691,5	0,000692	100	0,069153	547,57	0,00012629	126,2899
RSD	*2,6%*		100		547,57		
T3	778,3	0,000778	100	0,077833	547,57	0,000142143	142,1432

163

Kidneys.2							
RSD	*2,4%*		100		547,57		
T3 Kidneys.3	986,0	0,000986	100	0,098597	547,57	0,000180063	180,0633
RSD	*0,3%*		100		547,57		
T3 Spleen.1	1354,5	0,001354	100	0,135446	547,57	0,000247358	247,3577
RSD	*5,5%*		100		547,57		
T3 Spleen.2	1497,6	0,001498	100	0,149756	547,57	0,000273491	273,4913
RSD	*5,3%*		100		547,57		
T3 Spleen.3	24,3	2,43E-05	100	0,002427	547,57	4,43231E-06	4,432313
RSD	*159,9%*		100		547,57		
T3 Liver.1	2096,3	0,002096	100	0,209634	547,57	0,000382845	382,8449
RSD	*1,6%*		100		547,57		
T3 Liver.2	2151,3	0,002151	100	0,215131	547,57	0,000392883	392,8827
RSD	*0,7%*		100		547,57		
T3 Liver.3	2151,3	0,002151	100	0,215131	547,57	0,000392883	392,8827
RSD	*0,7%*		100		547,57		
T3 Brain.1	474,6	0,000475	100	0,04746	547,57	8,66733E-05	86,67333
RSD	*3,4%*		100		547,57		
T3 Brain.2	523,2	0,000523	100	0,052321	547,57	9,55517E-05	95,55168
RSD	*2,2%*		100		547,57		
T3 Brain.3	532,8	0,000533	100	0,053279	547,57	9,73012E-05	97,30118
RSD	*8,1%*		100		547,57		

List of Abbreviations

NAME	ABBREVIATION
Chitosan	**Ch**
Hyaluronic Acid	**HA**
Positron Emission Tomography	**PET**
Magnetic Resonance Imaging	**MRI**
Hybrid Core Shell	**HyCoS**
Nanoparticles	**NPs**
Fluorescence molecular tomographic	**FMT**
Radiofrequency	**RF**
Computer Tomography	**CT**
Ultrasound	**US**
Divinyl Sulfone	**DVS**
Sodium Tripolyphosphate	**TPP**
Contrast Agents	**CAs**
two-photon fluorescence	**TPF**
Stimulated Emission Depletion	**STED**

Scanning Electron Microscope	**SEM**
Transmission electron microscope	**TEM**
Central Nervous System	**CNS**
Near-infrared fluorescent	**NIRF**

Collaborations

- IRCCS SDN Gianturco Street, 113 -80143-Naples.

SDN, Diagnostics and Nuclear Research Institute, is an integrated group of specialist clinics in the diagnostic laboratory and imaging.

In vivo MRI analysis are performed in the Diagnostic Center. Futhermore, the absorption procedure of radiotracer and its synthesis are conducted at the Radiopharmaceutical Department inside the Diagnostic Center IRCSS SDN in Naples where the laboratories and the equipment are adequate to manage a radiotracer in a safe way.

- Ceinge-Biotecnologie Avanzate s.c.a.r.l. Comunale Margherita, 484-538, 80131 Naples.

CEINGE - Advanced Biotechnology is a nonprofit consortium that deals with advanced biotechnology and its possible applications.

In vivo FMT measures are conducted in Ceinge Biotecnologie Avanzate s.c.a.r.l..

Communications to Congress / Conference of the student in the three years of activity:

- *Participation at the Congress CLINAM 2016 in Basel, Swiss. Comparison of Engineered Nanostructures for Multimodal in vivo Imaging. Enza Torino, Maria Russo, Donatella Vecchione, Paolo Antonio Netti. **Poster and Oral Presentation**.*
- *Participation at V Congress of the National Group of Bioengineering (GNB2016), Naples. ISBN 978-88-941906-0-1 Core-Shell Polymeric Nanoparticles obtained by a complex coacervation method for multimodal applications. Donatella Vecchione, Paolo Antonio Netti, Enza Torino. **Poster***
- *Participation at E-MRS 2016 Congress in Lilla, France "Biocompatible PET/MRI nanoparticles obtained by a coacervation method guided by temperature". Donatella Vecchione, Paolo Antonio Netti, Enza Torino. **Oral Presentation***
- *Participation at 3rd International Conference on Nanotechnology in Medicine 23-25 November 2015, Manchester, UK. Torino E., Bevilacqua P., De Sarno ., Forte E., Grimaldi A.M., Ponsiglione A.M., Romano E., Russo M., Vecchione D., Netti P.A. Design of Nanostructures to Improve Properties of Paramagnetic Contrast Agents. **Poster***
- *Participation at the Congress IV International Conference on Nanotechnology in Medicine 7-9 November 2016 Warsaw, Poland. Comparison of Engineered Nanostructures for Multimodal in vivo Imaging. Enza Torino, Maria Russo, Donatella Vecchione, Paolo Antonio Netti. **Poster***

List of publications of the doctoral candidate

- *Abstract presented to V Congress of the National Group of Bioengineering (GNB2016). Core-Shell Polymeric Nanoparticles obtained by a complex coacervation method for multimodal applications. Donatella Vecchione, Paolo Antonio Netti, Enza Torino. ISBN 978-88-941906-0-1*

- *A Process for the preparation of double crosslinked polymeric nanoparticles –* **Patent Pending**

- *Hybrid Core-Shell (HyCoS) Nanoparticles Produced by Complex Coacervation for Multimodal Applications.* **D Vecchione**, A M Grimaldi, E Forte, P Bevilacqua, PA Netti, E Torino *just accepted by Scientific Reports (February 2017).*

- *Gd-DTPA- Hybrid Core-Shell (HyCoS) NPs entrapping ^{18}F-FDG for simultaneous PET/MRI acquisitions. -* **D Vecchione***, A C Del Prete, E Nicolai, M Salvatore, P A Netti, E Torino. submitted to* **Nanomedicine: Future Medicine.**

- *Functionalized HyCoS NPs for in vivo optical imaging applications: the case study of a B-cell lymphoma.* **D Vecchione**, *submitted to* **Small**.

Other Activities

- TEAM LEADER during the StartCup Campania with the project "KYME", Regione Campania, Naples. (October 2016)

- *Award* at the StartCup Campania with the project "KYME", Regione Campania, Naples. (October 2016) – First classified in the Bio& Nano Category.

KYME is a spin-off project of the "Center for Advanced Biomaterials for Healthcare" of Istituto Italiano di

Tecnologia (IIT) of Naples in collaboration with the University of Naples "Federico II".
The project aims to produce injectable medical devices for Magnetic Resonance Imaging (MRI). Through the use of nanotechnology, KYME aims to improve clinically used Contrast Agents (CAs) and to ensure a more effective early diagnosis, thus contributing to the improvement of diagnostic Imaging.

- **Team Leader for the KYME spin-off project** at Premio Nazionale Innovazione PNI. Modena, Italy (November 2016)

- Attendance at Bioupper Startup Accelerator, Milan, Italy
    o First selection (21 June – 16 October 2016)
    o Training Week (12-17 December 2016)
    o Acceleration Program (26 January – 6 April 2017)
    o Award Ceremony (12 April 2017)

- Research activity is part of "CeSMeMo - PONa3_00173". Project aims at the development of biomedical products, in particular of novel nanosystems for diagnostics and therapy. (June 2014 – December 2016)

- Elevator pitch to event "Unione Centenario Industriali". (February 2017).

Public Links to media reporting about KYME:

http://openinnovation.startupitalia.eu/55278-20170311-bioupper-kyme-esami-meno-tossici-piu-dettagliati

http://mobile.ilsole24ore.com/solemobile/main/art/impresa-e-territori/2017-02-27/digitale-campania-rincorre-223212.shtml?uuid=AESyJSe

http://www.ilmattino.it/innovazione/biotecnologie/bioupper_team_campano_kyme_migliori_idee_business_nanotecnologia_diagnostica_medica-2279797.html

http://www.rainews.it/dl/rainews/TGR/basic/PublishingBlock-d2203e2e-1690-4898-839d-f712cdab8eb1.html

http://ildenaro.it/imprese-e-mercati/168-imprese-e-mercati/79240/kyme-il-team-campano-tra-i-10-progetti-in-finale-a-bioupper

https://biomedical.closeupengineering.it/startup-kyme-crea-contrasto-per-rmn/8881/

http://ingegneriabiomedica.org/news/diagnostica/start-cup-campania-2016-la-diagnostica-medica-trova-nuova-luce-grazie-kyme/